POLITECNICO
MILANO 1863

SCUOLA DI INGEGNERIA INDUSTRIALE
E DELL'INFORMAZIONE

Predictor-Based Adaptive Control and Allocation for multirotor UAVs

Tesi di Laurea Magistrale in
Aeronautical Engineering - Ingegneria Aeronautica

Author: **Nicolò Borsa**

Student ID: 231952
Advisor: Prof. Davide Invernizzi
Co-advisors: Giovanni Gozzini

Academic Year: 2024-25

Abstract

This thesis presents the implementation of an Augmented P-MRAC controller on a vector-thrust quadrotor UAV and the analysis of its performance under various fault and disturbance conditions.

First, the general Augmented P-MRAC framework adopted in this thesis is introduced, described, and analyzed for a generic uncertain dynamical system. Particular attention is devoted to the structural properties of the system matrices (*e.g.* overactuation), which are exploited to improve the adaptive laws.

Subsequently, the model of a vector-thrust quadrotor UAV is introduced, and two alternative Augmented P-MRAC controller architectures for the uncertain attitude and position dynamics are presented.

The first architecture is based on the use of a single augmented P-MRAC controller, in which the uncertain attitude and position dynamics are combined into a unified model. In this case, an adaptive control allocation algorithm is employed, exploiting the online estimation of the efficiency of each individual actuator, to optimize the control allocation process.

The second architecture is based on the application of the Augmented P-MRAC controller to each subsystem separately, thereby ensuring higher modularity, reduced computational demand, and a decrease in the number of adaptive parameters needed to be estimated. This reduction is achieved through the projection of the control effectiveness matrix onto the non-null subspace in the case of an overactuated subsystem.

Subsequently, an adaptive control allocation algorithm is implemented for real-time applications, combining the two projected estimates of the control effectiveness matrix to reconstruct the full control effectiveness matrix.

The implemented Augmented P-MRAC approaches are then validated and compared in a numerical simulation environment (Simulink) under different actuator degradation and disturbance scenarios.

Finally, the Augmented P-MRAC controller is implemented on a physical quadrotor platform, and real-world experimental tests are conducted to assess its practical effectiveness.

Keywords: Augmented P-MRAC Controller; Faults; Disturbances; Singular Value Decomposition (SVD); Control Allocation

Abstract in lingua italiana

Questa tesi presenta l'implementazione di un controllore augmented P-MRAC su un UAV quadrirotore a spinta vettoriale e l'analisi delle sue prestazioni in presenza di diverse condizioni di guasto e disturbo.
Inizialmente, il framework generale dell'augmented P-MRAC adottato, viene introdotto, descritto e analizzato con riferimento a un sistema dinamico generico incerto. Particolare attenzione è rivolta alle proprietà strutturali delle matrici del sistema (*e.g.* la sovra-attuazione), che vengono sfruttate per ottimizzare le leggi di adattamento.
Successivamente, viene introdotto il modello di un UAV quadrirotore e vengono presentate due architetture alternative di un augmented P-MRAC per le dinamiche incerte di assetto e posizione.
La prima architettura si basa sull'utilizzo di un unico augmented P-MRAC, nel quale le dinamiche incerte di assetto e posizione sono combinate in un modello unificato. In questo caso, viene impiegato un algoritmo di allocazione del controllo adattativo, che sfrutta la stima online dell'efficienza di ciascun attuatore al fine di ottimizzare il processo di allocazione del controllo.
La seconda architettura si basa sull'applicazione dell'augmented P-MRAC a ciascun sottosistema separatamente, garantendo una maggiore modularità, un minore carico computazionale e una riduzione del numero di parametri adattativi da stimare. Tale riduzione è ottenuta attraverso la proiezione della matrice di efficacia del controllo sul sottospazio non nullo nel caso di un sottosistema sovraattuato.
Successivamente, viene implementato un algoritmo di allocazione del controllo adattativo per applicazioni in tempo reale, che combina le due stime della proiezione della matrice di efficacia del controllo al fine di ricostruire la matrice completa di efficacia del controllo.
I due diversi approcci P-MRAC implementati, vengono quindi validati e confrontati in un ambiente di simulazione numerica (Simulink) sotto diversi scenari di riduzione dell'efficacia degli attuatori e di disturbo.
Infine, l'augmented P-MRAC viene implementato su una piattaforma quadrirotore reale e vengono condotti test sperimentali in condizioni operative reali per valutarne l'efficacia pratica.

Parole chiave: Controllore P-MRAC Aumentato; Guasti; Disturbi; Decomposizione Ai Valori Singolari (SVD); Allocazione Del Controllo

Contents

Abstract **i**

Abstract in lingua italiana **iii**

Contents **v**

Introduction **1**

1 Augmented P-MRAC approach with parameter reduction due to over-actuation **9**

1.1 Uncertain dynamical model 9

1.2 Augmented P-MRAC Approach 10

1.2.1 Predictor Model 10

1.2.2 Singular Value Decomposition of the Input Map 11

1.2.3 Update Laws with parameter reduction thanks to overactuation . . 12

1.2.4 Update Laws without reduction 15

2 Adaptive augmentation and allocation strategies for vector-thrust UAVs **17**

2.1 Vector-thrust quadrotor UAV modeling 17

2.1.1 Configuration Space 17

2.1.2 Control-Oriented Model 18

2.1.3 Trajectory tracking control problem and baseline control system . . 19

2.1.4 Augmented P-MRAC controller architectures 21

2.2 Augmented P-MRAC approach for the full uncertain vector-thrust quadrotor UAV 22

2.3 Modular Augmented P-MRAC approach based on parameters reduction . . 24

2.3.1 Augmented P-MRAC approach for the uncertain attitude subsystem 25

2.3.2 Parameter reduction for quadrotor UAVs 27

2.3.3 Augmented P-MRAC approach for the uncertain position subsystem 30

2.3.4 Combined attitude-position Augmented P-MRAC using Adaptive Control Allocation 32

3 Numerical Simulations **35**
3.1 Attitude and Position Numerical Simulations 35
3.2 Vector-Thrust Quadrotor UAV Numerical Simulations 36
3.2.1 First Simulation: Constant position Setpoint 39
3.2.2 Second Simulation: Circular trajectory 52

4 Experimental results **63**
4.1 Hoovering condition without external disturbance 64
4.1.1 First Case: Hovering with degradation of all rotors 65
4.1.2 Second Case: Degradation of the third rotor 69
4.2 Hoovering condition with external wind disturbance and degradation of the third rotor 74
4.3 Hoovering condition with external wind disturbance and degradation of all rotors 81

5 Conclusions and future developments **87**

Bibliography **89**

A Theorems **93**

List of Figures **99**

List of Tables **103**

List of Symbols **105**

Acknowledgements **109**

Introduction

Motivation

In recent years, autonomous aerial vehicles have been increasingly deployed in a wide variety of applications. Owing to the rapid development of sensing, computation, and control technologies, these systems are expected to be employed in the near future for even more complex, safety-critical, and high-precision missions, in which even minimal errors are unacceptable.

From a commercial perspective, several companies are investing heavily in autonomous delivery systems. For instance, Amazon is developing a drone delivery program [1] aimed at achieving faster delivery times compared to traditional logistics solutions, through the use of newly developed aerial platforms [2] capable of transporting packages of up to five pounds in under one hour. Autonomous drones are also employed in sports events [3] to enhance spectators' experiences through dynamic aerial filming.

Beyond commercial applications, autonomous aerial vehicles are increasingly considered for non-commercial and humanitarian missions, such as emergency response and disaster relief operations [4], as well as the delivery of human organs for transplantation [5].

Future developments are expected to include urban air mobility systems, in which automation will play a fundamental role. Although large-scale commercial deployment has not yet been achieved, several prototypes are currently at an advanced stage of development, such as the CityAirbus demonstrator by Airbus [6] and the autonomous air taxi developed by Wisk Aero [7].

These examples do not exhaust the range of possible applications of autonomous vehicles. Additional fields, including military and agricultural domains, already employ or actively investigate autonomous aerial systems.

A common characteristic of all these applications is the stringent requirement for accuracy, precision, and reliability. Autonomous vehicles must operate safely to prevent accidents that could result in financial losses, reputational damage, or even loss of human life.

One of the major limitations of conventional autonomous control systems is that they typically perform well only under nominal operating conditions or, if designed to be ro-

bust, under conditions that differ only slightly from the nominal case. Modeling errors, actuator faults, and external disturbances can severely degrade system performance and may ultimately lead to system instability or complete failure. Given the critical nature of the aforementioned applications, such outcomes are clearly unacceptable.
For these reasons, the adoption of advanced control strategies is necessary to enable autonomous systems to cope effectively with uncertainties, disturbances, and faults, thereby improving both performance and operational safety.

State of the art

Modeling errors, external disturbances, and actuator faults represent major challenges in the control of autonomous aerial vehicles and can significantly degrade system performance, particularly under non-nominal operating conditions.
During the controller design phase, modeling errors are almost unavoidable. The synthesis of an optimal controller would require perfect knowledge of the system dynamics; however, such knowledge is unrealistic in practice. System parameters are often affected by uncertainty, and additional dynamics may be neglected either because they are unknown or because their complexity renders them impractical to model accurately. These discrepancies between the real system and its nominal model can lead to degraded performance or instability when the system operates outside its nominal conditions.
Non-nominal behavior in autonomous aerial vehicles is primarily caused by external disturbances and faults. Among external disturbances, wind gusts represent the most significant source of uncertainty. Their onset, direction, magnitude, and duration are inherently unpredictable, making their compensation particularly challenging.
Actuator faults constitute another critical issue, especially those related to degradation or failure of propulsion units. In multirotor aerial vehicles, control is achieved by modulating the angular velocities of the rotors within predefined saturation limits. Partial degradation of an actuator, which may arise from motor faults, electronic failures, or mechanical damage to the propellers, reduces the maximum achievable rotor speed and consequently limits the vehicle's maneuverability. A complete actuator failure renders the corresponding control input unusable and may result in loss of controllability.
Two main approaches are commonly adopted to address these issues: passive and active fault-tolerant control strategies [8].
Passive approaches [8–10] rely on the design of controllers that are robust against a predefined set of disturbances and faults considered during the design phase. As a result, controller gains remain fixed and are not adjusted online. The main advantage of this approach lies in its simplicity and ease of implementation.

However, passive controllers are inherently conservative and cannot compensate for all possible faults or disturbances, leading to suboptimal performance.
Active approaches [8, 11, 12], by contrast, involve the reconfiguration of the control action following the occurrence of faults or disturbances, with the objective of maintaining stability and acceptable performance. In this framework, the controller actively adapts its parameters and/or structure in response to changes in system behavior.
Compared to passive strategies, active approaches can adapt online to a wider range of faults and disturbances, provided sufficient control authority is available and the underlying assumptions are satisfied. As a result, they can potentially maintain higher performance levels under non-nominal operating conditions.
Model Reference Adaptive Control (MRAC) and its predictor-based variants (P-MRAC) have been widely investigated for aerial vehicles subject to modeling uncertainties and external disturbances.
Model Reference Adaptive Control (MRAC) [13–15] operates by enforcing the closed-loop system to follow the behavior of a predefined reference model, without requiring explicit knowledge of the true system dynamics.
The basic idea is to drive the real system to track the reference model by adapting the controller parameters in real time, based on the tracking error between the plant output and the reference model output. The core idea behind P-MRAC [14, 16, 17], instead, is

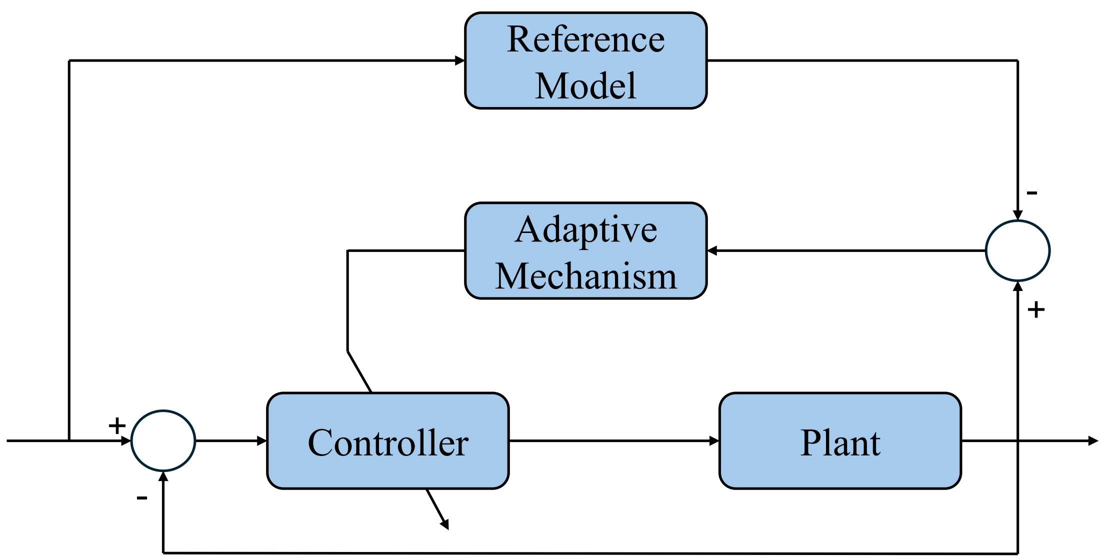

Figure 1: MRAC structure.

the introduction of an additional control layer operating in parallel with a baseline controller.

This augmented control action is activated when the system deviates from its nominal behavior due to modeling uncertainties, disturbances, or actuator faults, and aims at compensating for these effects.

The augmented adaptive framework incorporates a predictor model that runs in parallel with the baseline controller. This predictor includes a model of the controlled system and a set of estimated parameters representing the effects of unknown dynamics and external disturbances. These parameters are continuously adjusted through an update law driven by the discrepancy between the actual system response and the predictor response.

An adaptive control input, computed from the estimated parameters, is then added to the baseline control action in order to compensate for the identified uncertainties. These

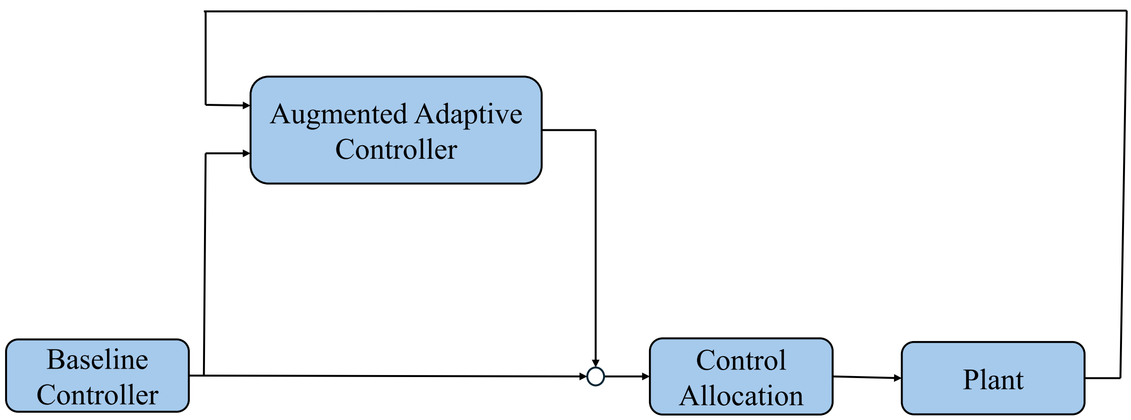

Figure 2: Augmented P-MRAC.

approaches enable online adaptation of uncertain parameters and can significantly enhance robustness under non-nominal operating conditions. However, their performance is strongly influenced by the choice of adaptation laws and by the presence of noise and unmodeled dynamics.

One of the main limitations of standard adaptive control approaches is that they do not explicitly account for actuator degradation and faults.

To address actuator degradation and faults, control allocation algorithms are commonly integrated into the adaptive control framework. Control allocation strategies [18, 19] have been extensively studied for aerial vehicles. Typical approaches include pseudo-inverse methods, quadratic programming formulations, and weighted least-squares solutions, often combined with online actuator effectiveness estimation to cope with partial loss of

effectiveness or complete failures.
The purpose of control allocation is to optimally distribute the control effort among the available actuators based on the estimated effectiveness of each actuator. This is typically achieved by introducing a control effectiveness matrix, which represents the efficiency of each actuator and is treated as an additional unknown parameter to be estimated online through a dedicated adaptation law.
Actuator saturation is also a relevant topic in the literature [20], since it limits disturbance rejection capabilities and achievable maneuverability under actuator degradation and fault conditions.
Despite significant progress in adaptive and fault-tolerant control of UAVs, several open challenges remain. In particular, existing approaches often require the online estimation of a large number of parameters, leading to increased computational burden and potentially reduced robustness. Moreover, the integration of adaptive control with control allocation is frequently addressed in a modular manner, without fully exploiting the structural properties of the actuation system.
This work builds upon these research directions by proposing an augmented adaptive control framework integrated with control allocation for a quadrotor aerial vehicle. The proposed approach aims to reduce the number of adaptive parameters and improve real-time implementability, while preserving robustness under modeling uncertainties, disturbances, and actuator faults.

Contributions

The main contributions of this thesis can be summarized as follows:

- **Augmented adaptive controller design**
  This thesis designs and implements two augmented model reference adaptive controllers: one for attitude and one for position, inspired by the approaches presented in [14, 16, 17]. Each adaptive module integrates with an existing baseline controller without modifying or redesigning the original control law.

- **Parameter reduction via SVD-based input subspace projection**
  The approach applies singular value decomposition to the control effectiveness mapping and projects it onto its non-null input subspace, as proposed in [14, 16, 18], reducing the number of adaptive parameters while preserving the full input–output information content.

- **Adaptive allocation that combines two different control effectiveness projections estimations**

Having obtained the two estimates of the projection of the control effectiveness matrix onto the non-null subspaces associated with the attitude and position subsystems, these estimates are combined to reconstruct the complete control effectiveness matrix for an adaptive allocation.

- **Structure-aware adaptation and real-time control allocation**
  The thesis exploits structural properties of the projected attitude input mapping to reduce the number of estimated parameters and simplify the adaptive update laws, and develops a real-time optimized control allocation strategy for two controller architectures compatible with the augmented adaptive controllers.

- **Experimental validation under actuator degradation and wind disturbances**
  The proposed controllers are experimentally validated on a small-scale quadrotor UAV under actuator fault conditions and realistic wind-gust disturbances.

Structure of the Thesis

The structure of the thesis is summarized as follows:

- In Chapter 1: **Augmented P-MRAC approach with parameter reduction due to overactuation** the Augmented P-MRAC controller used in this thesis is derived.
  A consideration on the structure of the control effectiveness matrix (its diagonality) is exploited to reduce the number of parameters needed to be estimated. Furthermore, some modifications (separate estimation for modeling errors and disturbances effects, projection operator applied to the parameter associated with the estimate of the effects of modeling errors and saturation limits on the estimate of Λ and its projections) are applied to improve accuracy of the estimates.

- In Chapter 2: **Adaptive augmentation and allocation strategies for vectored-thrust UAVs** the implementation of the Augmented P-MRAC controller is performed on a vector-thrust quadrotor UAV.
  Initially, the equations adopted to describe the dynamics, kinematics, and baseline control architecture of a vector-thrust quadrotor UAV are presented.
  Subsequently, the proposed Augmented P-MRAC approach is implemented using a single augmented controller, obtained by combining the uncertain attitude and position dynamics into a unified model. For this architecture, a dedicated adaptive control allocation strategy is developed and described.

Finally, the Augmented P-MRAC framework is applied separately to the uncertain attitude and position dynamics subsystems, to exploit the overactuation properties of each subsystem. An adaptive control allocation strategy specifically tailored to this separated architecture is also presented.

- In Chapter 3: **Numerical simulations** a numerical comparison between the two proposed architectures for the augmented P-MRAC controllers under different scenarios of faults and disturbances, for the full drone, is shown.
- In Chapter 4: **Experimental results** the best-performing version of the Augmented P-MRAC controller is implemented on a physical drone and real-life experimental tests are conducted under different scenarios of faults and disturbances.
- In Chapter 5 **Conclusions and future developments** the main conclusions of these thesis are summarized, and some possible future developments are presented.

1 | Augmented P-MRAC approach with parameter reduction due to overactuation

This chapter presents the formulation and theoretical analysis of the Augmented P-MRAC approach. The developments presented herein are based on and inspired by the PhD thesis [14], the conference papers [21, 22], and the journal article [16].
The approach presented herein forms the basis for the development of the adaptive control architectures for multirotor UAVs presented in Chapter 2.
The chapter is organized as follows. In the first section, a suitable uncertain dynamical model is introduced and analyzed. In the second section, the Augmented P-MRAC approach is presented and its theoretical framework is derived.

1.1. Uncertain dynamical model

To describe the Augmented P-MRAC control laws, the following representation of an uncertain dynamical system, including actuator dynamics, is considered:

$$\begin{aligned} \dot{x}_p(t) &= A_p x_p + B_p \Lambda \operatorname{sat}(u_{act}(t)) + B_p \varphi(x_p(t), t)\theta + d \\ \tau_u \dot{u}_{act} &= u_{cmd} - u_{act} \end{aligned} \tag{1.1}$$

where $x_p \in \mathbb{R}^n$ denotes the plant state, $A_p \in \mathbb{R}^{n\times n}$ is the unknown system dynamic matrix, and $B_p \in \mathbb{R}^{n\times m}$ is the input matrix. The matrix $\Lambda \in \mathbb{R}^{m\times m}$ represents the unknown control effectiveness matrix, which represents the efficiency of each control input, while $\operatorname{sat}(u_{act})$ denotes the saturated actuator input. The function $\varphi(x_p(t), t)$ is a known regressor, θ is a vector of unknown parameters, and $d \in \mathbb{R}^n$ represents external disturbances. Finally, u_{cmd} is the commanded control input, and τ_u denotes the actuator time constant.
To facilitate the application of the Augmented P-MRAC approach and control allocation techniques, an alternative two-step representation is adopted. Introducing the virtual

control vector $\nu_{act}(t) \in \mathbb{R}^r$, the system can be rewritten as:

$$\begin{aligned} \dot{x}_p(t) &= A_p x_p + B_\nu(\nu_{act}(t) + \varphi(x_p(t), t)\theta_p) \\ \nu_{act}(t) &= B_a \Lambda \, \mathrm{sat}(u_{act}(t)). \end{aligned} \tag{1.2}$$

where the effects of the disturbances have been condensed into the term $B_\nu \varphi(x_p(t), t)\theta_p$. This formulation separates the rigid-body dynamics from the actuator dynamics, enabling the application of optimized control allocation strategies.

The key to this representation is the right choice of the virtual controls $\nu_{act}(t)$. The virtual control inputs $\nu_{act}(t)$ represent a minimal set of independently controllable degrees of freedom. In mechanical systems, they typically correspond to generalized forces and moments. The matrix $B_a \in \mathbb{R}^{r \times m}$ is a known actuator mapping matrix (a known matrix that allows to map the virtual control ν, given an input u), while $B_\nu \in \mathbb{R}^{n \times r}$ is the rigid-body input matrix, such that $B_p = B_\nu B_a$.

The main advantage of this alternative representation lies in the separation between the rigid-body dynamics of the uncertain system and the actuator dynamics. Therefore, starting from a basic control allocation approach:

$$u(t) = \mathrm{pinv}(B_a \Lambda) \cdot \nu_{act}(t) \tag{1.3}$$

optimized techniques (which can exploit actuators redundancy and/or particular system structures) for control allocation can be exploited.

1.2. Augmented P-MRAC Approach

In this section, the theoretical framework of the Augmented P-MRAC approach is presented. The control input is decomposed into a baseline component, designed for the nominal plant, and an adaptive component that compensates for uncertainties and disturbances.

1.2.1. Predictor Model

A state predictor is employed to estimate both the plant state $x_p(t)$ and the unknown parameters.

The prediction error, defined as $e_p(t) = x_p(t) - \hat{x}_p(t)$, is used to derive adaptive update laws for the unknown parameters. Then, with the knowledge of these estimates, the adaptive input can be obtained.

The key aspect of this design is that parameter adaptation is performed only in the

presence of mismatches with respect to the nominal model, such as modeling uncertainties, actuator faults, or external disturbances.
The predictor dynamics is defined as:

$$\dot{\hat{x}}_p(t) = A_p\hat{x}_p + B_p\hat{\Lambda}(\text{sat}(u_{act}(t)) \pm u(t)) + B_p\varphi(x_p(t), t)\hat{\theta} + L(x_p - \hat{x}_p). \tag{1.4}$$

Following the formulation in (1.2), the predictor model can be rewritten as:

$$\begin{aligned}
\dot{\hat{x}}_p(t) &= A_p\hat{x}_p + B_\nu\hat{\nu}(t) + B_\nu(\hat{\nu}_{act}(t) - \hat{\nu}(t)) + L(x_p - \hat{x}_p) + B_\nu\varphi\hat{\theta}_p \\
\hat{\nu}(t) &= \hat{\nu}_{bl} + \hat{\nu}_{aug} = B_a\hat{\Lambda}u(t) \\
\hat{\nu}_{act}(t) &= \hat{\nu}_{bl,act} + \hat{\nu}_{aug,act} = B_a\hat{\Lambda}\,\text{sat}(u_{act}(t)) \\
\hat{\nu}_{aug} &= -\varphi\hat{\theta}_p
\end{aligned} \tag{1.5}$$

where, in this case, Λ is considered as a full $m \times m$ matrix.

1.2.2. Singular Value Decomposition of the Input Map

To facilitate the derivation of the adaptive input and update laws, a Singular Value Decomposition (SVD) of the actuator mapping matrix B_a is performed:

$$B_a = U_a\Sigma_a V_a^\top \tag{1.6}$$

where $\Sigma_a \in \mathbb{R}^{r\times m}$ is a rectangular matrix in which the diagonal entities ($\sigma_{ii} \quad i = 1, ..., r$) are the non-negative singular values of B_a; $U_a \in \mathbb{R}^{r\times r}$ and $V_a \in \mathbb{R}^{m\times m}$ are orthogonal matrices, whose columns are the left and right singular vectors, respectively.
If the system is overactuated, the range of B_a does not have full dimension because B_a has a null space due to $\text{rank}(B_a) = r < m$.
Therefore, a modification can be made to the singular value decomposition (SVD) of B_a. Due to the overactuation of the system, Σ_a is a rectangular matrix, in the following form:

$$\Sigma_a = \begin{bmatrix} D_a & 0_{r\times(m-r)} \end{bmatrix} \tag{1.7}$$

where $D_a \in \mathbb{R}^{r\times r}$ is a diagonal matrix containing the nonzero singular values.
By partitioning $U_a = [U_{ar}; U_{an}]$ and $V_a = [V_{ar}; V_{an}]$, the reduced SVD representation is obtained:

$$B_a = U_{ar}D_aV_{ar}^\top. \tag{1.8}$$

Therefore, the predictor model (1.5) can be rewritten as:

$$\begin{aligned}\dot{\hat{x}}_p(t) &= A_p\hat{x}_p + B_\nu\hat{\nu}(t) + B_\nu(\hat{\nu}_{act}(t) - \hat{\nu}(t)) + L(x_p - \hat{x}_p) + B_\nu\varphi\hat{\theta}_p \\ \hat{\nu}(t) &= U_{ar}D_aV_{ar}^\top\hat{\Lambda}u(t) = U_{ar}D_a\hat{\Lambda}_{ar}u(t).\end{aligned} \tag{1.9}$$

It can be observed that, due to the application of the Singular Value Decomposition (SVD) to the input matrix B_a and the consequent projection onto the non-null subspace of B_a, the set of parameters to be estimated changes from the full control effectiveness matrix Λ (if this matrix is assumed to be non-diagonal) to its reduced form Λ_{ar}.
This formulation enables several useful considerations.
First the projection of Λ onto the non-null subspace allows a significant reduction in the number of parameters that need to be estimated, thereby decreasing the computational burden of the adaptive algorithm.
Moreover, this projection allows actuator faults to be handled more effectively. In particular, in the presence of severe actuator degradation or total failure of one or more actuators, the matrix $\Lambda \neq I$ may become singular and thus non-invertible, which forbids the direct pseudo-inversion through (1.3).
Furthermore, instead of estimating only the projection of Λ onto V_{ar}, the projection of Λ onto both V_{ar} and V_a, $\Lambda_{aa} = V_{ar}^\top\Lambda V_a \in \mathbb{R}^{r\times m}$, is considered. This formulation facilitates, in later sections of the thesis, the application of symmetry-based arguments to further reduce the number of parameters to be estimated and guarantees the positive definiteness of the Lyapunov candidate function, later employed in the derivation of the update laws.
Conversely, the reduced matrix Λ_{aa}, remains invertible in the least-squares sense through the use of a pseudo-inverse, despite its non-square structure. This property ensures that the control allocation problem remains well-posed even under loss of actuator effectiveness.

1.2.3. Update Laws with parameter reduction thanks to overactuation

The next step is the derivation of the appropriate update laws (using the Falconì method [14]) for the parameters $\hat{\theta}_p$ and $\hat{\Lambda}_{ar}$, to ensure convergence of the prediction error $e_p(t) = x_p(t) - \hat{x}_p(t)$ to zero and stability of the parameter estimation errors $\tilde{\theta}_p(t) = \theta_p - \hat{\theta}_p(t)$ and $\tilde{\Lambda}_{aa} = \Lambda_{aa} - \hat{\Lambda}_{aa}$.
From (1.2) and (1.5), the predictor error dynamics can be computed as:

$$\dot{e}_p = A_px_p + B_\nu\nu_{act}(t) + B_\nu\varphi\theta_p - \left(A_p\hat{x}_p + B_\nu\hat{\nu}_{act}(t) + L(x_p - \hat{x}_p) + B_\nu\varphi\hat{\theta}_p\right) \tag{1.10}$$

By defining:

$$\begin{aligned}\tilde{\nu}_{act} &= \nu_{act} - \hat{\nu}_{act} = B_a(\Lambda - \hat{\Lambda})\,\mathrm{sat}(u_{act}) = U_{ar}D_aV_{ar}^\top\tilde{\Lambda}V_aV_a^\top\,\mathrm{sat}(u_{act}) \\ &= U_{ar}D_a\tilde{\Lambda}_{aa}V_a^\top\,\mathrm{sat}(u_{act}) \\ \tilde{\theta}_p &= \theta_p - \hat{\theta}_p.\end{aligned} \tag{1.11}$$

The predictor error dynamics can be rewritten as:

$$\dot{e}_p = (A_p - L)e_p + B_\nu\tilde{\nu}_{act} + B_\nu\varphi\tilde{\theta}_p \tag{1.12}$$

$$= (A_p - L)e_p + B_\nu U_{ar}D_a\tilde{\Lambda}_{aa}V_a^\top\,\mathrm{sat}(u_{act}) + B_\nu\varphi\tilde{\theta}_p. \tag{1.13}$$

The update laws for the parameters are then derived from Lyapunov stability analysis by choosing this Lyapunov candidate function:

$$V = \frac{1}{2}e_p^\top e_p + \frac{1}{2}\tilde{\theta}_p^\top\Gamma_\theta^{-1}\tilde{\theta}_p + \frac{1}{2}\,\mathrm{trace}(\tilde{\Lambda}_{aa}^\top\Gamma_\Lambda^{-1}\tilde{\Lambda}_{aa}). \tag{1.14}$$

Even if the matrix $\tilde{\Lambda}_{aa}$ is generally not a square matrix, the previous Lyapunov candidate function is still positive definite due to Lemma B.8 (Positive Definite Trace) presented in [14].

Considering the fact that the Lyapunov candidate function V is a scalar, the derivative of the Lyapunov candidate function is given by:

$$\dot{V} = \frac{1}{2}\dot{e}_p^\top e_p + \frac{1}{2}e_p^\top\dot{e}_p + \tilde{\theta}_p^\top\Gamma_\theta^{-1}\dot{\tilde{\theta}}_p + \mathrm{trace}(\tilde{\Lambda}_{aa}^\top\Gamma_\Lambda^{-1}\dot{\tilde{\Lambda}}_{aa}). \tag{1.15}$$

By substituting (1.12) in (1.15), after some computations, the derivative of the Lyapunov candidate function can be rewritten as:

$$\dot{V} = \frac{1}{2}e_p^\top(A_p - L)e_p + e_p^\top B_\nu(U_{ar}D_a\tilde{\Lambda}_{aa}V_a^\top\,\mathrm{sat}(u_{act}) + \varphi\tilde{\theta}_p) + \tilde{\theta}_p^\top\Gamma_\theta^{-1}\dot{\tilde{\theta}}_p + \mathrm{trace}(\tilde{\Lambda}_{aa}^\top\Gamma_\Lambda^{-1}\dot{\tilde{\Lambda}}_{aa}) \tag{1.16}$$

considering again the scalar dimension of V and the trace property (A.1), the previous derivative of the Lyapunov candidate function, can be rewritten as:

$$\begin{aligned}\dot{V} =& \frac{1}{2}e_p^\top(A_p - L)e_p + \mathrm{trace}\Big(\tilde{\Lambda}_{aa}^\top(D_aU_{ar}^\top B_\nu^\top e_p\,\mathrm{sat}(u_{act})^\top V_a + \Gamma_\Lambda^{-1}\dot{\tilde{\Lambda}}_{aa})\Big) + \\ &+ \tilde{\theta}_p^\top(\varphi^\top B_\nu^\top e_p + \Gamma_\theta^{-1}\dot{\tilde{\theta}}_p)\end{aligned} \tag{1.17}$$

The update laws for the parameters $\dot{\hat{\theta}}_p$ and $\dot{\hat{\Lambda}}_{aa}$, can be found such that $\dot{V}$ is negative semi-definite: this guarantees that the equilibrium point $(e_p, \tilde{\Lambda}_{aa}, \tilde{\theta}_p) = (0, 0, 0)$ is a stable equilibrium point.
To do this, due to the fact that the first term: $\frac{1}{2}e_p^\top(A_p - L)e_p$ is already negative semi-definite (By choosing an appropriate high value of L if A_p is non negative semi-definite, or by choosing any value of L if A_p is already negative semi-definite), it is only necessary to set the other terms equal to 0. The update laws, consequently, assume this form:

$$\begin{aligned} \dot{\hat{\theta}}_p &= \Gamma_\theta \varphi^\top B_\nu^\top e_p \\ \dot{\hat{\Lambda}}_{aa} &= \Gamma_\Lambda D_a U_{ar}^\top B_\nu^\top e_p \, \mathrm{sat}(u_{act})^\top V_a \rightarrow \hat{\Lambda}_{ar} = \hat{\Lambda}_{aa} V_a^\top \end{aligned} \tag{1.18}$$

where $\hat{\Lambda}_{ar}$ is computed only in case the allocation equation (1.9) is not reparametrized in terms of $\hat{\Lambda}_{aa}$.

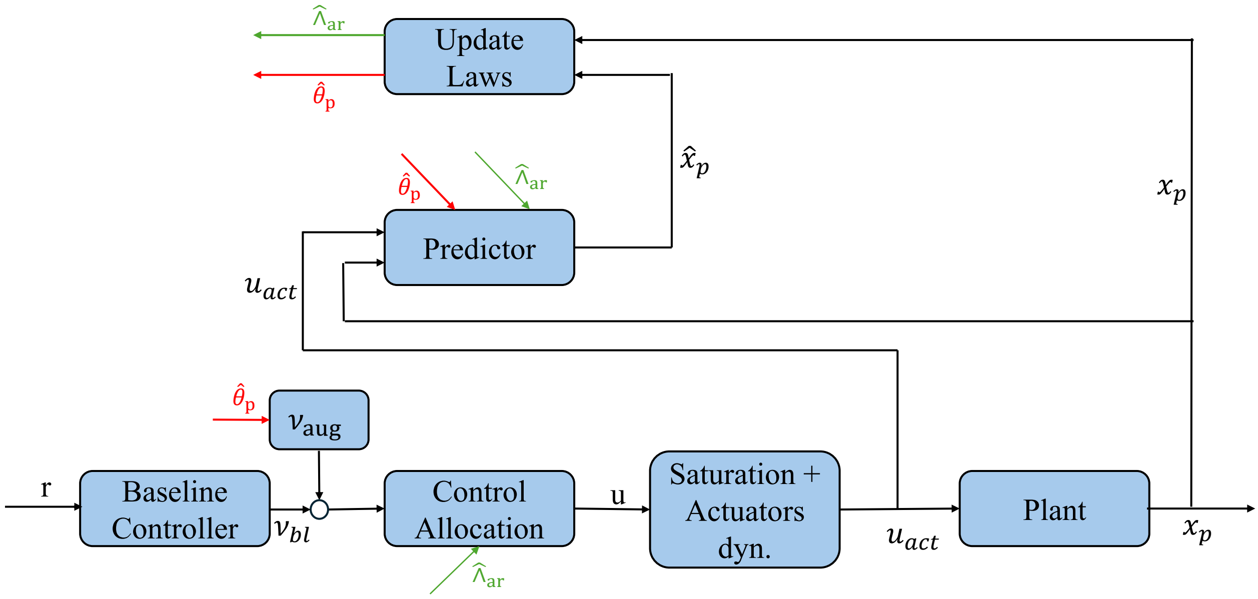

Figure 1.1: Augmented P-MRAC structure.

Figure 1.1 shows the structure of the augmented P-MRAC approach just derived for the generic uncertain dynamical model.

1.2.4. Update Laws without reduction

Alternatively, by assuming the control effectiveness matrix Λ to be diagonal rather than a full $n \times n$ matrix, its structural properties can be exploited to derive a dedicated update law directly for $\hat{\Lambda}$, rather than for the projected matrix $\hat{\Lambda}_{aa}$. In particular, it is possible to estimate only the elements on the diagonal, due to the fact that the other elements are equal to 0.
The predictor error dynamics is computed analogously to (1.10), with a difference in the definition of the virtual controls error:

$$\tilde{\nu}_{act} = \nu_{act} - \hat{\nu}_{act} = B_a(\Lambda - \hat{\Lambda})\,\mathrm{sat}(u_{act}) = B_a\,\mathrm{diag}(\mathrm{sat}(u_{act}))\tilde{\lambda} \tag{1.19}$$

where $\tilde{\lambda} = \mathrm{diag}(\tilde{\Lambda})$ is a vector that contains the diagonal elements of the Lambda estimation error parameter and $\mathrm{diag}(\mathrm{sat}(u_{act}))$ is a diagonal matrix, in which the diagonal elements are the inputs of the system (for simplicity, it will now be expressed as U_{diag}).
The predictor error dynamics can be rewritten as:

$$\dot{e}_p = (A_p - L)e_p + B_\nu B_a U_{diag}\tilde{\lambda} + B_\nu \varphi \tilde{\theta}_p. \tag{1.20}$$

The selected Lyapunov Candidate Function is:

$$V = \frac{1}{2}e_p^\top e_p + \frac{1}{2}\tilde{\theta}_p^\top \Gamma_\theta^{-1}\tilde{\theta}_p + \frac{1}{2}\tilde{\lambda}^\top \Gamma_\lambda^{-1}\tilde{\lambda}. \tag{1.21}$$

The derivative of the Lyapunov Candidate Function is given by:

$$\dot{V} = \frac{1}{2}\dot{e}_p^\top e_p + \frac{1}{2}e_p^\top \dot{e}_p + \tilde{\theta}_p^\top \Gamma_\theta^{-1}\dot{\tilde{\theta}}_p + \tilde{\lambda}^\top \Gamma_\lambda^{-1}\dot{\tilde{\lambda}}. \tag{1.22}$$

By substituting (1.20) into (1.22) and with some calculus, the derivative of the Lyapunov Candidate Function can be rewritten as:

$$\dot{V} = \frac{1}{2}e_p^\top (A_p - L)\dot{e}_p + e_p^\top B_\nu(B_a U_{diag}\tilde{\lambda} + \varphi\tilde{\theta}_p) + \tilde{\theta}_p^\top \Gamma_\theta^{-1}\dot{\tilde{\theta}}_p + \tilde{\lambda}^\top \Gamma_\lambda^{-1}\dot{\tilde{\lambda}}. \tag{1.23}$$

Considering again the scalar dimension of V, the previous derivative of the Lyapunov Candidate Function can be rewritten as:

$$\dot{V} = \frac{1}{2}e_p^\top (A_p - L)\dot{e}_p + \tilde{\lambda}^\top (U_{diag}^\top B_a^\top B_\nu^\top e_p + \Gamma_\lambda^{-1}\dot{\tilde{\lambda}}) + \tilde{\theta}_p^\top (\varphi^\top B_\nu^\top e_p + \Gamma_\theta^{-1}\dot{\tilde{\theta}}_p). \tag{1.24}$$

The update laws for the parameters $\dot{\hat{\theta}}_p$ and $\dot{\hat{\lambda}}$, assume the following form:

$$\begin{aligned} \dot{\hat{\theta}}_p &= \Gamma_\theta \varphi^\top B_\nu^\top e_p \\ \dot{\hat{\lambda}} &= \Gamma_\lambda U_{diag}^\top B_a^\top B_\nu^\top e_p \rightarrow \hat{\Lambda} = \mathrm{diag}(\hat{\lambda}). \end{aligned} \tag{1.25}$$

Remark. Due to the possible presence of noise or unmodeled disturbances during the simulations, some robust modifications need to be made to the update laws.
In particular, an upper and lower saturation limit is considered on the values of the parameter $\hat{\Lambda}_{aa}$ (or $\hat{\lambda}$), and a Projection Operator is applied to $\hat{\theta}_p$.
The Projection Operator is a smart integrator defined by a Lipschitz continuous function that keeps the adaptation parameters bounded while making the Lie Derivative of the Lyapunov function negative semi-definite in ideal conditions.
Given (θ, y) with $y = \Gamma_\theta \varphi^\top B_\nu^\top e_p$ the projection operator is defined as follows:

$$\mathrm{proj}(\theta, y) = \begin{cases} y - f(\theta)\dfrac{\nabla f(\theta)(\nabla f(\theta))^\top}{\|\nabla f(\theta)\|^2} y, & \text{if } \left[f(\theta) > 0 \wedge y^\top \nabla f(\theta) > 0\right], \\ \\ y, & \text{otherwise} \end{cases} \tag{1.26}$$

where $f(\theta) : \mathbb{R}^{n_\theta} \rightarrow \mathbb{R}$ is a convex C^1 function (to be designed) for which the sublevel (convex) sets:

$$\Omega_0 := \theta \in \mathbb{R}^{n_\theta} : f(\theta) \leq 0, \qquad \Omega_1 := \theta \in \mathbb{R}^{n_\theta} : f(\theta) \leq 1 \tag{1.27}$$

are such that $\varnothing \neq \Omega_0 \subset \Omega_1$. A common selection for the convex function $f(\theta)$ and its corresponding gradient for $|\theta| < \theta_M$, is:

$$f(\theta) = \frac{(1+\epsilon)|\theta|^2 - \theta_M^2}{\epsilon \theta_M^2} \quad \nabla f(\theta) \quad = \frac{2(1+\epsilon)}{\epsilon \theta_M^2}\theta. \tag{1.28}$$

2 | Adaptive augmentation and allocation strategies for vector-thrust UAVs

In this chapter, the Augmented P-MRAC approach is applied the class of vector-thrust quadrotor UAV, exploiting the typical cascade structure of their baseline control systems. The chapter is organized as follows. First, the controller is implemented on the isolated attitude dynamics of the vector-thrust quadrotor UAV. Subsequently, the approach is applied to the isolated position dynamics. Finally, an alternatively complete implementation on the full vector-thrust quadrotor UAV model is presented.

2.1. Vector-thrust quadrotor UAV modeling

This section presents the equations adopted to model the dynamics, kinematics, and baseline control of a vector-thrust quadrotor UAV, drawing on the works presented in [23] and the course notes [24].

2.1.1. Configuration Space

To properly describe the vector-thrust quadrotor UAV, two configuration spaces are needed:

1. NED frame $F_I := (I, \{i_I, j_I, k_I\})$ an inertial reference frame, in which i_I axis is aligned with North direction, j_I axis is aligned with East direction and k_I axis point along gravity direction.

2. Body frame $F_B := (B, \{i_B, j_B, k_B\})$ a non-inertial reference frame, whose origin coincide with the center of gravity of the UAV, in which k_B axis points in the opposite direction of the thrust direction of the propellers, the first axis i_B defines the heading direction and j_B is perpendicular to them.

The rigid transformation between the Body and the NED frame is parametrized by the Direction Cosine Matrix (DCM):

$$ {}^{\mathcal{B}}T_{\mathcal{I}} := \begin{bmatrix} \langle i_{\mathcal{I}}, i_{\mathcal{B}} \rangle & \langle j_{\mathcal{I}}, i_{\mathcal{B}} \rangle & \langle k_{\mathcal{I}}, i_{\mathcal{B}} \rangle \\ \langle i_{\mathcal{I}}, j_{\mathcal{B}} \rangle & \langle j_{\mathcal{I}}, j_{\mathcal{B}} \rangle & \langle k_{\mathcal{I}}, j_{\mathcal{B}} \rangle \\ \langle i_{\mathcal{I}}, k_{\mathcal{B}} \rangle & \langle j_{\mathcal{I}}, k_{\mathcal{B}} \rangle & \langle k_{\mathcal{I}}, k_{\mathcal{B}} \rangle \end{bmatrix} \tag{2.1} $$

2.1.2. Control-Oriented Model

Attitude dynamics and kinematics, expressed in the body frame, and position dynamics and kinematics, expressed in the inertial frame, for a generic vector-thrust quadrotor UAV, are the following:

$$ \begin{cases} J\dot{\omega}_b = -\omega_b^{\times} J\omega_b - D_{\tau\omega}\omega_b + \tau_c + d_\tau \\ \dot{R} = R\omega_b^{\times} \\ m\dot{v}_i = mge_3 - RD_{fv}R^{\top}v_i - T_cRe_3 + d_f \\ \dot{p} = v_i \end{cases} \tag{2.2} $$

where $J \in \mathbb{R}^{3\times3}$ is the inertia matrix, $\omega_b \in \mathbb{R}^3$ is angular rates vector, $D_{\tau\omega} \in \mathbb{R}^{3\times3}$ is the angular velocity damping matrix, $\tau_c \in \mathbb{R}^3$ is the control torque, $d_\tau \in \mathbb{R}^3$ is the disturbance torque, $R \in \mathbb{R}^{3\times3}$ is the rotation matrix, $m \in \mathbb{R}$ is the mass, $v_i \in \mathbb{R}^3$ is the velocity vector, g is gravity acceleration, $D_{fv} \in \mathbb{R}^{3\times3}$ is the linear velocity damping matrix, $T_c \in \mathbb{R}$ is the total thrust, $d_f \in \mathbb{R}^3$ is the disturbance velocity, and $p \in \mathbb{R}^3$ is the position vector.
The control torque $\tau_c := {}^B\tau_c := (l_c, m_c, n_c)$ and the total thrust T_c are the virtual control inputs of this model.
Defining $u = (T_1, T_2, T_3, T_4)_{cmd}$, so having as control inputs the thrusts provided by each propeller, a simple linear mapping (using the input map B_a) of the thrust generated by each propeller with the virtual control inputs, can be derived:

$$ \begin{bmatrix} 0 \\ 0 \\ T_c \\ \ell_c \\ m_c \\ n_c \end{bmatrix} = \begin{bmatrix} 0 & 0 & 0 & 0 \\ 0 & 0 & 0 & 0 \\ 1 & 1 & 1 & 1 \\ -bs(\gamma_1) & -bs(\gamma_2) & -bs(\gamma_3) & -bs(\gamma_4) \\ bc(\gamma_1) & bc(\gamma_2) & bc(\gamma_3) & bc(\gamma_4) \\ -\xi_1\sigma & -\xi_2\sigma & -\xi_3\sigma & -\xi_4\sigma \end{bmatrix} \begin{bmatrix} T_1 \\ T_2 \\ T_3 \\ T_4 \end{bmatrix} \tag{2.3} $$

where $b := |p_{BHp}|$ (position vector of the hub center of the p-th propeller from B) is the length of each arm, γ_i is angle between the i-th arm and i_B, ξ_i is the rotation direction of the i-th propeller and σ is torque aerodynamics coefficient.

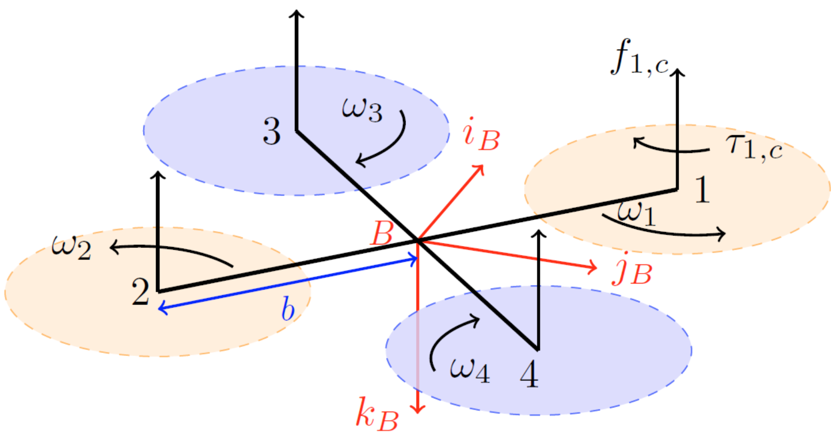

Figure 2.1: Vector-thrust UAVs scheme.

2.1.3. Trajectory tracking control problem and baseline control system

As common in autopilots for multirotor UAVs, the trajectory tracking control problem addressed in this work, is solved by a hierarchical architecture, based on the work presented in [23] and [25]

Considering the underactued nature and the structure of the system (2.2), a hierarchical control framework is proposed in which position and attitude are controlled separately. In particular the outer controller is the position one, which provides as output the total thrust and the desired attitude, while the inner one is the attitude controller.

Position Controller: Position dynamics is rewritten in term of tracking error $e_P := p - p_d$ and $e_v := v_i - v_d$, in this way:

$$\begin{aligned} \dot{e}_p &= e_v \\ m\dot{e}_v &= m(ge_3 - \dot{v}_d) + f_c + d_v. \end{aligned} \tag{2.4}$$

The virtual control force f_c is selected using this simple P/PI structure:

$$\begin{aligned} \dot{x}_{iv} &= v_i - v_c \\ f_c &= \sigma_{mf}(-K_v(v_i - v_c) - K_{iv}x_{iv} + m(\dot{v}_c - ge_3)), \end{aligned} \tag{2.5}$$

where the velocity command is selected using a proportional controller:

$$v_C = -\sigma_{mv}(K_p(p - p_d)) + v_d \tag{2.6}$$

and the generic $\sigma_{mi}(\cdot)$ is a function with this form $\sigma_{mi}(\cdot) = m_i \tanh(\frac{\cdot}{m_i})$, and $K_p, K_v, K_{iv} \in \mathbb{R}^{3\times3}$ are gain matricies.

Attitude extractor: Defining f_c as a desired control force to be designed for position tracking, a planned attitude $R_p \in SO(3)$ is computed by assigning:

$$R_p e_3 = \frac{f_c}{\|f_c\|} := b_{p3}, \tag{2.7}$$

and by including a desired heading direction $b_{d_1} \in S^2$ as a secondary control objective:

$$R_p := \begin{bmatrix} \frac{b_{p3} \times b_{d1}}{\|b_{p3} \times b_{d1}\|} \times b_{p3} & \frac{b_{p3} \times b_{d1}}{\|b_{p3} \times b_{d1}\|} & b_{p3} \end{bmatrix}. \tag{10}$$

Attitude Controller: To track the planned attitude at the velocity level, the following control law is used:

$$\omega_c := R_e^\top \omega_p - k_{\phi\theta}{}^B k_p \times {}^B k_B - \frac{k_\psi}{2}(\langle j_p, i_B\rangle - \langle i_p, j_B\rangle)^B k_B \tag{2.8}$$

where $R_e := R_p^\top R$ is the attitude error (in terms of DCMs) and $\omega_p := (R_p^\top \dot{R}_p)^\vee$ is the planned angular velocity, while k_ϕ, k_ω are scalar gains.

Given ω_c and it's time derivative $\dot{\omega}_c$, the inner loop attitude controller is given by a P/PI law:

$$\begin{aligned} \dot{x}_{i\omega} &= \omega_e \\ \tau_c &= -K_\omega \omega_e - K_{i\omega} x_{i\omega} + \omega_c^\times J\omega_b + J\dot{\omega}_c \end{aligned} \tag{2.9}$$

where $K_\omega, K_{i\omega} \in \mathbb{R}^{3\times3}$ are gain matrices, and $\omega_e := \omega_b - \omega_c$

Approach presented in [23]: to improve robustness, the control-oriented model in (2.2) is rewritten as follows:

$$\begin{cases} J\dot{\omega}_b = -\omega_b^\times J\omega_b - D_{\tau\omega}\omega_b + \lambda_\tau \tau_c + d_\tau \\ \dot{R} = R\omega_b^\times \\ m\dot{v}_i = mge_3 - RD_{fv}R^\top v_i - \lambda_{T_c} T_c R e_3 + d_f \\ \dot{p} = v_i \end{cases} \tag{2.10}$$

where $\lambda_\tau = \mathrm{diag}(\lambda_{\ell_c}, \lambda_{m_c}, \lambda_{n_c})$ and λ_{T_c} represent the efficiency of the virtual control inputs. From this formulation, an adaptive controller can be designed to estimate the virtual control efficiency terms λ_τ and λ_{T_c}, together with the remaining uncertain parameters of the model.

Subsequently, a basic control allocation is performed on the nominal model as follows:

$$\begin{bmatrix} T_1 \\ T_2 \\ T_3 \\ T_4 \end{bmatrix} = \overline{B}_a^{-1} \begin{bmatrix} T_c \\ \ell_c \\ m_c \\ n_c \end{bmatrix}, \tag{2.11}$$

where $\overline{B}_a$ denotes the nominal value of the input map.

Although this approach is straightforward and computationally efficient, it relies on significant simplifications of the uncertain model. Moreover, faults affecting individual actuators cannot be explicitly identified, since only virtual control efficiencies are estimated. As a consequence, the control allocation algorithm may generate incorrect or suboptimal actuator commands when actuator-level degradations are present.

2.1.4. Augmented P-MRAC controller architectures

Given the generic vector-thrust quadrotor UAV model introduced above, two different Augmented P-MRAC architectures are considered and analyzed:

1. In the first approach, a single augmented controller is employed. In this case, the attitude and position dynamics are combined into a unified dynamical model, and a single predictor is used to estimate the uncertain parameters and generate the adaptive control action.

2. In the second approach, the Augmented P-MRAC framework is applied separately to the attitude and position dynamics subsystems. Two distinct Augmented P-MRAC controllers are therefore employed: one for the attitude subsystem and one for the position subsystem. These two augmented controllers are then integrated within the hierarchical control framework of the full vector-thrust quadrotor UAV.

2.2. Augmented P-MRAC approach for the full uncertain vector-thrust quadrotor UAV

This section presents the first architecture of the Augmented P-MRAC approach (2.1.4) applied to the complete vector-thrust quadrotor UAV.

In particular, a single augmented controller is employed. In this case, the attitude and position dynamics are combined into a unified model, and a single predictor is used. Considering the attitude dynamics (2.17) and the position dynamics expressed in the body frame (2.40) (both sets of equations will be formally introduced in the next section), these can be combined into a single model according to (1.2) as follows:

$$
\begin{aligned}
\dot{x}_p &= A_p x_p + B_\nu \nu_{act} + B_\nu \varphi_x \theta_{Ap} + d + \begin{bmatrix} gRk_b & -J^{-1}\omega_b^\times J\omega_b \end{bmatrix}^\top \\
x_p &= \begin{bmatrix} v_x & v_y & v_z & p & q & r \end{bmatrix}^\top \\
A_p &= \begin{bmatrix} -\frac{D_{fv}}{m} & 0 \\ 0 & -J^{-1}D_{\tau\omega} \end{bmatrix} \\
B_\nu &= \begin{bmatrix} -\frac{I}{m} & 0 \\ 0 & J^{-1} \end{bmatrix} \\
\nu_{act} &= B_a \Lambda \,\mathrm{sat}(u_{act}) \\
B_a &= \begin{bmatrix} 0 & 0 & 0 & 0 \\ 0 & 0 & 0 & 0 \\ 1 & 1 & 1 & 1 \\ -bs(\gamma_1) & -bs(\gamma_2) & -bs(\gamma_3) & -bs(\gamma_4) \\ bc(\gamma_1) & bc(\gamma_2) & bc(\gamma_3) & bc(\gamma_4) \\ -\xi_1\sigma & -\xi_2\sigma & -\xi_3\sigma & -\xi_4\sigma \end{bmatrix}
\end{aligned}
\tag{2.12}
$$

where J is assumed known, $D_{\tau\omega}$ is assumed unknown, m is assumed known, D_{fv} is assumed unknown, R is assumed known, g is assumed known, and Λ is assumed unknown.

A predictor model analogous to (1.5) can then be defined as:

$$
\begin{aligned}
\dot{\hat{x}}_b &= A_p \hat{x}_b + B_\nu \hat{\nu} + B_\nu(\hat{\nu}_{act} - \hat{\nu}) + L(x_b - \hat{x}_b) + \\
&\quad B_\nu \varphi_x \hat{\theta}_{Ap} + B_\nu \varphi_d \hat{\theta}_d + \begin{bmatrix} gRk_b & -J^{-1}\omega_b^\times J\omega_b \end{bmatrix}^\top \\
\hat{\nu}(t) &= \hat{\nu}_{bl} + \hat{\nu}_{aug} = B_a \hat{\Lambda}\,\mathrm{sat}(u_{act}) \\
\hat{\nu}_{aug} &= -(\varphi_x \hat{\theta}_{Ap} + \varphi_d \hat{\theta}_d)
\end{aligned}
\tag{2.13}
$$

It can be observed that uncertainties affecting the system matrix A_p and input disturbances are treated separately by introducing two distinct regressor functions and parameter vectors. In particular, φ_x depends solely on the system state x_b, while φ_d is defined as a function of a unitary vector.
Proceeding as in Section (1.2.4), the following parameter update laws are obtained:

$$\begin{aligned} \dot{\hat{\theta}}_{Ap} &= \Gamma_{\theta_{Ap}} \varphi_x^\top B_\nu^\top e_p \\ \dot{\hat{\theta}}_d &= \Gamma_{\theta_d} \varphi_d^\top B_\nu^\top e_p \\ \dot{\hat{\lambda}} &= \Gamma_\lambda U_{diag} B_a^\top B_\nu^\top e_p \rightarrow \dot{\hat{\Lambda}} = \mathrm{diag}(\dot{\hat{\lambda}}) \end{aligned} \tag{2.14}$$

The adaptive control allocation algorithm implemented is the following.
Initially, due to the presence of only one predictor, in this version (as presented in (2.14)), an estimation over time of $\hat{\lambda}$ is obtained.
$\hat{\lambda}$, as explained before, is a vector that contains the diagonal elements of $\hat{\Lambda}$, so, differently from the previous case, the estimated control effectiveness matrix $\hat{\Lambda}$ is always a diagonal matrix.
Exploiting the properties of the diagonal matrices, the inverse of $\hat{\Lambda}$ can be easily found by:

$$\begin{aligned} \hat{\lambda} &= \begin{bmatrix} \hat{\lambda}_1 & \hat{\lambda}_2 & \hat{\lambda}_3 & \hat{\lambda}_4 \end{bmatrix}^\top \\ \hat{\Lambda}^{-1} &= \mathrm{diag}\left(\begin{bmatrix} \frac{1}{\hat{\lambda}_1} & \frac{1}{\hat{\lambda}_2} & \frac{1}{\hat{\lambda}_3} & \frac{1}{\hat{\lambda}_4} \end{bmatrix}^\top \right) \\ \hat{\lambda}_i &= 0 \rightarrow \frac{1}{\hat{\lambda}_i} \approx 0 \end{aligned} \tag{2.15}$$

Finally, the adaptive control allocation law is obtained as:

$$u(t) = \hat{\Lambda}^{-1}\,\mathrm{pinv}(B_a)\nu(t) \tag{2.16}$$

Since B_a (defined in (2.1.2)) is known and constant, $\mathrm{pinv}(B_a)$ can be computed offline, further reducing the real-time computational burden.
The main advantage of the proposed Adaptive Control Allocation strategy, compared to the WACE-based allocation described in (2.1.3), lies in the estimation of the efficiency of each individual actuator.
By explicitly estimating actuator-level efficiencies, it becomes possible to directly detect and isolate efficiency losses or faults affecting specific actuators, rather than only inferring performance degradation at the level of the aggregated virtual control inputs. This additional layer of information enables the control allocation algorithm to explicitly account

for heterogeneous actuator health conditions.
Consequently, the control effort can be properly redistributed among the available actuators, assigning a reduced demand to degraded actuators while increasing the contribution of healthy ones. This results in improved fault isolation, enhanced robustness to partial actuator failures, and more reliable reconfiguration capabilities.
Moreover, knowledge of actuator-level efficiencies prevents the generation of inappropriate or physically unrealistic commands directed to faulty actuators. This not only improves control performance under fault conditions but also enhances the overall operational safety of the system.

2.3. Modular Augmented P-MRAC approach based on parameters reduction

This section presents the second implementation of the Augmented P-MRAC approach applied to the complete vector-thrust quadrotor UAV.
In particular the Augmented P-MRAC framework is applied separately to the attitude and position dynamics subsystems. Two distinct Augmented P-MRAC controllers are therefore employed: one for the attitude subsystem and one for the position subsystem. These two augmented controllers are then integrated within the hierarchical control framework of the full vector-thrust quadrotor UAV.
The main advantage of this architecture, compared to the previous one, lies in its modularity and implementation flexibility. In practical real-world applications, it is not necessarily required to implement adaptive augmentation on both the attitude and position dynamics simultaneously. Depending on the mission profile and performance requirements, it may be sufficient to apply the augmented adaptive controller only to the attitude subsystem (*i.e.*, for fault compensation in aggressive maneuvers) or only to the position subsystem (*i.e.*, for disturbance rejection in hovering conditions).
The previous (combined) architecture does not offer this level of flexibility, since the attitude and position dynamics are merged within a single predictor model. Even if only one augmented control action is effectively required, the other augmented input must still be computed, resulting in additional computational effort and unnecessary parameter adaptation. This reduces implementation efficiency and may negatively affect robustness due to increased parameter coupling.
In contrast, the separated architecture enables a fully modular design, where each subsystem can be independently augmented, tuned, or even deactivated without affecting the other. This improves scalability and simplifies gain tuning, especially in experimental

implementations.
Furthermore, the separate formulation allows the overactuation properties of the isolated attitude and position subsystems to be exploited independently. As discussed in (1), this leads to a reduction in the number of parameters to be estimated, improving computational efficiency, identifiability, and robustness of the adaptive laws.

2.3.1. Augmented P-MRAC approach for the uncertain attitude subsystem

This subsection presents the implementation of the Augmented P-MRAC strategy on the isolated attitude dynamics of the vector-thrust quadrotor UAV.
Recalling the attitude dynamics equation from (2.2):

$$J\dot{\omega}_b = -\omega_b^{\times} J\omega_b - D_{\tau\omega}\omega_b + \tau_c + d_\tau \tag{2.17}$$

it can be rewritten according to (1.2) as:

$$\begin{aligned} \dot{\omega}_b &= -J^{-1}D_{\tau\omega}\omega_b + J^{-1}\tau_c - J^{-1}\omega_b^{\times} J\omega_b + J^{-1}d_\tau \\ \tau_c &= W_M \Lambda\, \mathrm{sat}(u_{act}) \\ A_{p,att} &= -J^{-1}D_{\tau\omega} \\ B_{\nu,att} &= J^{-1} \\ B_a &= W_M \end{aligned} \tag{2.18}$$

where J is assumed known, $D_{\tau\omega}$ is assumed unknown, Λ is assumed unknown, and $W_M \in \mathbb{R}^{3\times4}$, the submatrix of (2.3) in which only the part associated with the three control moments is considered, is considered:

$$W_M = \begin{bmatrix} -bs(\gamma_1) & -bs(\gamma_2) & -bs(\gamma_3) & -bs(\gamma_4) \\ bc(\gamma_1) & bc(\gamma_2) & bc(\gamma_3) & bc(\gamma_4) \\ -\xi_1\sigma & -\xi_2\sigma & -\xi_3\sigma & -\xi_4\sigma \end{bmatrix} \tag{2.19}$$

Remark. Since the previous system is overactuated, the range of W_M does not have full dimension because W_M has a null space due to $\mathrm{rank}(W_M) = r < m$. Therefore, a modification on the singular value decomposition (SVD) of W_M:

$$W_M = U_M \Sigma_M V_M^{\top} \tag{2.20}$$

where $\Sigma_M \in \mathbb{R}^{r\times m}$ is a positive definite diagonal matrix, $U_M \in \mathbb{R}^{r\times r}$ and $V_M^\top \in \mathbb{R}^{m\times m}$ are orthogonal matrices, it can be done:
Due to the overactuation of the system, Σ_M is a rectangular matrix, in the following form:

$$\Sigma_M = \begin{bmatrix} D_M & 0_{r\times(m-r)} \end{bmatrix} \tag{2.21}$$

where $D_M \in \mathbb{R}^{r\times r}$ is a diagonal matrix.
Considering this structure of Σ_M, a partition of $V_M = [V_{Mr}, V_{Mn}]$ and $U_M = [U_{Mr}, U_{Mn}]$ can be made, such that W_M can be alternatively written as:

$$W_M = U_{Mr} D_M V_{Mr}^\top \tag{2.22}$$

Based on these considerations and following the framework introduced in Chapter 2, the attitude predictor model (analogous to (1.5)), is defined as:

$$\begin{aligned}
\dot{\hat{\omega}}_b &= A_{p,att}\hat{\omega}_b + B_{\nu,att}U_{Mr}D_M\hat{\Lambda}_{Mr}u(t) + B_{\nu,att}U_{Mr}D_M\hat{\Lambda}_{Mr}(\mathrm{sat}(u_{act}(t)) - u(t)) \\
&\quad - J^{-1}\hat{\omega}_b^\times J\hat{\omega}_b + L(\omega_b - \hat{\omega}_b) + B_{\nu,att}\varphi_x\hat{\theta}_{Ap} + B_{\nu,att}\varphi_d\hat{\theta}_d \\
\hat{\nu}(t) &= \hat{\nu}_{bl} + \hat{\nu}_{aug} = W_M\hat{\Lambda}u(t) = U_{Mr}D_M\hat{\Lambda}_{Mr}\,\mathrm{sat}(u_{act}) \\
\hat{\nu}_{aug} &= -(\varphi_x\hat{\theta}_{Ap} + \varphi_d\hat{\theta}_d) \\
\hat{\Lambda}_{Mr} &= V_{Mr}^\top \cdot \hat{\Lambda}
\end{aligned} \tag{2.23}$$

The corresponding update laws are given by:

$$\begin{aligned}
\dot{\hat{\theta}}_{Ap} &= \Gamma_{\theta_{Ap},att}\varphi_x^\top B_{\nu,att}^\top e_\omega \\
\dot{\hat{\theta}}_d &= \Gamma_{\theta_d,att}\varphi_d^\top B_{\nu,att}^\top e_\omega \\
\dot{\hat{\Lambda}}_{MM} &= \Gamma_{\Lambda,att}D_M^\top U_{Mr}^\top B_{\nu,att}^\top e_\omega\,\mathrm{sat}(u_{act})^\top V_M \rightarrow \dot{\hat{\Lambda}}_{Mr} = \dot{\hat{\Lambda}}_{MM} \cdot V_M^\top
\end{aligned} \tag{2.24}$$

It can be observed that uncertainties affecting the system matrix A_p and input disturbances are treated separately by introducing two distinct regressor functions and parameter vectors. In particular, φ_x depends solely on the attitude state ω_b, while φ_d is defined as a function of a unitary vector.
Moreover, the nonlinear term $-J^{-1}\omega_b^\times J\omega_b$ is assumed to be perfectly known and is therefore explicitly included in the predictor model. Any residual modeling error arising from imperfect knowledge of this term is implicitly compensated by the adaptive parameter $\hat{\theta}_{Ap}$.

2.3.2. Parameter reduction for quadrotor UAVs

For a quadrotor drone, it is possible to exploit the structure of the control effectiveness matrix Λ_{MM} in order to reduce the number of parameters required for its estimation by leveraging system symmetries.
Starting from the generic expression of Λ_{MM}, it can be rewritten as:

$$\Lambda_{MM} = V_{Mr}^{\top} \Lambda V_M = V_{Mr}^{\top} \begin{bmatrix} \Lambda V_{Mr} & \Lambda V_{Mn} \end{bmatrix} \tag{2.25}$$

Focusing on the term $V_{Mr}^{\top} \Lambda V_{Mr}$, its components can be explicitly expressed as:

$$\begin{aligned}
\Lambda_{MM} &= \begin{bmatrix} \Lambda_{MM_{11}} & \Lambda_{MM_{12}} & \Lambda_{MM_{13}} & \Lambda_{MM_{14}} \\ \Lambda_{MM_{21}} & \Lambda_{MM_{22}} & \Lambda_{MM_{23}} & \Lambda_{MM_{24}} \\ \Lambda_{MM_{31}} & \Lambda_{MM_{32}} & \Lambda_{MM_{33}} & \Lambda_{MM_{34}} \end{bmatrix} \\
V_{Mr}^{\top} \Lambda V_{Mr} &= \begin{bmatrix} \Lambda_{MM_{11}} & \Lambda_{MM_{12}} & \Lambda_{MM_{13}} & \\ \Lambda_{MM_{21}} & \Lambda_{MM_{22}} & \Lambda_{MM_{23}} & \\ \Lambda_{MM_{31}} & \Lambda_{MM_{32}} & \Lambda_{MM_{33}} & \end{bmatrix} \\
\Lambda &= \begin{bmatrix} \lambda_{11} & 0 & 0 & 0 \\ 0 & \lambda_{22} & 0 & 0 \\ 0 & 0 & \lambda_{33} & 0 \\ 0 & 0 & 0 & \lambda_{33} \end{bmatrix} \\
V_{Mr} &= \begin{bmatrix} V_{Mr_{11}} & V_{Mr_{12}} & V_{Mr_{13}} \\ V_{Mr_{21}} & V_{Mr_{22}} & V_{Mr_{23}} \\ V_{Mr_{31}} & V_{Mr_{32}} & V_{Mr_{33}} \\ V_{Mr_{41}} & V_{Mr_{42}} & V_{Mr_{43}} \end{bmatrix}
\end{aligned} \tag{2.26}$$

The individual elements of Λ_{MM} can therefore be written as:

$$\begin{aligned}
\Lambda_{MM_{11}} &= \lambda_{11} \cdot V_{Mr_{11}}^2 + \lambda_{22} \cdot V_{Mr_{21}}^2 + \lambda_{33} \cdot V_{Mr_{31}}^2 + \lambda_{44} \cdot V_{Mr_{41}}^2 \\
\Lambda_{MM_{22}} &= \lambda_{11} \cdot V_{Mr_{12}}^2 + \lambda_{22} \cdot V_{Mr_{22}}^2 + \lambda_{33} \cdot V_{Mr_{32}}^2 + \lambda_{44} \cdot V_{Mr_{42}}^2 \\
\Lambda_{MM_{33}} &= \lambda_{11} \cdot V_{Mr_{13}}^2 + \lambda_{22} \cdot V_{Mr_{23}}^2 + \lambda_{33} \cdot V_{Mr_{33}}^2 + \lambda_{44} \cdot V_{Mr_{43}}^2 \\
\Lambda_{MM_{12}} &= \Lambda_{MM_{21}} = \lambda_{11} \cdot V_{Mr_{11}} \cdot V_{Mr_{12}} + \lambda_{22} \cdot V_{Mr_{21}} \cdot V_{Mr_{22}} \\
&\qquad + \lambda_{33} \cdot V_{Mr_{31}} \cdot V_{Mr_{32}} + \lambda_{44} \cdot V_{Mr_{41}} \cdot V_{Mr_{42}} \\
\Lambda_{MM_{13}} &= \Lambda_{MM_{31}} = \lambda_{11} \cdot V_{Mr_{11}} \cdot V_{Mr_{13}} + \lambda_{22} \cdot V_{Mr_{21}} \cdot V_{Mr_{23}} \\
&\qquad + \lambda_{33} \cdot V_{Mr_{31}} \cdot V_{Mr_{33}} + \lambda_{44} \cdot V_{Mr_{41}} \cdot V_{Mr_{43}} \\
\Lambda_{MM_{23}} &= \Lambda_{MM_{32}} = \lambda_{11} \cdot V_{Mr_{12}} \cdot V_{Mr_{13}} + \lambda_{22} \cdot V_{Mr_{22}} \cdot V_{Mr_{23}} \\
&\qquad + \lambda_{33} \cdot V_{Mr_{32}} \cdot V_{Mr_{33}} + \lambda_{44} \cdot V_{Mr_{42}} \cdot V_{Mr_{43}}
\end{aligned} \tag{2.27}$$

Because the matrix V_{Mr} satisfies the condition (A.5):

$$|V_{Mr}(i,1)| = |V_{Mr}(i,2)| = |V_{Mr}(i,3)| \quad \forall i = 1, ..., 4 \tag{2.28}$$

then it follows that

$$\Lambda_{MM_{11}} = \Lambda_{MM_{22}} = \Lambda_{MM_{33}}. \tag{2.29}$$

Under this assumption, the number of independent parameters required to describe $V_{Mr}^\top \Lambda V_{Mr}$ can be reduced, yielding:

$$\begin{aligned}
\Lambda_{MM_{11}} = \Lambda_{MM_{22}} = \Lambda_{MM_{33}} &= \lambda_{11} \cdot V_{Mr_{1i}}^2 + \lambda_{22} \cdot V_{Mr_{2i}}^2 + \lambda_{33} \cdot V_{Mr_{3i}}^2 + \lambda_{44} \cdot V_{Mr_{4i}}^2 \\
\Lambda_{MM_{12}} = \Lambda_{MM_{21}} &= \lambda_{11} \cdot V_{Mr_{11}} \cdot V_{Mr_{12}} + \lambda_{22} \cdot V_{Mr_{21}} \cdot V_{Mr_{22}} \\
&\qquad + \lambda_{33} \cdot V_{Mr_{31}} \cdot V_{Mr_{32}} + \lambda_{44} \cdot V_{Mr_{41}} \cdot V_{Mr_{42}} \\
\Lambda_{MM_{13}} = \Lambda_{MM_{31}} &= \lambda_{11} \cdot V_{Mr_{11}} \cdot V_{Mr_{13}} + \lambda_{22} \cdot V_{Mr_{21}} \cdot V_{Mr_{23}} \\
&\qquad + \lambda_{33} \cdot V_{Mr_{31}} \cdot V_{Mr_{33}} + \lambda_{44} \cdot V_{Mr_{41}} \cdot V_{Mr_{43}} \\
\Lambda_{MM_{23}} = \Lambda_{MM_{32}} &= \lambda_{11} \cdot V_{Mr_{12}} \cdot V_{Mr_{13}} + \lambda_{22} \cdot V_{Mr_{22}} \cdot V_{Mr_{23}} \\
&\qquad + \lambda_{33} \cdot V_{Mr_{32}} \cdot V_{Mr_{33}} + \lambda_{44} \cdot V_{Mr_{42}} \cdot V_{Mr_{43}}
\end{aligned} \tag{2.30}$$

As a result, the number of parameters to be estimated is reduced from nine to four. Introducing the compact parameter vector

$$\lambda_{MM} = \begin{bmatrix} \lambda_{MM_1} & \lambda_{MM_2} & \lambda_{MM_3} & \lambda_{MM_4} \end{bmatrix}^\top, \tag{2.31}$$

the relationship between λ_{MM} and the original diagonal elements of Λ can be written as:

$$\lambda_{MM} = B_\Lambda \lambda, \tag{2.32}$$

where B_Λ is defined as:

$$B_\Lambda = \begin{bmatrix} V_{Mr_{1i}}^2 & V_{Mr_{2i}}^2 & V_{Mr_{3i}}^2 & V_{Mr_{4i}}^2 \\ V_{Mr_{11}} \cdot V_{Mr_{12}} & V_{Mr_{21}} \cdot V_{Mr_{22}} & V_{Mr_{31}} \cdot V_{Mr_{32}} & V_{Mr_{41}} \cdot V_{Mr_{42}} \\ V_{Mr_{11}} \cdot V_{Mr_{13}} & V_{Mr_{21}} \cdot V_{Mr_{23}} & V_{Mr_{31}} \cdot V_{Mr_{33}} & V_{Mr_{41}} \cdot V_{Mr_{43}} \\ V_{Mr_{12}} \cdot V_{Mr_{13}} & V_{Mr_{22}} \cdot V_{Mr_{23}} & V_{Mr_{32}} \cdot V_{Mr_{33}} & V_{Mr_{42}} \cdot V_{Mr_{43}} \end{bmatrix} \tag{2.33}$$

Moreover, the particular structure of V_{Mn} implies additional equalities among the elements of Λ_{MM}:

$$\begin{aligned} \Lambda_{MM_{14}} &= \Lambda_{MM_{23}} = \Lambda_{MM_{32}} \\ \Lambda_{MM_{24}} &= \Lambda_{MM_{13}} = \Lambda_{MM_{31}} \\ \Lambda_{MM_{34}} &= \Lambda_{MM_{12}} = \Lambda_{MM_{21}} \end{aligned} \tag{2.34}$$

Applying these results, if the matrix B_Λ is invertible (in this case it is invertible (A.6)), the predictor error dynamics for the attitude subsystem can be expressed as:

$$\dot{e}_\omega = (A_{p,att} - L_{att})e_\omega + B_{\nu,att} W_M U_{diag} B_\Lambda^{-1} \tilde{\lambda}_{MM} + B_{\nu,att}\varphi_x \tilde{\theta}_{Ap} + B_{\nu,att}\varphi_d \tilde{\theta}_d. \tag{2.35}$$

Considering the Lyapunov candidate function:

$$V = \frac{1}{2} e_\omega^\top e_\omega + \frac{1}{2}\tilde{\theta}_{Ap}^\top \Gamma_{\theta_{Ap,att}}^{-1} \tilde{\theta}_{Ap} + \frac{1}{2}\tilde{\theta}_d^\top \Gamma_{\theta_{d,att}}^{-1} \tilde{\theta}_d + \frac{1}{2}\tilde{\lambda}_{MM}^\top \Gamma_\Lambda^{-1} \tilde{\lambda}_{MM} \tag{2.36}$$

The following update laws can be derived:

$$\begin{aligned} \dot{\hat{\theta}}_{Ap} &= \Gamma_{\theta_{Ap,att}} \varphi_x^\top B_{\nu,att}^\top e_\omega \\ \dot{\hat{\theta}}_d &= \Gamma_{\theta_{d,att}} \varphi_d^\top B_{\nu,att}^\top e_\omega \\ \dot{\hat{\lambda}}_{MM} &= \Gamma_{\Lambda,att} B_\Lambda^{-1^\top} U_{diag}^\top W_M^\top B_{\nu,att}^\top e_\omega \\ \dot{\hat{\Lambda}}_{MM} &= \begin{bmatrix} \dot{\hat{\lambda}}_{MM_1} & \dot{\hat{\lambda}}_{MM_2} & \dot{\hat{\lambda}}_{MM_3} & \dot{\hat{\lambda}}_{MM_4} \\ \dot{\hat{\lambda}}_{MM_2} & \dot{\hat{\lambda}}_{MM_1} & \dot{\hat{\lambda}}_{MM_4} & \dot{\hat{\lambda}}_{MM_3} \\ \dot{\hat{\lambda}}_{MM_3} & \dot{\hat{\lambda}}_{MM_4} & \dot{\hat{\lambda}}_{MM_1} & \dot{\hat{\lambda}}_{MM_2} \end{bmatrix} \end{aligned} \tag{2.37}$$

This formulation reduces the number of estimated parameters associated with $V_{Mr}^\top \dot{\hat{\Lambda}} V_{Mr}$ from twelve to four, without loss of information.

2.3.3. Augmented P-MRAC approach for the uncertain position subsystem

This subsection presents the implementation of the Augmented P-MRAC approach applied to the isolated position dynamics of the vector-thrust quadrotor UAV.
Recalling the position dynamics equation introduced in (2.2):

$$m\dot{v}_i = mge_3 - RD_{fv}R^\top v_i - T_c R e_3 + d_f \tag{2.38}$$

it can be rewritten according to (1.2) as:

$$\begin{aligned}
\dot{v}_i &= -\frac{RD_{fv}R^\top}{m} v_i - \frac{Re_3}{m} T_c + ge_3 + \frac{d_f}{m} \\
T_c &= W_{Tc}\Lambda\,\mathrm{sat}(u_{act}) \\
A_{p,pos} &= -\frac{RD_{fv}R^\top}{m} \\
B_{\nu,pos} &= -\frac{Re_3}{m}
\end{aligned} \tag{2.39}$$

where m is assumed known, D_{fv} is assumed unknown, Λ is assumed unknown, R is assumed known, g is assumed known, and $W_{Tc} \in \mathbb{R}^{3\times 4}$, is the known submatrix of (2.3) in which only the part associated with the total thrust is considered.
Unlike the attitude dynamics case, the matrices $A_{p,pos}$ and $B_{\nu,pos}$ are not constant, as they depend on the rotation matrix R, which is time-varying. As a consequence, the previously introduced methodology cannot be directly applied due to the time-varying nature of these matrices.
To overcome this issue, the position dynamics, originally expressed in the inertial NED frame, are rewritten in the body frame:

$$m\dot{v}_b = mgRk_B - D_{fv}v_b - T_c k_b + d_T \tag{2.40}$$

This equation can be rewritten according to (1.2) in this form:

$$
\begin{aligned}
\dot{v}_b &= -\frac{D_{fv}}{m}v_b - \frac{I}{m}T_{cv} + gRk_b + \frac{d_T}{m} \\
T_{cv} &= \begin{bmatrix} 0 \\ 0 \\ f_z \end{bmatrix} = W_{Tc}\Lambda\,\mathrm{sat}(u_{act}) \\
A_{p,pos} &= -\frac{D_{fv}}{m} \\
B_{\nu,pos} &= -\frac{I}{m} = \begin{bmatrix} -\frac{1}{m} & 0 & 0 \\ 0 & -\frac{1}{m} & 0 \\ 0 & 0 & -\frac{1}{m} \end{bmatrix}
\end{aligned}
\tag{2.41}
$$

In this formulation, both $A_{p,pos}$ and $B_{\nu,pos}$ are constant matrices.
However, an additional assumption is required. Due to the structure of the input vector T_{cv}, whose only non-zero component is the third one, modeling uncertainties affecting the entire matrix $A_{p,\mathrm{pos}}$ and disturbances acting along all three spatial directions cannot be fully compensated. In particular, only uncertainties associated with the third diagonal element of $A_{p,\mathrm{pos}}$ and disturbances acting along the z-direction can be fully compensated by the control input.
Nevertheless, instead of adopting a reduced predictor model in which only the third state component is retained and the remaining components are neglected (since they cannot be directly compensated), a complete predictor model is still employed. This choice allows the estimation of the corresponding parameters associated with the non-actuated directions, even though these estimates are not directly used for control compensation.
Following the same procedure adopted for the attitude dynamics, a position predictor model analogous to (1.5) can be derived:

$$
\begin{aligned}
\dot{\hat{v}}_b &= A_{p,pos}\hat{v}_b + B_{\nu,pos}\hat{T}_{cv} + B_{\nu,pos}(\hat{T}_{cv,act} - \hat{T}_{cv}) + L(v_b - \hat{v}_b) + \\
&\quad B_{\nu,pos}\varphi_d\hat{\theta}_d + B_{\nu,pos}\varphi_x\hat{\theta}_{Ap} + gRk_b \\
\hat{T}_{cv}(t) &= \hat{T}_{cv,bl} + \hat{T}_{cv,aug} = W_{Tc}\hat{\Lambda}\,\mathrm{sat}(u_{act}) = U_{Tr}D_T\hat{\Lambda}_{Tr}\,\mathrm{sat}(u_{act}) \\
\hat{T}_{cv,aug} &= -(\varphi_d\hat{\theta}_d + \varphi_x\hat{\theta}_{Ap}) \\
\hat{\Lambda}_{Tr} &= V_{Tr}^{\top}\cdot\hat{\Lambda}
\end{aligned}
\tag{2.42}
$$

The corresponding parameter update laws are:

$$\begin{aligned}\dot{\hat{\theta}}_d &= \Gamma_{\theta_d,pos}\varphi_d^\top B_{\nu,pos}^\top e_v \\ \dot{\hat{\theta}}_{Ap} &= \Gamma_{\theta_{Ap},pos}\varphi_x^\top B_{\nu,pos}^\top e_v \\ \dot{\hat{\Lambda}}_{TT} &= \Gamma_{\Lambda,pos} D_T U_{Tr}^\top B_{\nu,pos}^\top e_v \, \mathrm{sat}(u_{act})^\top V_T\end{aligned} \tag{2.43}$$

As (2.3.1) uncertainties affecting the system matrix A_p and input disturbances are treated separately by introducing two distinct regressor functions and parameter vectors. In particular, φ_x depends solely on the position state v_b, while φ_d is defined as a function of a unitary vector.

These two implemented Augmented P-MRAC strategies are then applied to the attitude and position baseline controllers, respectively, as presented in (2.1.3), when considering the full vector-thrust quadrotor UAV.

Given the estimates of the projections of the control effectiveness matrix Λ onto the non-null subspaces associated with the attitude and position dynamics subsystems, respectively, an adaptive control allocation algorithm can be implemented to combine the outputs of the two augmented control modules.

2.3.4. Combined attitude-position Augmented P-MRAC using Adaptive Control Allocation

This subsection presents the second architecture of the Augmented P-MRAC approach (2.1.4) applied to the complete vector-thrust quadrotor UAV, and, in particular, the adaptive control allocation strategy for real-time implementation associated with this architecture.

If, in a real-life full vector-thrust quadrotor UAV, both the attitude and position Augmented P-MRAC controllers are required, they can be implemented by applying the previously derived augmented controllers to their respective baseline controllers, exploiting the hierarchical control framework of the full vector-thrust quadrotor UAV.

The Adaptive Control Allocation strategy adopted in this case differs slightly from the one presented in (2.2).

From (1.2), the relationship between the virtual control input and the actuator commands is given by

$$\nu(t) = B_a \Lambda u(t). \tag{2.44}$$

When the Augmented P-MRAC controller is adopted, this relationship becomes:

$$\begin{aligned} \nu(t) &= \nu_{bl}(t) + \hat{\nu}_{aug}(t) = B_a \hat{\Lambda} u(t), \\ \hat{\nu}_{aug}(t) &= -\big(\varphi_x(x,t)\hat{\theta}_{Ap}(t) + \varphi_d(x,t)\hat{\theta}_d(t)\big). \end{aligned} \tag{2.45}$$

When the two augmented controllers are applied independently to the attitude and position subsystems, estimates of Λ_{MM} and Λ_{TT} are obtained from (2.24) and (2.43), respectively. The following relations hold:

$$\begin{aligned} \hat{\Lambda}_{MM} &= V_{Mr}^{\top} \hat{\Lambda} V_M, \\ \hat{\Lambda}_{TT} &= V_{Tr}^{\top} \hat{\Lambda} V_T. \end{aligned} \tag{2.46}$$

Since V_M and V_T are orthogonal matrices obtained from the SVD of known submatrices of W, the following reconstructions can be performed:

$$\begin{aligned} \hat{\Lambda}_{Mr} &= \hat{\Lambda}_{MM} \cdot V_M^{\top} = V_{Mr}^{\top} \hat{\Lambda} V_M \cdot V_M^{\top} = V_{Mr}^{\top} \hat{\Lambda} I \\ \hat{\Lambda}_{Tr} &= \hat{\Lambda}_{TT} \cdot V_T^{\top} = V_{Tr}^{\top} \hat{\Lambda} V_T \cdot V_T^{\top} = V_{Mr}^{\top} \hat{\Lambda} I \end{aligned} \tag{2.47}$$

Using (2.23) and (2.42), the corresponding actuator commands, are given by:

$$u = \operatorname{pinv}\left(\begin{bmatrix} U_{Tr} D_T \hat{\Lambda}_{Tr} \\ U_{Mr} D_M \hat{\Lambda}_{Mr} \end{bmatrix} \right) \cdot \begin{bmatrix} \hat{T}_{cv,bl} + \hat{T}_{cv,aug} \\ \hat{\nu}_{bl} + \hat{\nu}_{aug} \end{bmatrix} \tag{2.48}$$

However, this approach entails the continuous computation of the pseudo-inverse of a 6×4 matrix. Such an operation may impose a significant computational burden on real-time embedded platforms, potentially compromising real-time feasibility.

To overcome this issue, the two estimates are combined to reconstruct the full control effectiveness matrix associated with the single actuators. Knowing the ranges of the two subsystems, V_{Mr} and V_{Tr} (as discussed in (1.6)) are also known, so the full matrix $\hat{\Lambda}$ can be reconstructed as:

$$\begin{aligned} V_R^{-1} &= \begin{bmatrix} V_{Tr}^{\top} \\ V_{Mr}^{\top} \end{bmatrix}^{-1}, \\ \hat{\Lambda}_{TM} &= \begin{bmatrix} \hat{\Lambda}_{Tr} \\ \hat{\Lambda}_{Mr} \end{bmatrix}, \\ \hat{\Lambda} &= V_R^{-1} \hat{\Lambda}_{TM}. \end{aligned} \tag{2.49}$$

In the ideal case, when $\hat{\Lambda}_{MM}$ and $\hat{\Lambda}_{TT}$ coincide with their true values, the reconstructed $\hat{\Lambda}$ is diagonal, and its inverse can be computed directly.

In practice, due to estimation errors, the reconstructed control effectiveness matrix assumes the following full 4×4 form:

$$\hat{\Lambda} = \begin{bmatrix} \lambda_1 & b & c & d \\ a & \lambda_2 & c & d \\ a & b & \lambda_3 & d \\ a & b & c & \lambda_4 \end{bmatrix}. \tag{2.50}$$

The direct inversion of a full 4×4 matrix using standard numerical methods (*e.g.*, Gauss-Jordan elimination or LU factorization (A.2)) at each control step may be computationally demanding for real-time embedded platforms.
Therefore, an optimized strategy exploiting the particular structure of $\hat{\Lambda}$ is adopted.
Using the Sherman–Morrison theorem (A.3), the matrix $\hat{\Lambda}$ can be decomposed as

$$\hat{\Lambda} = D + rv^\top, \tag{2.51}$$

where

$$r = \begin{bmatrix} 1 & 1 & 1 & 1 \end{bmatrix}^\top, \qquad v = \begin{bmatrix} a & b & c & d \end{bmatrix}^\top, \tag{2.52}$$

and

$$D = \hat{\Lambda} - rv^\top. \tag{2.53}$$

By construction, D is a diagonal matrix. Hence, if $(1 + v^\top D^{-1} r) \neq 0$, the inverse of $\hat{\Lambda}$ can be efficiently computed as

$$\hat{\Lambda}^{-1} = (D + rv^\top)^{-1} = D^{-1} - \frac{D^{-1} r v^\top D^{-1}}{1 + v^\top D^{-1} r}. \tag{2.54}$$

where D^{-1} is computed like (2.15), due to its diagonal structure.
This formulation requires only matrix-vector products and the inversion of a diagonal matrix, which can be computed very efficiently in real time.
Finally, the adaptive control allocation law is obtained as

$$u(t) = \hat{\Lambda}^{-1} \operatorname{pinv}(B_a)\nu(t) = \left(D^{-1} - \frac{D^{-1} r v^\top D^{-1}}{1 + v^\top D^{-1} r} \right) \operatorname{pinv}(B_a)\nu(t). \tag{2.55}$$

where, again, $\operatorname{pinv}(B_a)$ is computed offline.
The same considerations discussed in the final part of Section (2.2) also apply in this case.

3 | Numerical Simulations

In this chapter, the numerical simulation results of the three implemented models are presented and analyzed under various fault and disturbance scenarios.
The nominal values of the plant parameters presented in section 2.1.2, are the following:

Variable	**Description**	**SI unit**
b	0.08	m
m	0.363	Kg
σ	$9.7e^{-3}$	m
T_{max}	14.1951	N
T_{min}	0	N
r_b	$\begin{bmatrix} 0 & 0 & 0 \end{bmatrix}^\top$	m
J	$\begin{bmatrix} 0.00067 & 0 & 0 \\ 0 & 0.00069 & 0 \\ 0 & 0 & 0.00111 \end{bmatrix}$	$Kg \cdot m^2$
$D_{\tau\omega}$	$\begin{bmatrix} 0.000333 & 0 & 0 \\ 0 & 0.0002183 & 0 \\ 0 & 0 & 0.000172 \end{bmatrix}$	$N \cdot s/rad$
D_{fv}	$\begin{bmatrix} 0.05 & 0 & 0 \\ 0 & 0.05 & 0 \\ 0 & 0 & 0.1 \end{bmatrix}$	$N \cdot s/m$

Table 3.1: Plant Parameters.

3.1. Attitude and Position Numerical Simulations

In this section, the main results of the numerical simulations carried out on the isolated attitude and position subsystems are presented and discussed in a comprehensive manner. The analysis focuses on evaluating the behavior of each subsystem independently, with the objective of assessing the effectiveness of the proposed control architecture under

controlled and well-defined operating conditions.
The results are not explicitly reported in graphical form. This choice is motivated by the fact that the simulation scenarios adopted for this preliminary validation phase were intentionally simplified and do not fully represent realistic mission profiles. For instance, constant angular rate setpoints were imposed for the attitude dynamics subsystem, a condition that is not representative of typical operational maneuvers. These simplified scenarios were deliberately selected to facilitate controller validation, performance assessment, and parameter tuning, rather than to provide a complete depiction of real-flight behavior.
The numerical simulations were conducted under a wide range of operating conditions, including different fault configurations and external disturbance profiles. Various maneuvering scenarios were also considered in order to evaluate the robustness and adaptability of the control strategy. In particular, actuator faults and disturbance inputs were introduced to test the capability of the controller to maintain stability and acceptable tracking performance in the presence of model uncertainties and degradation of control effectiveness.
Overall, the simulation campaign clearly highlights the advantages of the augmented control strategy when compared to the baseline configuration. The results consistently indicate that the Augmented P-MRAC approach provides a tangible improvement in terms of disturbance rejection, fault compensation, and tracking performance. More specifically, the augmented controller demonstrated the ability to effectively counteract external disturbances and actuator faults while preserving system stability and satisfactory transient behavior.
Furthermore, the adaptive mechanism ensured a reliable estimation of the uncertain parameter vectors $\hat{\theta}_{Ap}$ and $\hat{\theta}_d$, contributing to improved model matching and enhanced robustness. At the same time, the control effectiveness matrix was reconstructed with sufficient accuracy through the estimation of $\hat{\Lambda}$, confirming the capability of the adaptive scheme to compensate for variations in actuator performance. Collectively, these results validate the effectiveness of the proposed augmented P-MRAC strategy as a robust solution for fault-tolerant control of the considered subsystems.

3.2. Vector-Thrust Quadrotor UAV Numerical Simulations

In this section, numerical simulations are carried on the full vector-thrust quadrotor UAV. The Simulink model implementing control architecture proposed in (2.2) is shown in Figure 3.1.

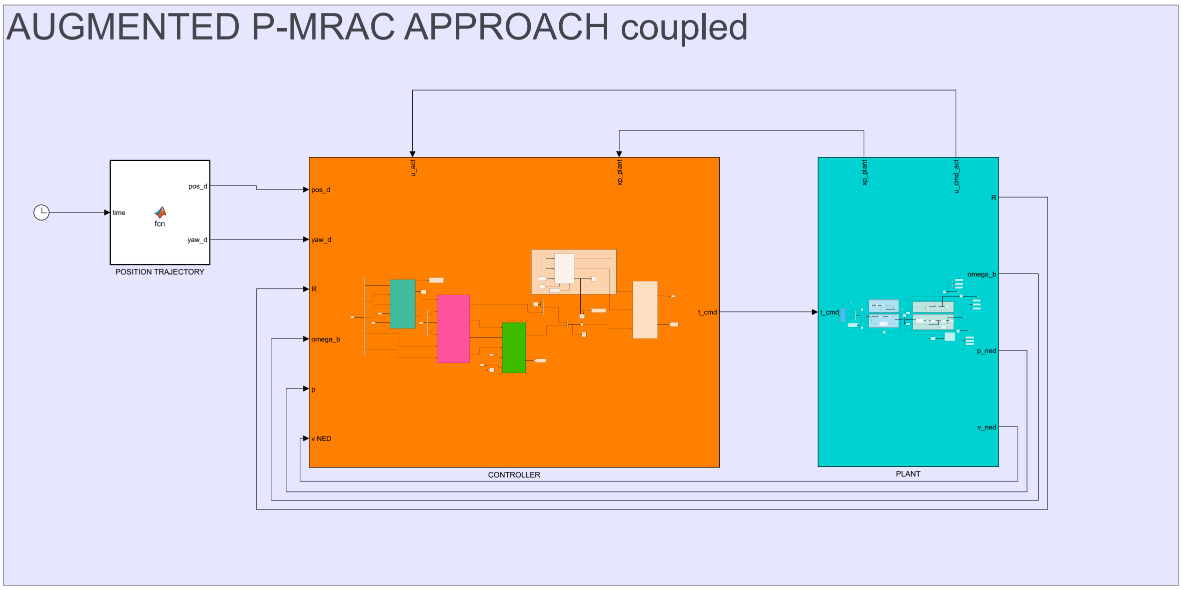

Figure 3.1: Augmented P-MRAC on the vector-thrust quadrotor UAV.

The "Position Trajectory" block generates the reference trajectory, the central orange block represents the controller, and the light blue block represents the full vector-thrust quadrotor UAV plant model.

The internal structure of the controller is shown in Figure 3.2. The leftmost block corresponds to the outer-loop position controller. The middle-left block computes the commanded attitude from the reference trajectory and thrust. The middle-right block implements the inner-loop attitude controller. The rightmost block performs control allocation. The upper block implements the Augmented P-MRAC controller for the combined dynamics.

The uncertainty parameters are the ones indicated in (2.3.1) and in (2.3.3), with a 40% deviation from nominal values. The effectiveness parameters λ_i range from 1 (no fault) to 0 (complete failure). A square-wave disturbance is applied to the total thrust.

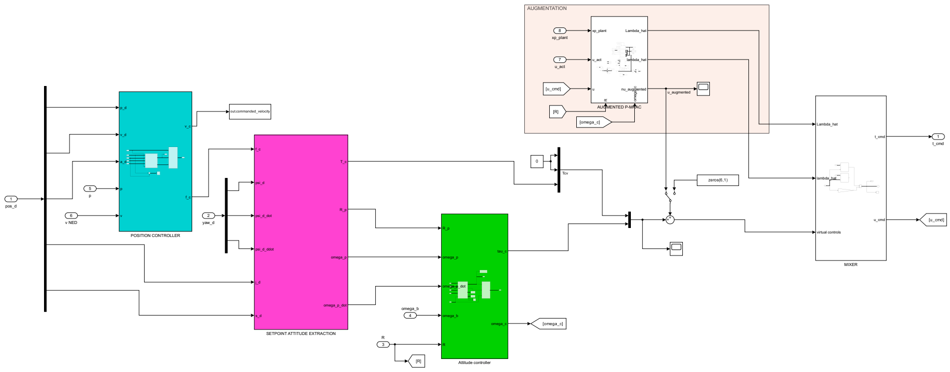

Figure 3.2: Controller block of the vector-thrust quadrotor UAV.

The control and adaptation gains for the combined approach are:

$$
\begin{aligned}
K_\omega &= 5 \cdot \mathrm{diag}([0.0039, 0.0026, 0.001]) \\
K_{i\omega} &= 2 \cdot \mathrm{diag}([0.0014, 0.0007, 0.0007]) \\
K_v &= 0.2 \cdot \mathrm{diag}([0.915, 0.915, 0.7 \cdot 2.2748]) \\
K_{iv} &= 0.1 \cdot \mathrm{diag}([0.27, 0.27, 0.2 \cdot 1.1151]) \\
K_p &= \mathrm{diag}([1, 1, 1]) \\
v_M &= 10 \\
\Gamma_\lambda &= 10 \cdot \mathrm{diag}([1, 1, 1, 1]) \\
\Gamma_{\theta_{Ap}} &= 10 \cdot \mathrm{diag}([1, 1, 1, 1, 1, 1]) \\
\Gamma_{\theta_d} &= 10 \cdot \mathrm{diag}([1, 1, 1, 1, 1, 1,]) \\
L &= 12 \cdot \mathrm{diag}([1, 1, 1, 1, 1, 1]) \\
\theta_{Ap}(0) &= \begin{bmatrix} 0 & 0 & 0 & 0 & 0 & 0 \end{bmatrix}^\top \\
\theta_d(0) &= \begin{bmatrix} 0 & 0 & 0 & 0 & 0 & 0 \end{bmatrix}^\top \\
\lambda(0) &= \begin{bmatrix} 1 & 1 & 1 & 1 \end{bmatrix}^\top \\
\theta_M &= 1e - 3 \cdot \begin{bmatrix} 30 & 30 & 55 & 0.14 & 0.09 & 0.07 \end{bmatrix}^\top \\
\epsilon &= 0.1.
\end{aligned} \tag{3.1}
$$

3.2.1. First Simulation: Constant position Setpoint

In the first simulation, a constant position setpoint $p = \begin{bmatrix} 2.5 & 2.5 & -2 \end{bmatrix}^\top m$ is commanded. The fault in the control effectiveness matrix is modelled without complete actuator failures but with the following reduction of the efficiency:

$$\Lambda = \begin{bmatrix} 0.8873 & 0 & 0 & 0 \\ 0 & 0.7855 & 0 & 0 \\ 0 & 0 & 0.7194 & 0 \\ 0 & 0 & 0 & 0.9432 \end{bmatrix}. \tag{3.2}$$

The simulation duration is set to $65s$, and an external random thrust disturbance is applied similar to the one in Figure 3.3.

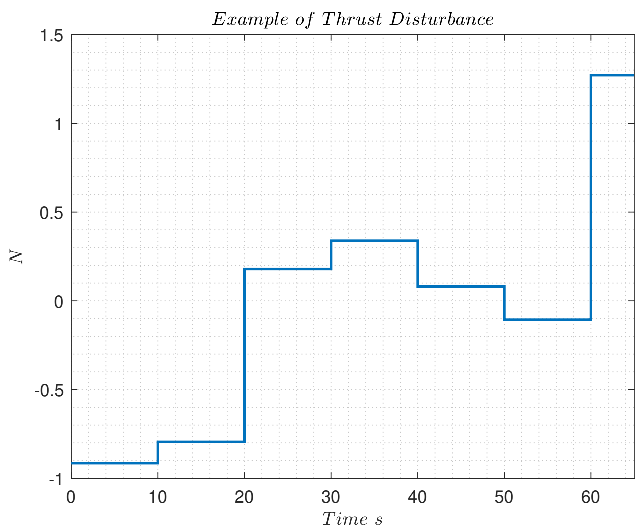

Figure 3.3: Exemple of external distrubance.

Only the responses obtained with the two augmented controllers are reported, while those of the baseline controller are omitted. This decision is justified by the fact that, in the baseline configuration, the controller fails to adequately track the commanded angular rates and velocities. Specifically, it produces control signals with excessively large amplitudes and unrealistically high-frequency oscillations. Such behavior is physically implausible and prevents any meaningful or fair comparison with the augmented control strategies.

The results are presented for the two considered architectures. The first architecture employs two decoupled predictors, one for the position dynamics and one for the attitude dynamics, as described in Section 2.3. The second architecture adopts a single predictor, and therefore a single augmentation scheme, as presented in Section 2.2.

Decoupled Architecture

Here the results produced by the two augmented controllers architecture (Section 2.2) are presented.

By analyzing the rate responses in Figure 3.4, it is clearly visible that the Decoupled controllers architecture operates correctly. In fact, after the fast initial transient, the plant rates stabilize around the commanded rates, confirming the fast response and the effectiveness of the predictor-based structure. Only the first seconds of the simulation are shown, since this is the time interval in which the drone moves toward the desired position setpoint and the rates are nonzero. Even though the disturbance effects are not clearly visible in the plots (due to their relatively small magnitude), they are sufficiently rapidly attenuated, and the resulting peaks remain limited.

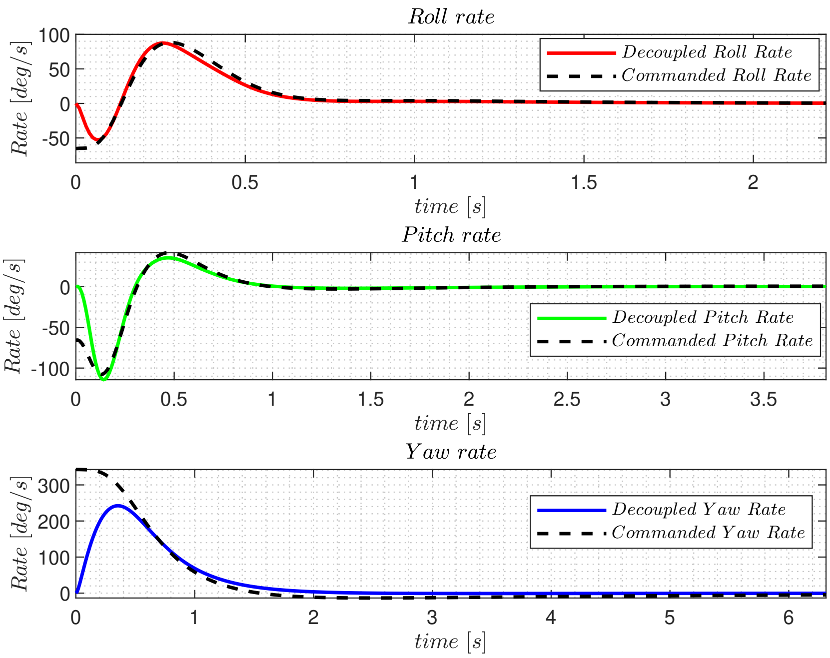

Figure 3.4: Angular rates for the position setpoint simulation in the decoupled case.

By examining the velocity and position responses in Figure 3.5 and in Figure 3.6, respectively, it can be observed that the UAV successfully reaches the desired position setpoint and remains largely unaffected by external disturbances. In particular, the disturbances have only a limited impact on the vertical dynamics, as evidenced by the small peaks observed in the z position and velocity.

It should be noted that the improvement provided by the adaptive augmentation is significant, as the baseline controller, when operating under the same conditions, is unable

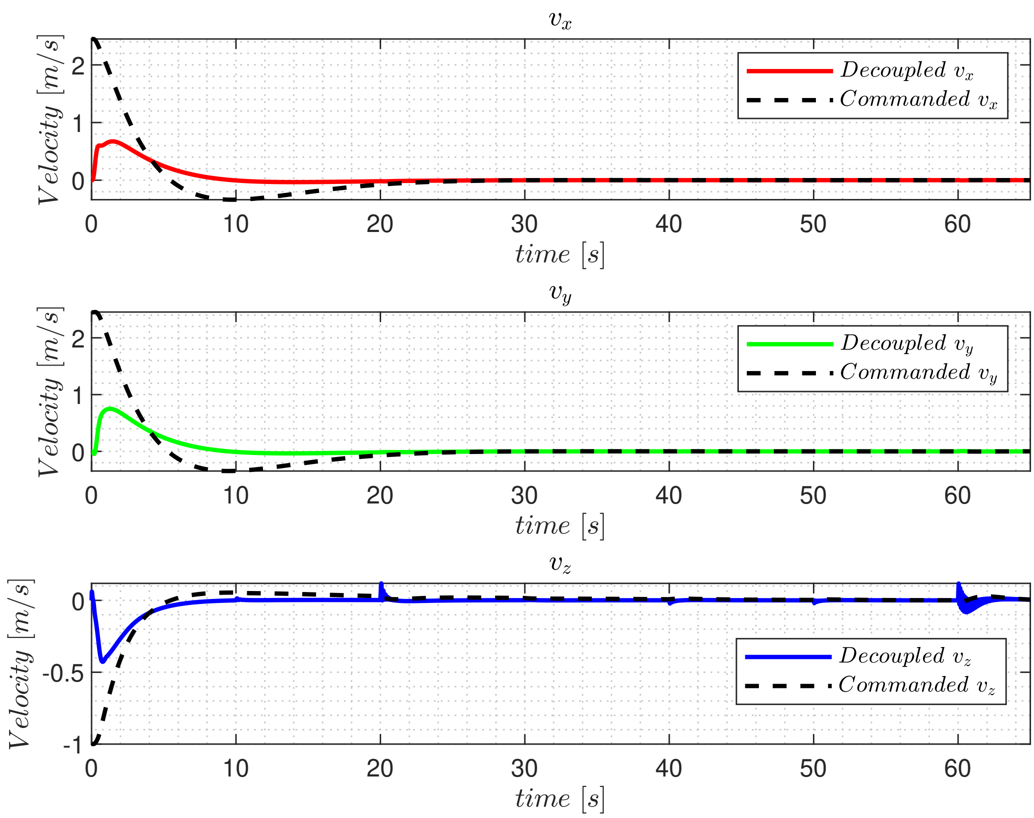

Figure 3.5: Velocity for the position setpoint simulation in the decoupled case.

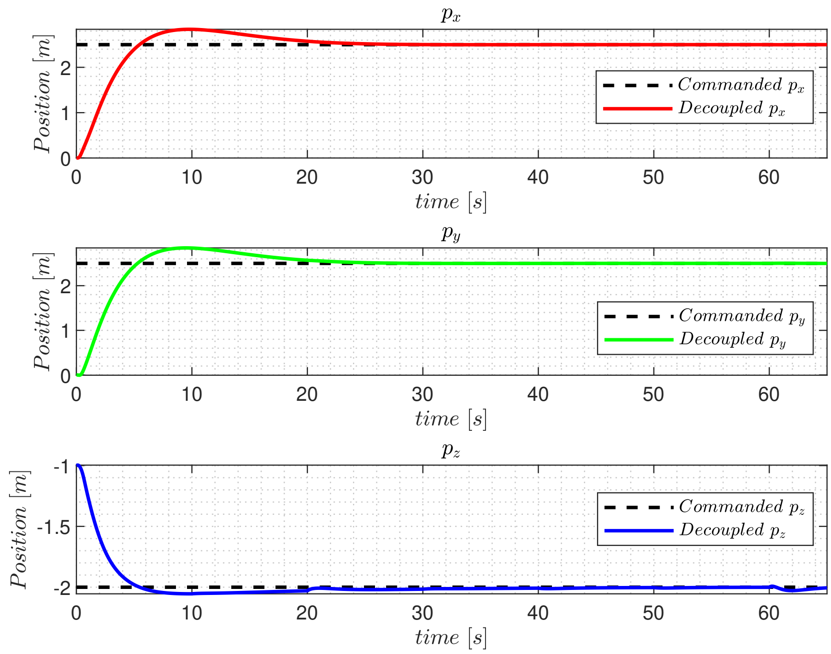

Figure 3.6: Position for the position setpoint simulation in the decoupled case.

to stabilize the system due to the reduced control effectiveness and the presence of disturbances along the vertical axis.
The state estimation errors (difference between the real state and the estimates given by the predictor) reported in Figure 3.7 further confirm the effectiveness of the augmented controllers. In fact it exhibits a very fast error dynamics, so that the estimated rates $\hat{\omega}_b$ and the estimated velocity $\hat{v}_b$ rapidly converge to the corresponding real values. This shows that the predictor model is capable of accurately reconstructing the system states even in the presence of modeling uncertainties and external disturbances.

It is also interesting to analyze in Figure 3.8 the thrust generated by each propeller during the simulation.

It can be observed that, in particular, the third propeller generally provides a higher thrust compared to the other three. This behavior is coherent with the larger efficiency reduction affecting this actuator and is therefore correct and desirable, since it reflects the ability of the control allocation algorithm to redistribute the control effort in order to compensate for actuator degradations.

Finally, the temporal evolutions of the estimated parameters, are analyzed. First, the time evolution of $\hat{\theta}_{Ap,att}(t)$ and $\hat{\theta}_{Ap,pos}(t)$ is not reported. This choice is motivated by the fact that these parameters are primarily intended to compensate for modeling uncer-

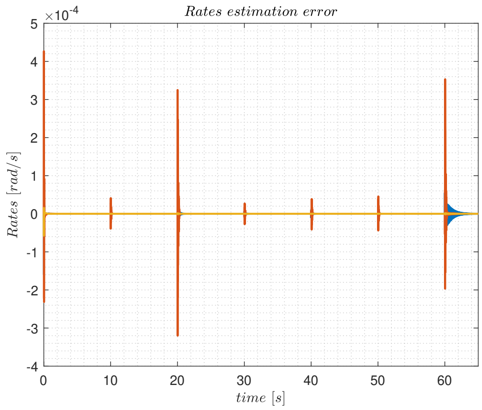

(a) Rates state estimation.

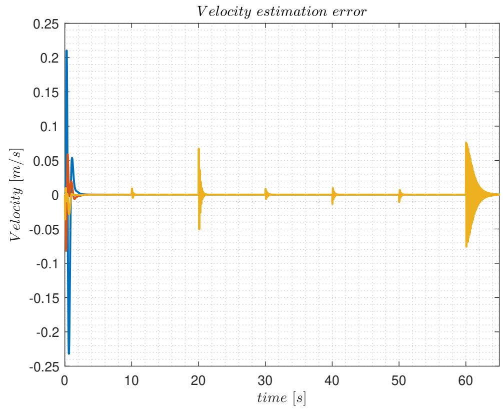

(b) Velocity state estimation error zoom.

Figure 3.7: States estimation errors for the position setpoint simulation in the decoupled case.

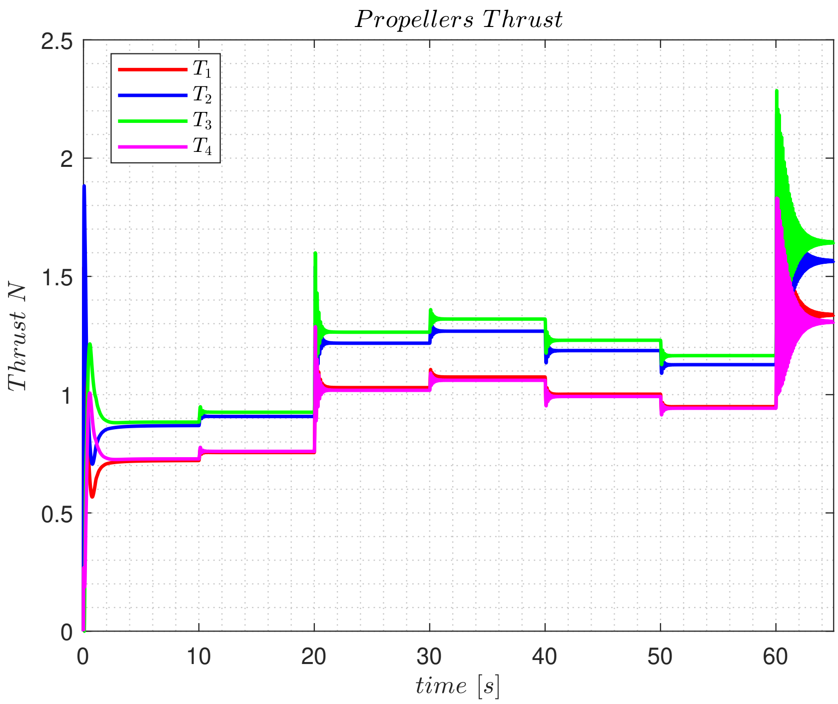

Figure 3.8: Propellers' thrust for the position setpoint simulation in the decoupled case.

tainties. In the present simulation scenario, where significant external disturbances are introduced, it was considered more meaningful to highlight the parameters directly associated with disturbance compensation. Nevertheless, $\hat{\theta}_{Ap,att}(t)$ exhibits a time evolution that is clearly influenced by the disturbance. This behavior can be explained by the coupling between the parameters associated with modeling uncertainties and those dedicated to disturbance compensation. Since all propellers are affected by efficiency reductions and the disturbance is modeled as an equivalent total thrust disturbance, the thrust generated by each propeller must be continuously adjusted to counteract its effects. This induces continuous variations in the angular rates, which in turn lead to ongoing adaptation of both parameter sets.

On the other hand, the time evolution of $\hat{\theta}_{Ap,pos}(t)$ appears to be only weakly affected by the disturbance. Unlike the attitude case, variations in the thrust distribution among the propellers do not directly and significantly influence the horizontal velocity components. As a result, the position-related modeling uncertainty parameters exhibit a more stable behavior.

Instead, the time evolution of the diturbances $\hat{\theta}_{d,att}(t)$, $\hat{\theta}_{d,pos}(t)$, and of the effectiveness $\hat{\Lambda}(t)$ are reported in Figure 3.9, Figure 3.10 and Figure 3.11.

When analyzing the time evolution of $\hat{\theta}_{d,att}(t)$ and $\hat{\theta}_{d,pos}(t)$, it can be observed that both are strongly influenced by the disturbance and exhibit a waveform resembling a square wave similar to the one of the external disturbance. In particular, the first two elements of $\hat{\theta}_{d,att}(t)$, associated with the roll and pitch rates, show this behavior for the same reasons discussed previously, namely the continuous redistribution of thrust required to counteract the disturbance. Similarly, the last element of $\hat{\theta}_{d,pos}(t)$, associated with the z-velocity, is significantly affected due to the nature of the external disturbance, which acts along the vertical direction.
This behavior is fully consistent with the role of these parameters, whose primary objective is to compensate for external disturbances. Consequently, their adaptation closely follows the disturbance profile.

When analyzing the time evolution of $\hat{\Lambda}(t)$ in Figure 3.10 and Figure 3.11, a preliminary clarification is necessary: the black dotted lines represent the true values of the parameters after the fault, while the colored continuous lines correspond to their estimated values. It can be observed that $\hat{\Lambda}(t)$ is highly sensitive to the presence of disturbances. Furthermore, the off-diagonal elements (Figure 3.11) assume relatively large values and are also noticeably influenced by the disturbance.
In this scenario, the estimation accuracy of $\hat{\Lambda}$ is very limited mainly for two reasons:

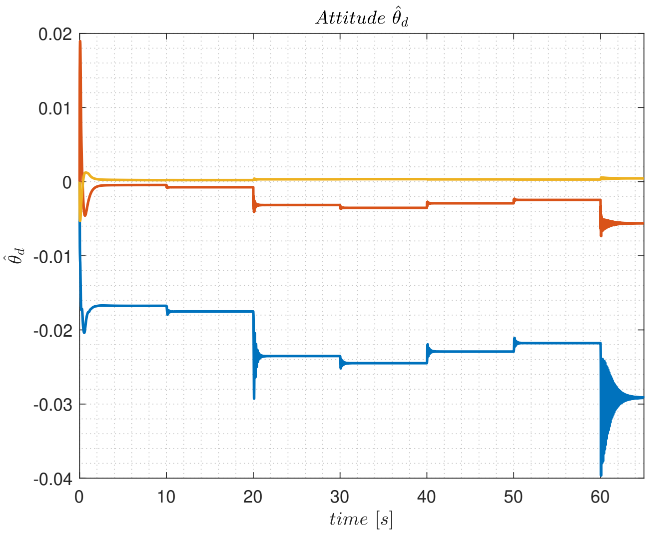

(a) $\hat{\theta}_{d,att}(t)$.

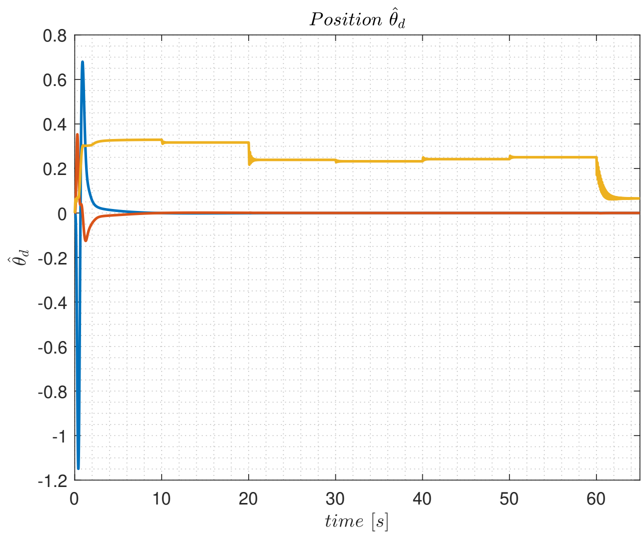

(b) $\hat{\theta}_{d,pos}(t)$.

Figure 3.9: Parameter estimates $\hat{\theta}_{d,att}$ and $\hat{\theta}_{d,pos}$ for the position setpoint simulation in the decoupled case.

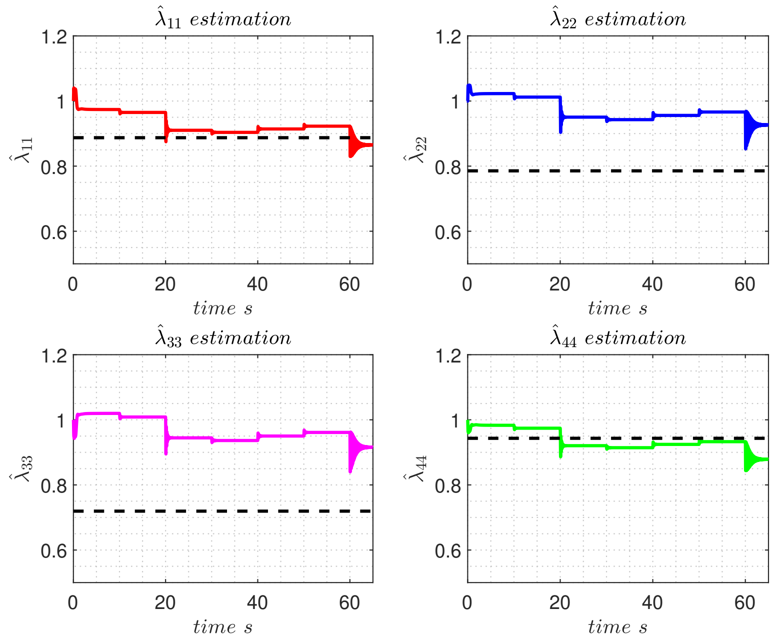

Figure 3.10: Diagonal terms of $\hat{\Lambda}(t)$ for the position setpoint simulation in the decoupled case.

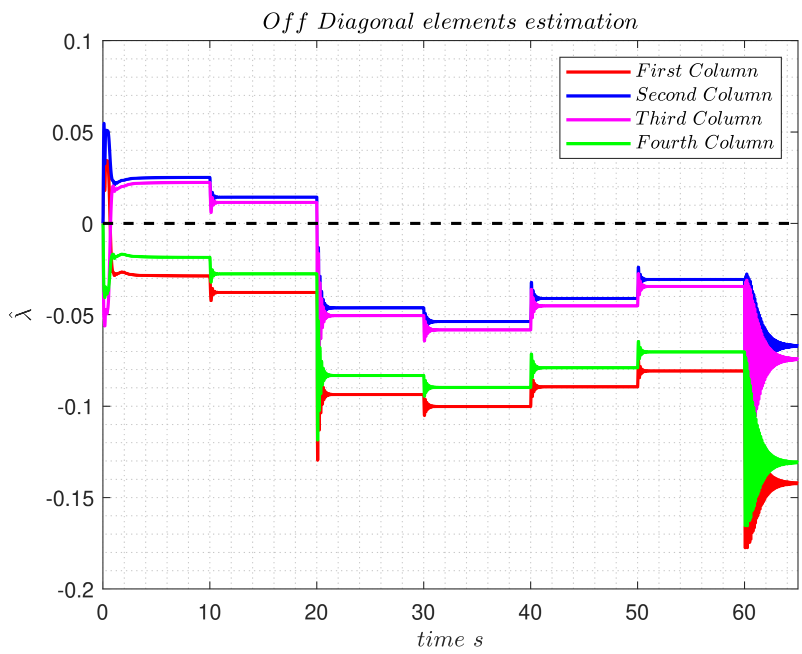

Figure 3.11: Estimates $\hat{\Lambda}$ of the off-diagonal terms of the effectivenss matrix for the position setpoint simulation in the decoupled case.

1. The use of a constant position setpoint results in limited system excitation, thereby reducing the amount of information available for accurate parameter adaptation.
2. The presence of external disturbances negatively affects the precision of the control effectiveness matrix estimation.

Coupled Architecture

Here the results obtained with the augmented controller architecture with a single predictor described in section 2.2 are presented.

An analysis of the rate responses shown in Figure 3.12 indicates that the decoupled controller architecture operates as intended. After a fast initial transient, the plant angular rates converge to and stabilize around the commanded rates, confirming both the rapid response and the effectiveness of the predictor-based control structure. Unlike the decoupled case, yaw rate exhibits a little inverse response with respect to the commanded reference.

Only the initial seconds of the simulation are reported, as this interval corresponds to the transient phase during which the UAV moves toward the desired position setpoint and the angular rates are nonzero. Although the effects of the disturbances are not clearly discernible in the plots due to their relatively small magnitude, they are attenuated sufficiently quickly, and the resulting peaks remain limited.

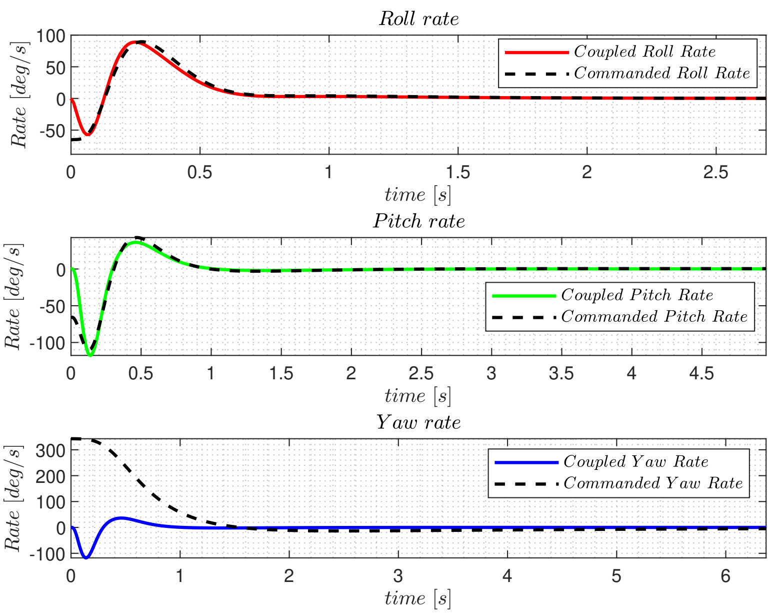

Figure 3.12: Angular rates for the position setpoint simulation in the coupled case.

An examination of the velocity and position responses in Figure 3.13 and in Figure 3.14, respectively, shows that the UAV successfully reaches the desired position setpoint and remains largely unaffected by external disturbances. In particular, the disturbances have only a limited impact on the vertical dynamics, as indicated by the small peaks observed in the z-axis position and velocity.

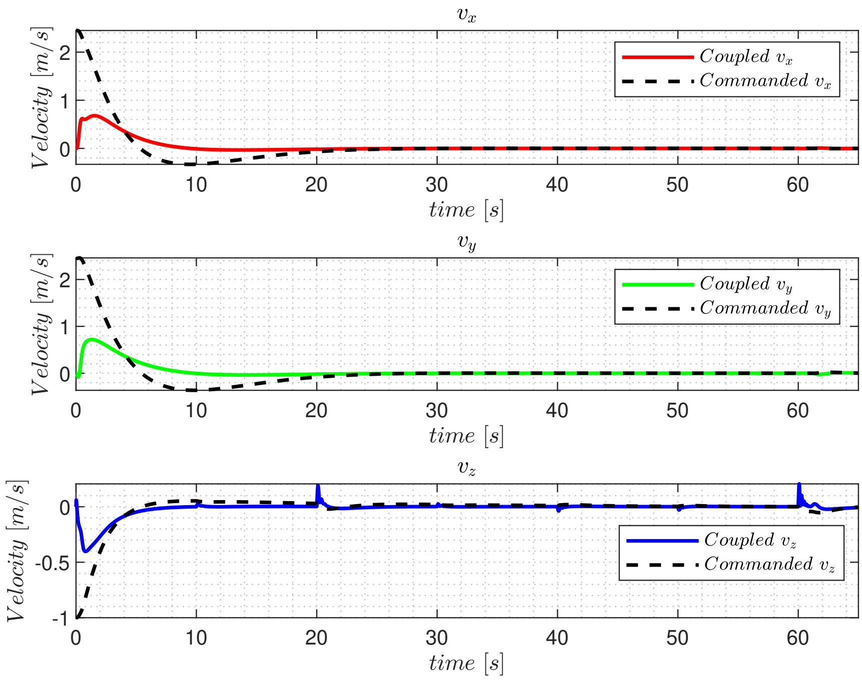

Figure 3.13: Velocity for the position setpoint simulation in the coupled case.

When comparing the Coupled and Decoupled versions in terms of rates, velocity, and position tracking performance, no significant differences are observed.

The state estimation errors (difference between the real state and the one estimated by the predictor) in Figure 3.15 further confirm the effectiveness of the augmented controller. In fact it exhibits a very fast error dynamics (even in the presence of external disturbances), so that the estimated rates $\hat{\omega}_b$ and the estimated velocity $\hat{v}_b$ rapidly converge to the corresponding real values. This demonstrates that the predictor model is able to accurately reconstruct the system states even in the presence of modeling uncertainties and external disturbances.

Finally, the temporal evolutions of the estimated parameters, are analyzed. First, like the Decoupled case, the time evolution of $\hat{\theta}_{Ap}(t)$ is not reported. This choice is motivated by the fact that this parameter is primarily intended to compensate for modeling uncertainties. In the present simulation scenario, where significant external disturbances are

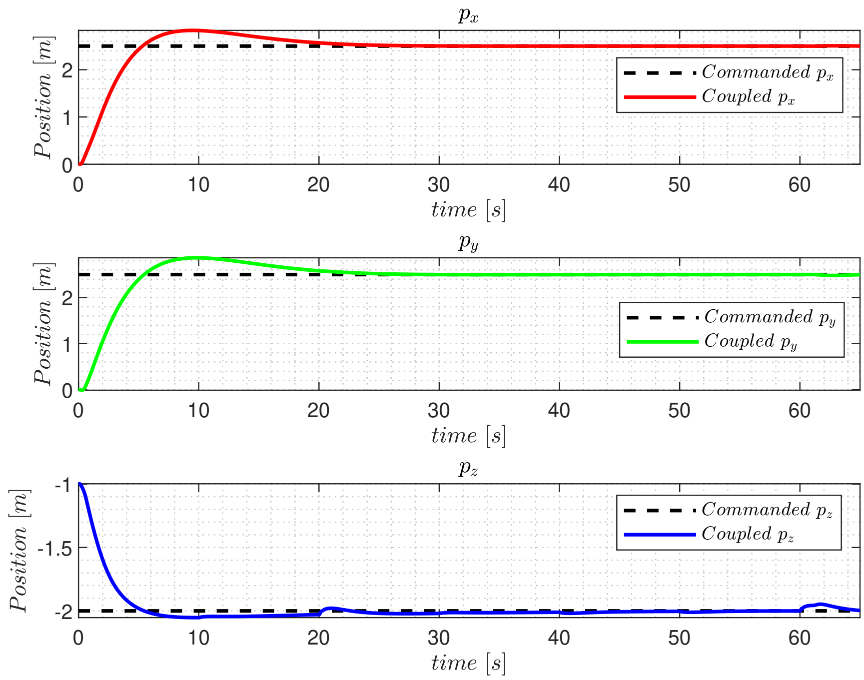

Figure 3.14: Position for the position setpoint simulation in the coupled case.

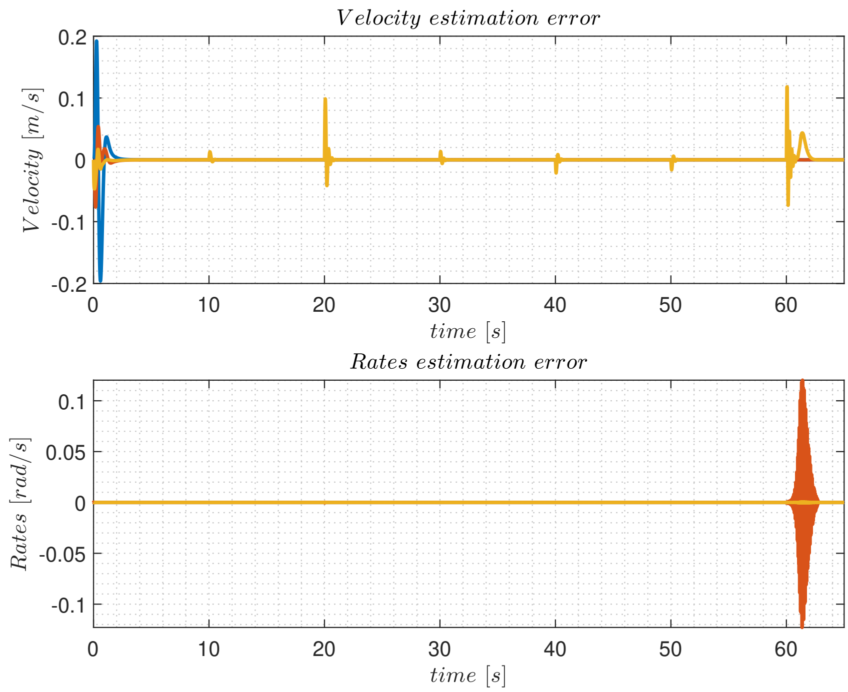

Figure 3.15: Estimated states for the position setpoint simulation in the coupled case.

introduced, it was considered more meaningful to highlight the parameter directly associated with disturbance compensation. Nevertheless, $\hat{\theta}_{Ap}(t)$ exhibits a time evolution that is clearly influenced by the disturbance. This behavior can be explained by the coupling between the parameters associated with modeling uncertainties and those dedicated to disturbance compensation. Even though their roles are conceptually distinct, the adaptation dynamics are interconnected, and variations in one parameter set indirectly affect the other. Instead, the temporal evolutions of the estimated parameters, $\hat{\theta}_d(t)$, and $\hat{\Lambda}(t)$ are reported in Figure 3.16 and Figure 3.17.

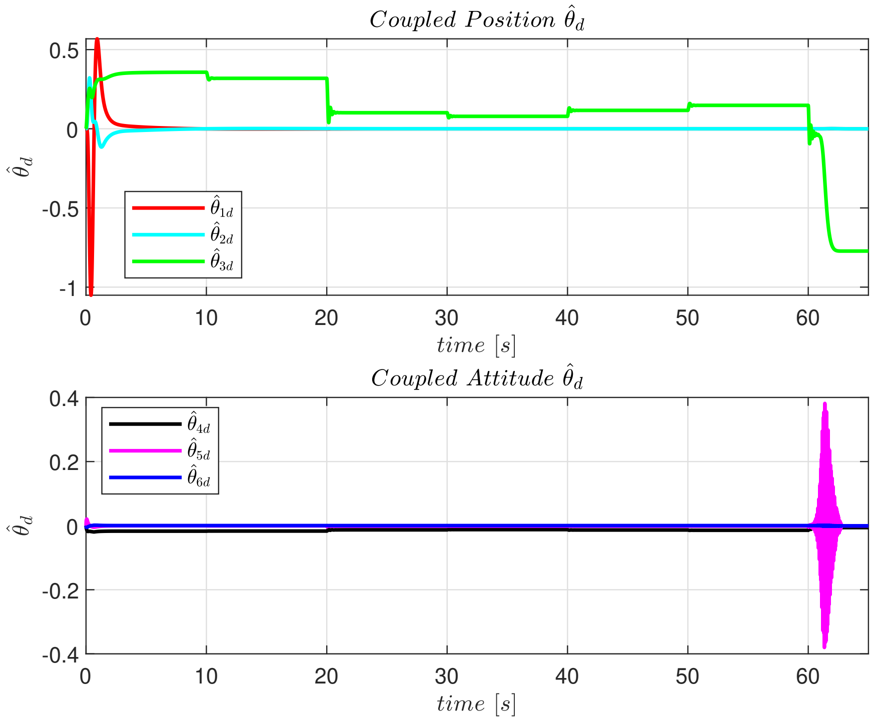

Figure 3.16: Estimate of the position and attitude disturbance $\hat{\theta}_d$ for the position setpoint simulation in the coupled case.

Analyzing the time evolution of $\hat{\theta}_d(t)$ in Figure 3.16, it can be observed that only the component associated with the z-velocity exhibits a waveform resembling the square wave of the disturbance. This is consistent with the nature of the applied disturbance, which primarily acts along the vertical direction. This behavior is fully consistent with the role of this parameter, whose primary objective is to compensate for external disturbances. Consequently, its adaptation closely follows the disturbance profile.

When analyzing the time evolution of $\hat{\Lambda}(t)$ (In this configuration, due to the adoption of the coupled architecture, no off-diagonal elements of the control effectiveness matrix are estimated), a preliminary clarification is necessary: the black dotted lines represent the

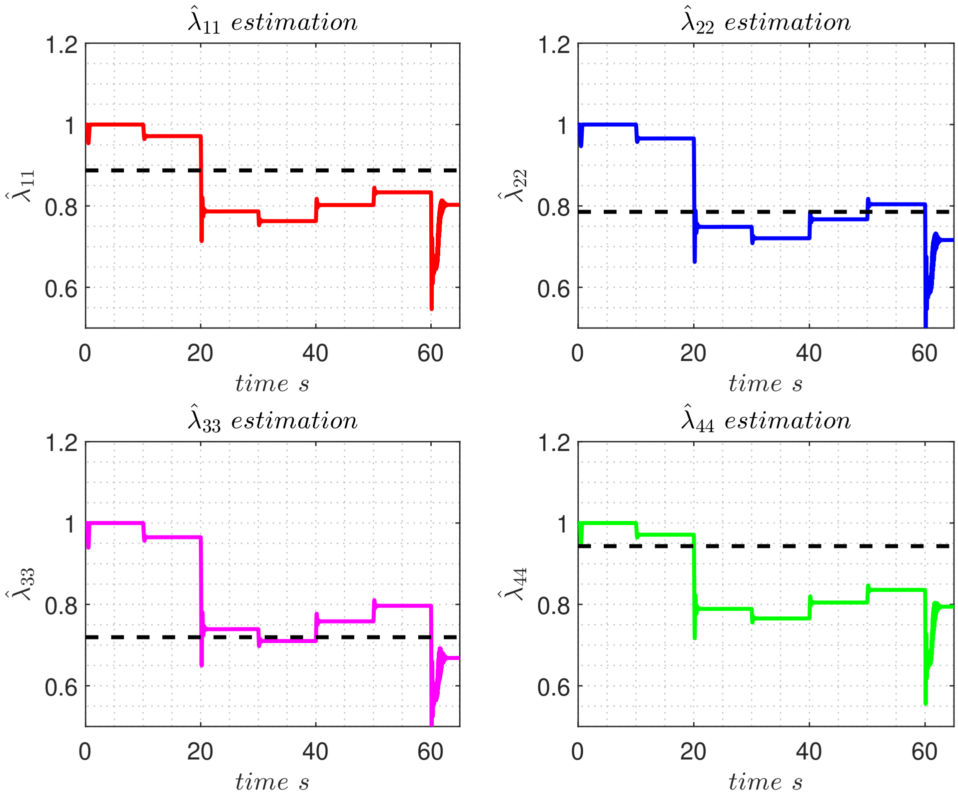

Figure 3.17: Estimate of the effectiveness $\hat{\Lambda}(t)$ for the position setpoint simulation in the coupled case.

true values of the parameters after the fault, while the colored continuous lines correspond to their estimated values. It can also be observed that $\hat{\Lambda}(t)$ is highly sensitive to the presence of disturbances, similarly to the previous case. In this scenario, the estimation accuracy of the diagonal elements of $\hat{\Lambda}$ remains limited, mainly for the same two reasons discussed previously.

3.2.2. Second Simulation: Circular trajectory

In the second simulation, a circular trajectory with radius $r = 2.5\,\mathrm{m}$, period $T = 40s$, and altitude $h = -1\,\mathrm{m}$ is commanded.
The control effectiveness matrix is selected as follows: for the first $10s$, it is chosen as a unit diagonal matrix (corresponding to nominal actuator conditions with no faults), while, after $t = 10s$, an efficiency reduction of the third rotor is introduced in order to simulate an actuator fault:

$$\Lambda = \begin{bmatrix} 1 & 0 & 0 & 0 \\ 0 & 1 & 0 & 0 \\ 0 & 0 & 0.35 & 0 \\ 0 & 0 & 0 & 1 \end{bmatrix}. \tag{3.3}$$

The total simulation time is set to $40s$, and no external disturbances are considered in this scenario.
Also for this simulation, only the responses obtained with the two augmented controllers are reported, while those of the baseline controller are omitted. This decision is taken because the poor performance of the baseline controllor under such severe fault causes the simulated drone to crash.

The results are again presented for the two considered architectures. The first architecture employs two decoupled predictors, one for the position dynamics and one for the attitude dynamics, as described in Section 2.3. The second architecture adopts a single predictor, and therefore a single augmentation scheme, as presented in Section 2.2.

Decoupled Architecture

Here the results produced by the two decoupled adaptive augmentations described in Section 2.3 are presented.

By examining the rate responses in Figure 3.18, it is clearly visible that, before the fault occurrence, the Decoupled controller architecture operates correctly. In fact, the plant angular rates closely match the commanded references.

After the occurrence of the actuator fault at $t = 10\,\mathrm{s}$, the tracking performance remains satisfactory. The plant rates continue to closely follow the commanded ones, and the transient induced by the fault is rapidly attenuated. This indicates that the augmented controller is capable of adapting to changes in the control effectiveness matrix, maintaining both stability and tracking performance despite the sudden degradation of one actuator.

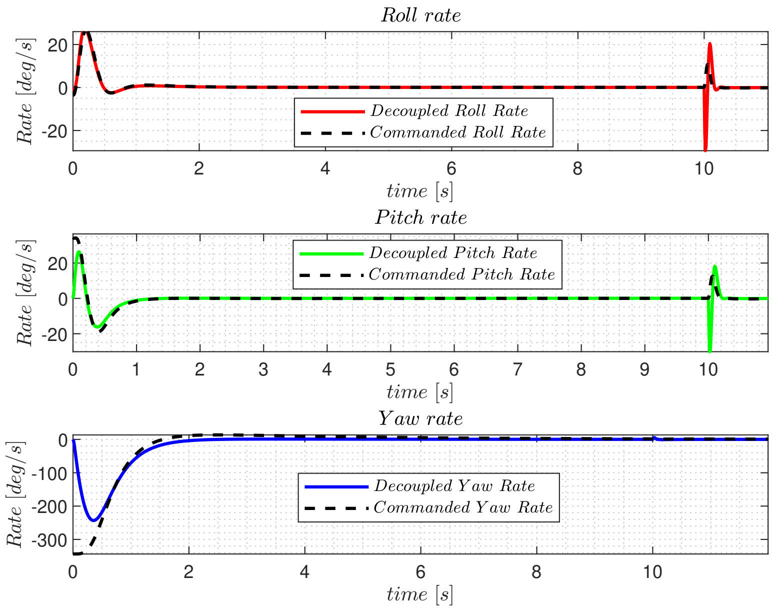

Figure 3.18: Angular rates for the circular setpoint simulation in the decoupled case.

A similar behavior can be observed when analyzing the velocity and position responses in Figure 3.19 and in Figure 3.20. During the initial fault-free phase, the adaptive controller achieves accurate tracking of the reference trajectory, with negligible differences between the plant velocity and the commanded one. After the fault occurrence, the overall tracking performance remains satisfactory, and the loss of altitude caused by the actuator degradation is negligible.

The state estimation errors (difference between the real states and the ones estimated by the predictor) in Figure 3.21 further confirm the effectiveness of the augmented controllers. In fact, it exhibits a very fast error dynamics, so that the estimated rates $\hat{\omega}_b$ and the estimated velocity $\hat{v}_b$ rapidly converge to the corresponding real values. This demonstrates that the predictor model remains accurate even in the presence of actuator faults and that the adaptive structure is able to preserve good state reconstruction properties.

It is also interesting to analyze in Figure 3.22 the thrust generated by each propeller during the simulation. It can be observed that the third propeller provides a significantly

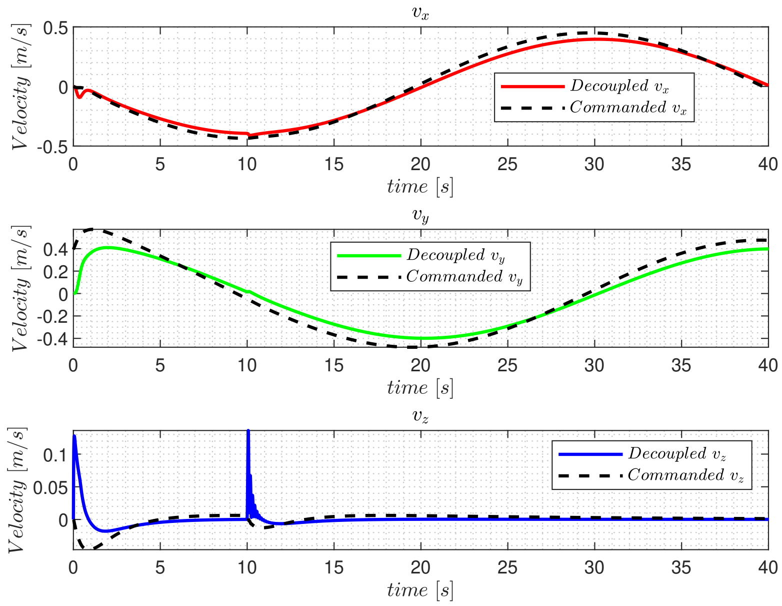

Figure 3.19: Velocity for the circular setpoint simulation in the decoupled case.

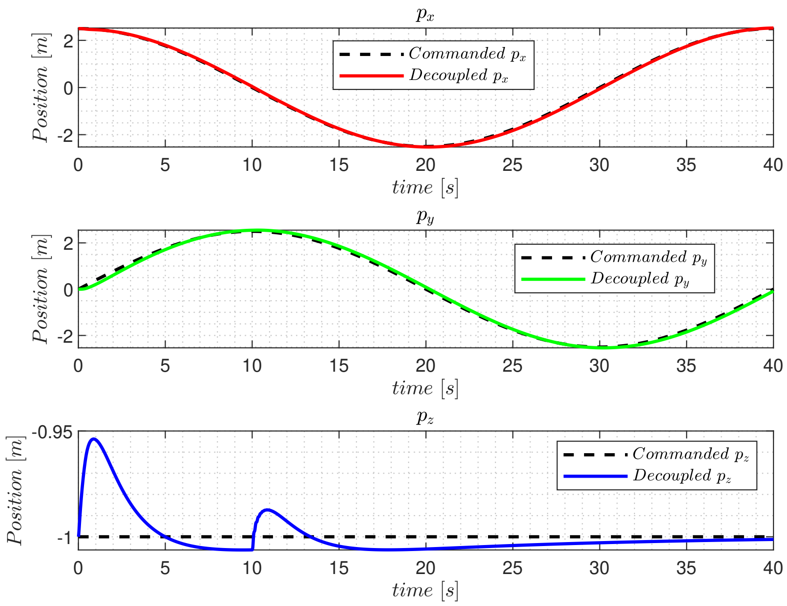

Figure 3.20: Position for the circular setpoint simulation in the decoupled case.

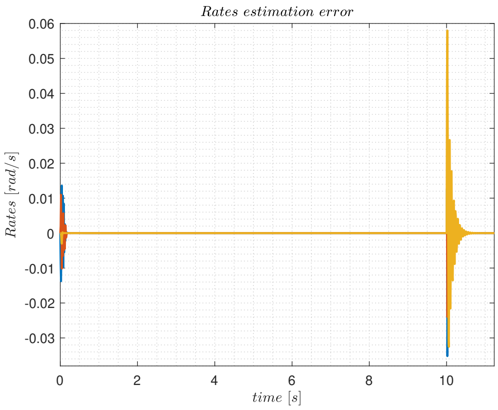

(a) Rates state estimation error zoom.

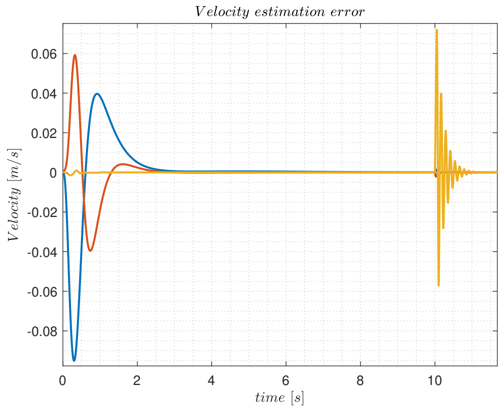

(b) Velocity State Estimation Error zoom.

Figure 3.21: State estimation error for the circular setpoint simulation in the decoupled case.

higher thrust than the other three, which exhibit similar thrust levels. This behavior is coherent with the reduced efficiency of the third rotor and reflects the ability of the control allocation algorithm to redistribute the control effort among the available actuators in order to compensate for the fault.

Finally, the time evolution of the estimated parameters is analyzed.

First, since no external disturbances are considered in this scenario, the disturbance-related parameters $\hat{\theta}_{d,i}(t)$ are neither included in the analysis nor updated during the simulation.

Second, the time histories of $\hat{\theta}Ap, att(t)$ and $\hat{\theta}Ap, pos(t)$ are not reported. This choice is motivated by the fact that these parameters depend exclusively on modeling uncertainties, which are relatively small in the present case. Consequently, the magnitude of their adaptation remains limited and does not provide particularly informative insight when plotted.

Nevertheless, the estimation accuracy of these parameters is very high, and their convergence to the true values can be regarded as essentially exact.

The time evolution of $\hat{\Lambda}(t)$ is reported in Figure 3.23.

When analyzing the time evolution of $\hat{\Lambda}(t)$, a preliminary clarification is necessary: the black dotted lines represent the true values of the parameters after the fault, while the colored continuous lines correspond to their estimated values. As expected, $\hat{\Lambda}(t)$ exhibits negligible variation during the first 10 s, since no actuator faults are present in this initial phase. After the occurrence of the fault, all estimates undergo a rapid adaptation

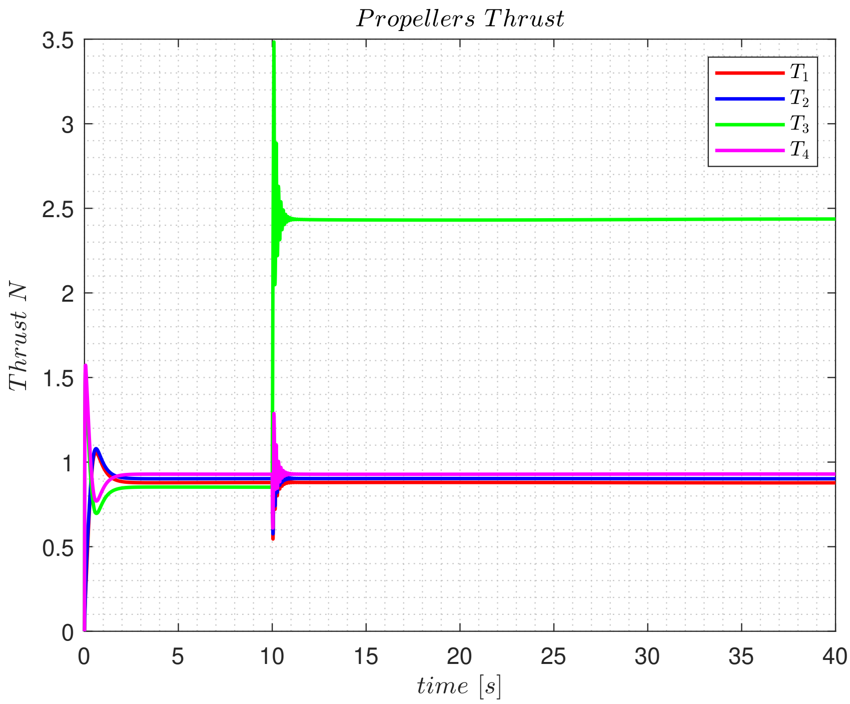

Figure 3.22: Propellers' thrust for the circular setpoint simulation in the decoupled case.

process and converge to new steady-state values. The estimation accuracy of $\hat{\Lambda}(t)$ is satisfactory: in particular, the efficiency reduction of the third actuator is almost perfectly identified, while the efficiencies of the remaining three actuators are slightly overestimated (Figure 3.23a). Furthermore, the off-diagonal elements in Figure 3.23b assume relatively small values.

Unlike the previous simulation, where the presence of disturbances negatively affected the estimation accuracy, in this case the absence of external disturbances allows for a significantly more accurate reconstruction of Λ.

Coupled Architecture

Here the results produced by the augmented controller architecture with only one predictor are presented.

By examining the responses of the angular rates, velocity and position in Figure 3.24, Figure and Figure , it can be seen that the Coupled controller architecture operates correctly. After the fault occurrence, the overall tracking performance remains satisfactory, and the loss of altitude caused by the actuator degradation is negligible.

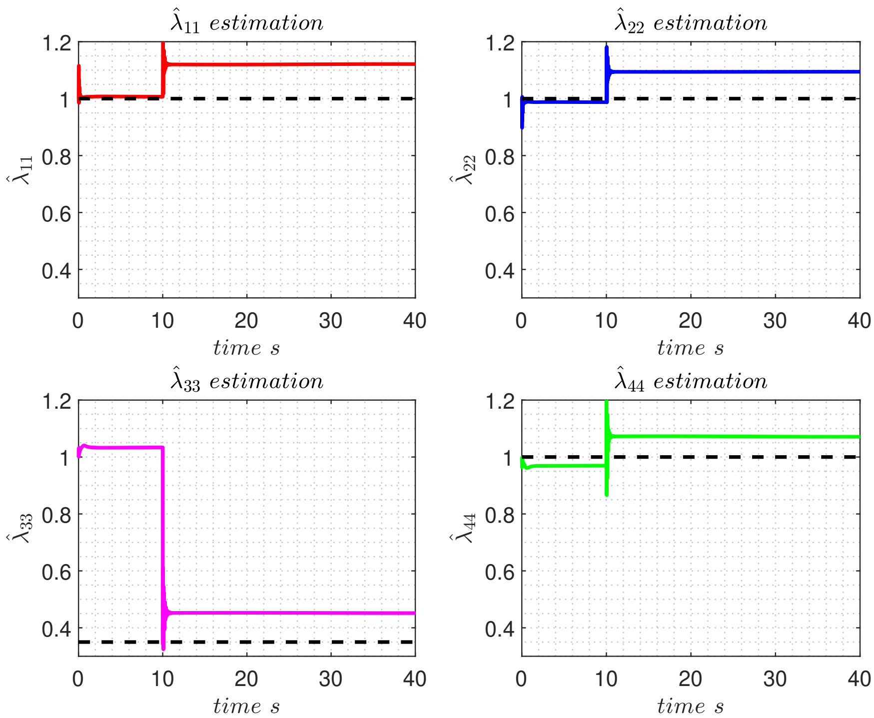

(a) Diagonal terms of $\hat{\Lambda}(t)$.

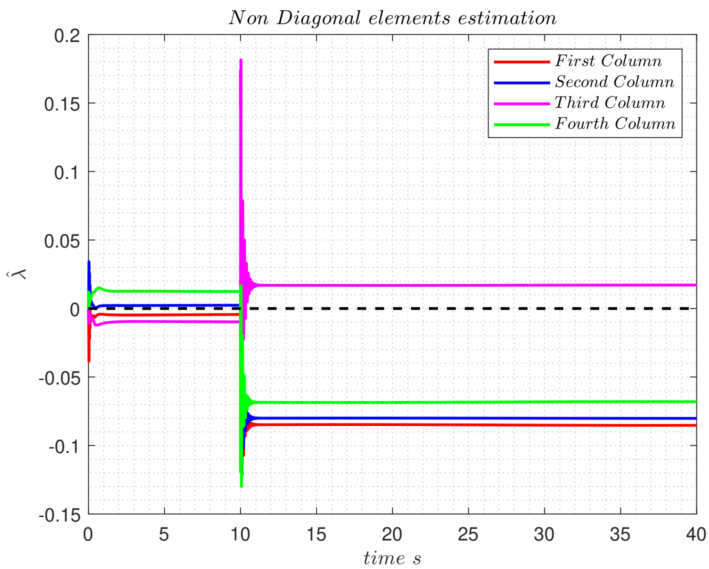

(b) Off-diagonal terms $\hat{\Lambda}(t)$.

Figure 3.23: Estimates $\hat{\Lambda}$ of the diagonal and off-diagonal terms of the effectivenss matrix for the circular setpoint simulation in the decoupled case.

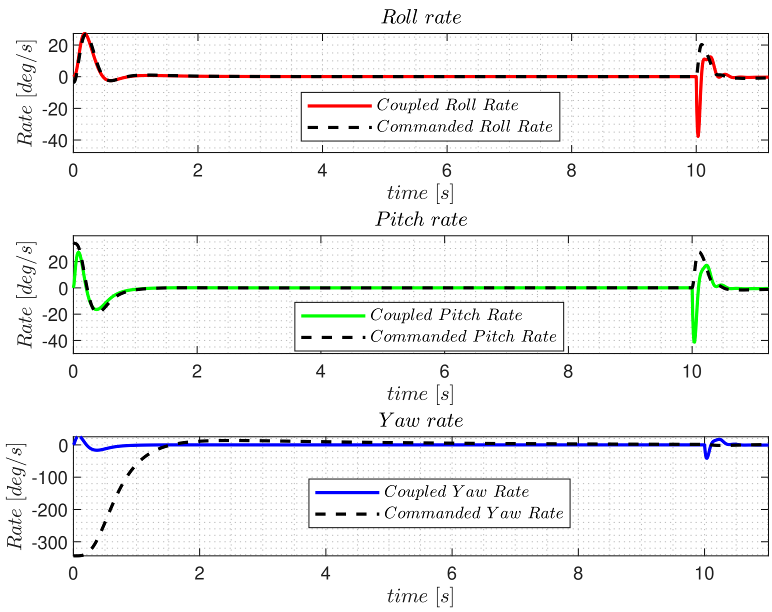

Figure 3.24: Angular rates for the circular setpoint simulation in the coupled case.

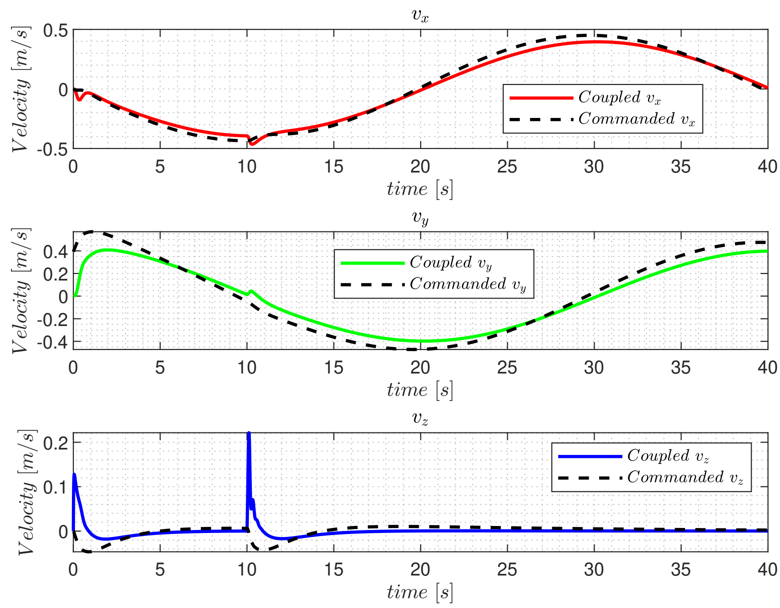

Figure 3.25: Velocity for the circular setpoint simulation in the coupled case.

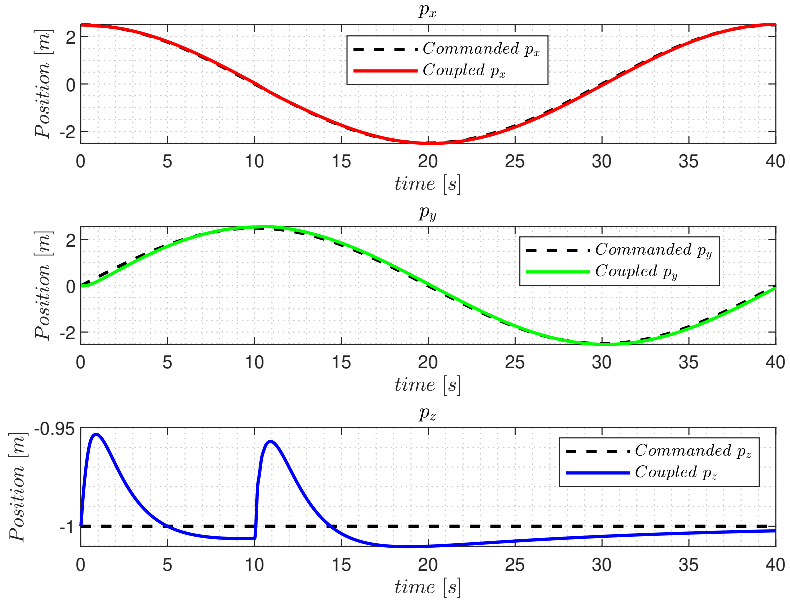

Figure 3.26: Position for the circular setpoint simulation in the coupled case.

When comparing the Coupled and Decoupled versions in terms of rates, velocity, and position tracking performance, no significant differences are observed. However, a small difference can be observed along the vertical direction. In particular, in the Coupled version, a slightly larger peak appears in the z-position, after the fault, with respect to the Decoupled version. Although this peak is negligible in absolute terms and does not compromise stability or safety, it is larger than the one observed with the Decoupled versions. This suggests that, in the Coupled version, the coupling between attitude and position dynamics may slightly reduce the effectiveness of the disturbance and fault compensation along the vertical axis.

The state estimation errors (difference between the real state and the ones estimated by the predictor) in Figure 3.27 further confirm the effectiveness of the augmented controller. In fact, it exhibits a very fast error dynamics, so that the estimated rates $\hat{\omega}_b$ and the estimated velocity $\hat{v}_b$ rapidly converge to the corresponding real values. This demonstrates that the predictor model is able to accurately reconstruct the system states even in the presence of modeling uncertainties.

Like for the Decoupled version, the time evolution of $\hat{\theta}_{Ap}(t)$ is not reported. This choice is motivated by the fact that this parameter depends exclusively on modeling uncertainties, which in this scenario are relatively small. Consequently, the magnitude of its adaptation remains limited and does not provide particularly insightful information for graphical

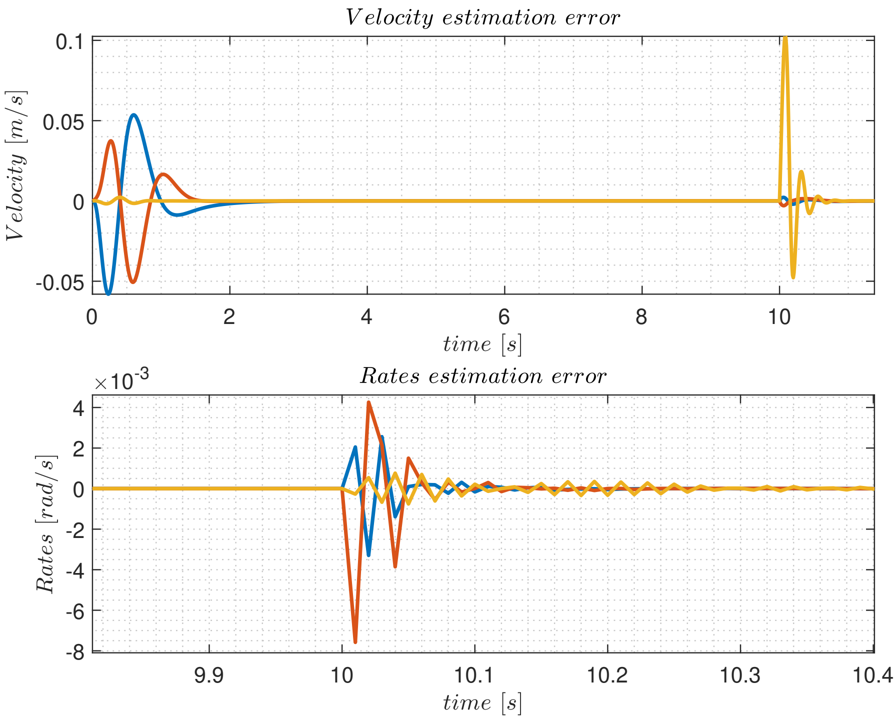

Figure 3.27: State estimation error for the circular setpoint simulation in the coupled case.

representation. Nevertheless, the estimation accuracy of this parameter is not as high as in the previous case, and its convergence to the true values cannot be considered equally good.
Moreover, differently from the previous case, $\hat{\theta}_d(t)$, although not explicitly reported, cannot be neglected in the analysis. Indeed, neglecting this parameter would result in nonzero steady-state estimation errors for the yaw rate and vertical velocity.

Finally, the temporal evolution of the estimated parameter $\hat{\Lambda}(t)$ is shown in Figure 3.28

As expected, $\hat{\Lambda}(t)$ shows no significant variation during the first 10 s, as there are no actuator faults in this initial phase. After the occurrence of the fault, all estimates undergo a rapid adaptation process and converge to new steady-state values. The estimation accuracy of $\hat{\Lambda}(t)$ can be considered overall satisfactory; however, the efficiency reduction of the third actuator is not estimated with the same level of accuracy observed in the Decoupled case, while the efficiencies of the remaining three actuators are slightly underestimated.

When comparing the Decoupled and Coupled versions, it can be observed that the estimation accuracy of the control effectiveness matrix is superior in the Decoupled architecture. This confirms that persistent excitation induced by the circular trajectory, together with

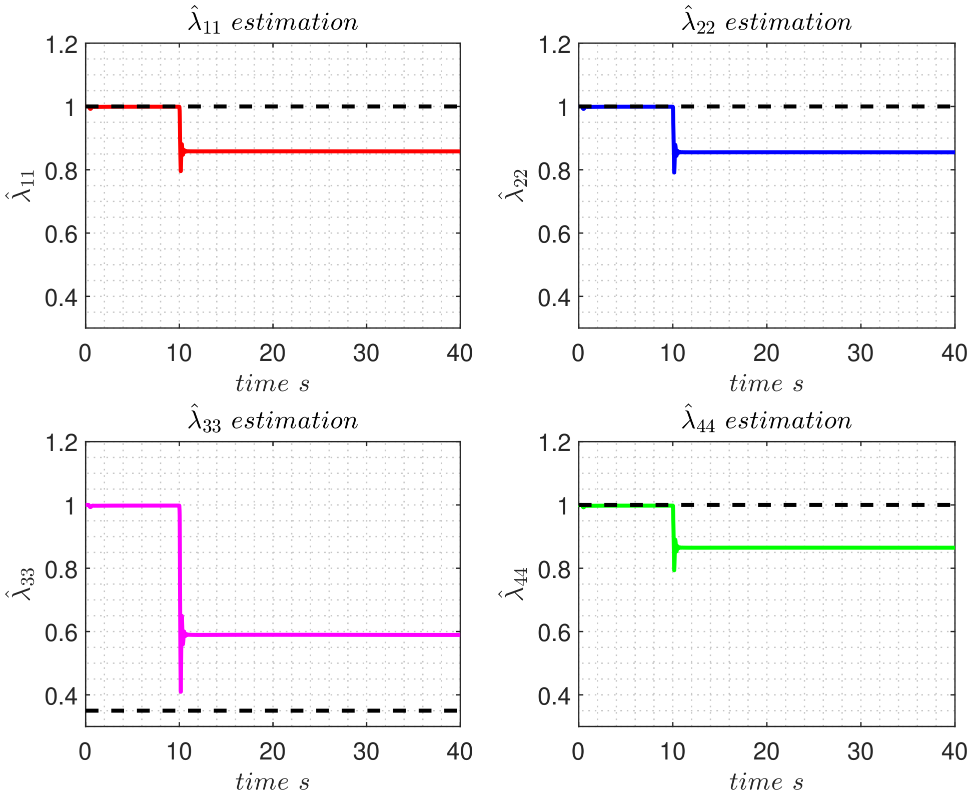

Figure 3.28: Estimate of the effectiveness $\hat{\Lambda}$ for the circular setpoint simulation in the coupled case.

reduced parameter coupling effects, improves the identifiability of the control effectiveness parameters.

4 | Experimental results

In this chapter, experimental validation on the physical vector-thrust quadrotor UAV shown in Figure 4.1 and built by ANT-X [26] are presented.
The drone dynamics is described by the same equations introduced in (2.1), with the only difference being the nominal values of the parameters, which slightly differ from those used in simulation. In practice, the real parameter values are not perfectly known and are therefore assumed based on available information. Only the first version (*i.e.*,

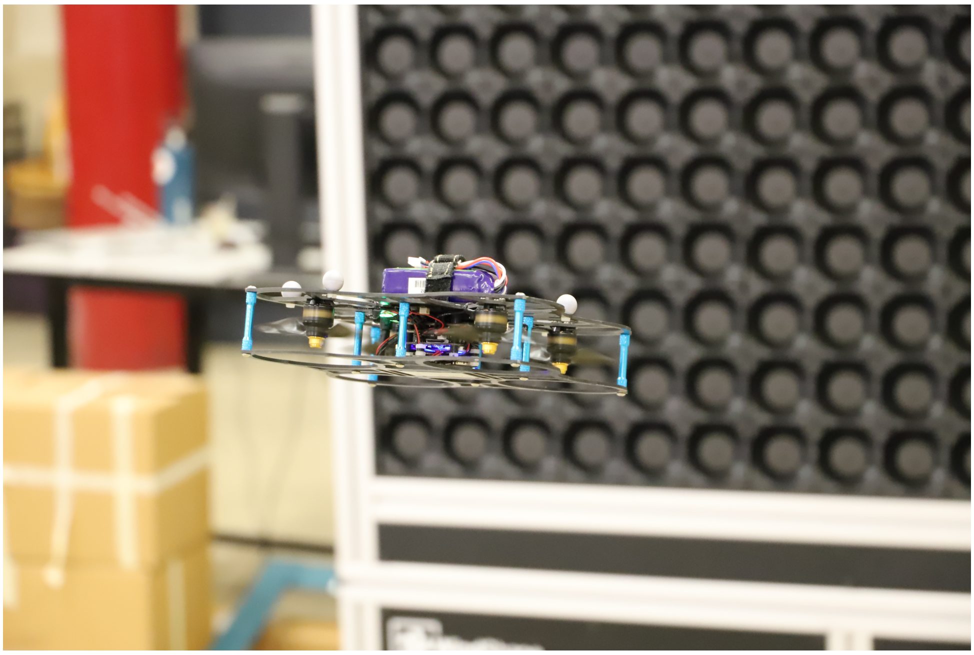

Figure 4.1: ANT-X drone.

the decoupled formulation) of the Augmented P-MRAC controller has been implemented on the physical platform. This choice was motivated by the difficulty in achieving an acceptable tuning for the Coupled version. In particular, when the adaptation gains were selected too small, the augmented controller had a negligible effect on the system behavior; conversely, when the gains were increased, the closed-loop system became unstable, and the drone exhibited uncontrollable behavior.
Whenever possible, the experimental results obtained with the augmented controller are

compared with those achieved using the baseline controller.
Before presenting and discussing the experimental results, a retuning of the Augmented P-MRAC controller parameters is required.
The gains used in the experimental implementation are reported in (4.1).

$$\begin{aligned}
\Gamma_{\Lambda_{att}} &= 1e^{-4} \cdot \text{diag}([1,1,1]) \\
\Gamma_{\theta_{Ap_{att}}} &= 5e^{-6} \cdot \text{diag}([1,1,1,1]) \\
\Gamma_{\theta_{d_{att}}} &= 1e^{-7} \cdot \text{diag}([1,1,1,1]) \\
L_{att} &= 10 \cdot \text{diag}([1,1,1]) \\
\theta_{M_{att}} &= 2e^{-3} \cdot \begin{bmatrix} 0.18 & 0.12 & 0.09 \end{bmatrix}^\top \\
\epsilon_{att} &= 0.2 \\
\Gamma_{\Lambda_{pos}} &= 0.1 \cdot \text{diag}([1,1,1]) \\
\Gamma_{\theta_{Ap_{pos}}} &= 1 \cdot \text{diag}([1,1,1,1]) \\
\Gamma_{\theta_{d_{pos}}} &= 1 \cdot \text{diag}([1,1,1,1]) \\
L_{pos} &= 10 \cdot \text{diag}([1,1,1]) \\
\theta_{M_{pos}} &= \begin{bmatrix} 0.04 & 0.04 & 0.055 \end{bmatrix}^\top \\
\epsilon_{pos} &= 0.2
\end{aligned} \tag{4.1}$$

It can be observed that the gains associated with the position dynamics subsystem are comparable to those used in the simulation studies, while the gains associated with the attitude dynamics subsystem are significantly smaller.

4.1. Hoovering condition without external disturbance

In the first experimental campaign, actuator faults on different rotors have been injected while the drone was in hover conditions without external disturbances affecting it. In particular, two different cases are analyzed:

- **First case:** a sudden efficiency reduction of 30% is applied to all rotors (*i.e.*, $\lambda_i = 0.7$ for all i), with the Augmented P-MRAC controller enabled and disabled.
- **Second case:** a sudden efficiency reduction of 40% is applied to the third rotor only (*i.e.*, $\lambda_3 = 0.6$), with the Augmented P-MRAC controller enabled and disabled.

4.1.1. First Case: Hovering with degradation of all rotors

In this case, a sudden efficiency reduction of 30% is applied simultaneously to all rotors while the ANT-X drone is in hovering conditions. The experiment is performed both with the Augmented P-MRAC controller enabled and with the adaptive augmentation disabled.

First, a comparison between the two configurations is carried out in terms of velocity and position responses.

From the position response in Figure 4.2, it can be clearly observed that the augmented controller outperforms the baseline controller. In particular, the Augmented P-MRAC controller allows the ANT-X drone to remain closer to ideal hovering conditions, whereas the baseline controller exhibits transients with larger errors.

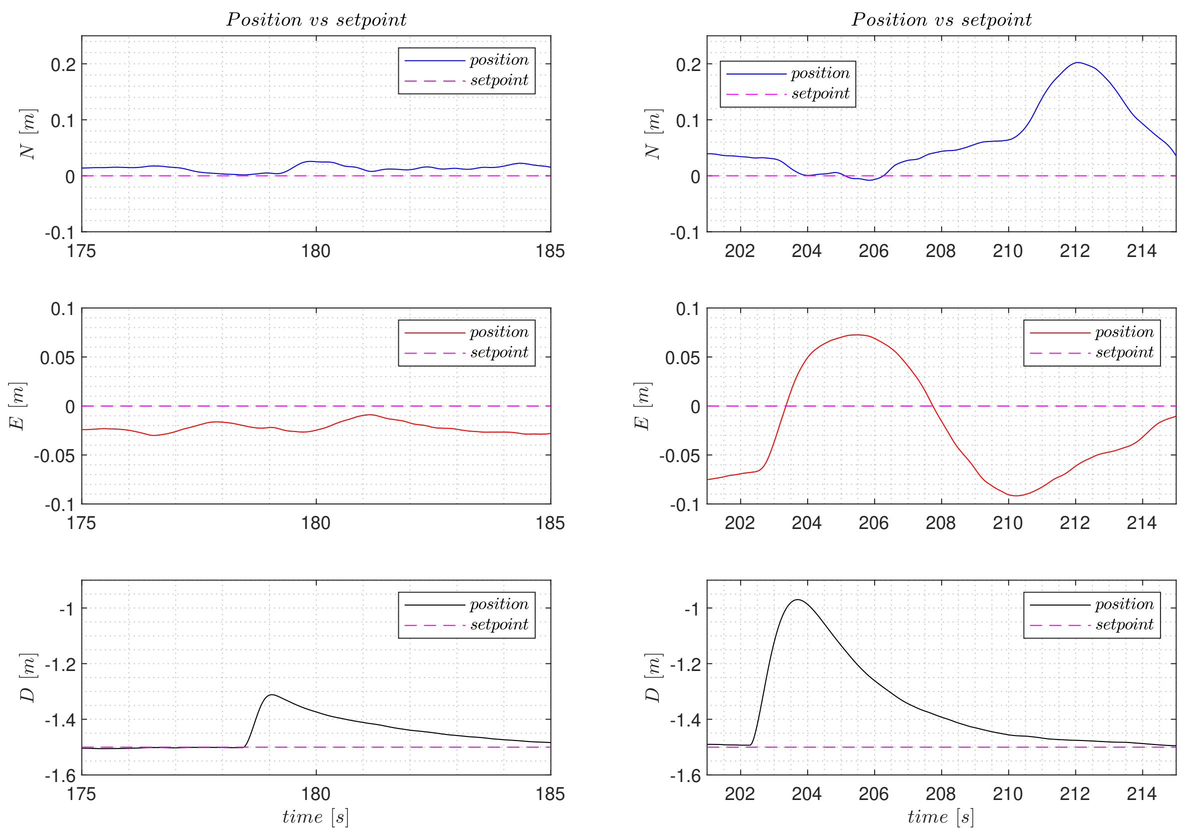

(a) Position Augmented (b) Position Baseline

Figure 4.2: North, East, Down position for the experiment with degradation of all rotors without external disturbance.

In the augmented case, the fault occurs at approximately $t \approx 178\,\mathrm{s}$, resulting in a measured altitude loss of about 18 cm. No significant horizontal displacement is observed. In the baseline case, the fault occurs at approximately $t \approx 202\,\mathrm{s}$, and the corresponding altitude loss is substantially larger, reaching approximately 54 cm, which is about three times greater than in the augmented case. A slightly larger horizontal displacement is also observed.

An analysis of the velocity responses in Figure 4.3 further highlights the robustness and fault-recovery capabilities of the Augmented P-MRAC controller. Compared to the baseline controller, it exhibits a faster recovery transient and significantly reduced velocity deviations when re-establishing the hovering condition (zero velocity), indicating an improved ability to promptly reject faults and restore nominal operation.

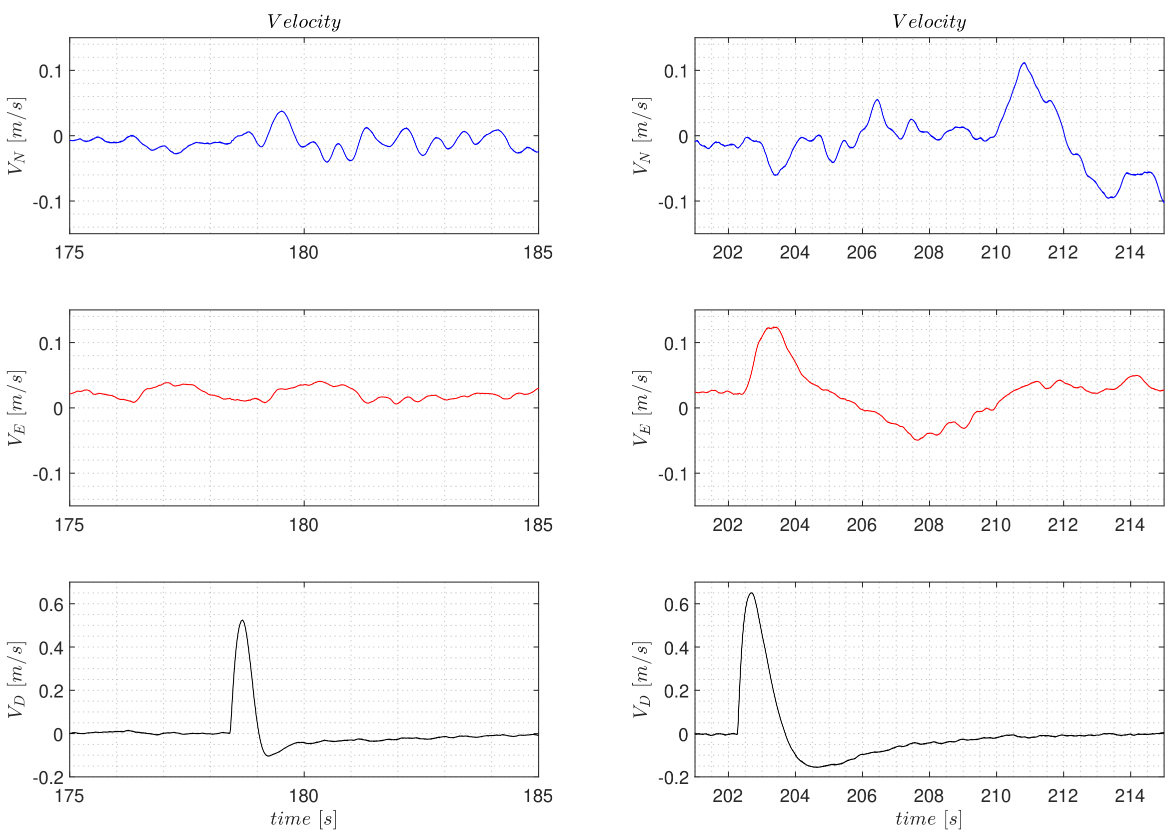

(a) Velocity Augmented. (b) Velocity Baseline.

Figure 4.3: Velocity for the experiment with degradation of all rotors without external disturbance.

In conclusion, the transient required to restore hovering conditions after the fault is noticeably shorter in the adaptive case. Specifically, the recovery time with the Augmented P-MRAC controller is approximately twice as fast as that observed with the baseline controller. This clearly highlights the benefit of the adaptive augmentation in compensating for actuator efficiency losses.

The time evolution of the adaptive control inputs is analyzed in Figure 4.4. The third adaptive force component is nonzero even before the fault occurrence. Its behavior is mainly due to the compensation of disturbances, aerodynamic effects, and unmodelled dynamics related to the battery voltage. After the fault, $f_{z,\text{adpt}}$ exhibits a rapid variation, characterized in particular by an increase in the vertical force component in order to compensate for the loss of efficiency affecting all rotors.
Regarding the adaptive moments, their magnitude remains relatively small. This is consistent with the considered operating condition, namely hovering with a uniform efficiency reduction applied to all actuators. Under such symmetric degradation, no significant moment imbalance is generated, and therefore large variations in the adaptive moment components are neither required nor observed.

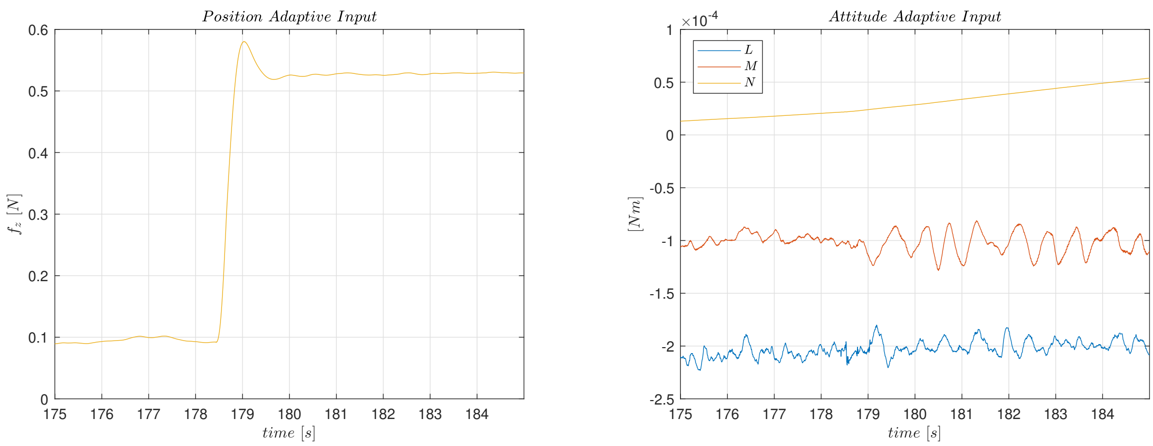

(a) Adaptive forces. (b) Adaptive moments.

Figure 4.4: Adaptive inputs for the experiment with degradation of all rotors without external disturbance.

Finally, it is interesting to analyze the time evolution of the parameter $\hat{\Lambda}$ shown in Figure 4.5 where the dotted lines represent the true parameter values after the fault occurrence, whereas the continuous lines correspond to their estimated values..

During the initial phase, when no actuator faults are present, $\hat{\Lambda}(t)$ exhibits only minor deviations from its nominal value (equal to 1 for the diagonal elements and 0 for the off-diagonal ones). After the fault occurrence, all estimates undergo a rapid adaptation

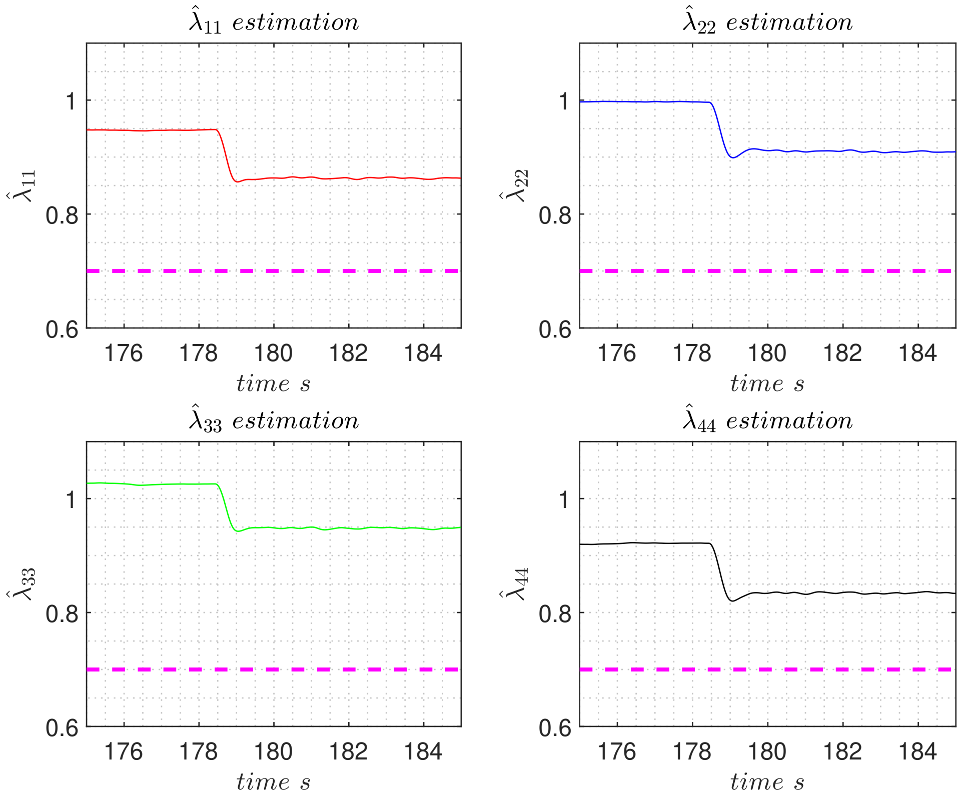

(a) Estimates of the diagonal terms of $\hat{\Lambda}(t)$.

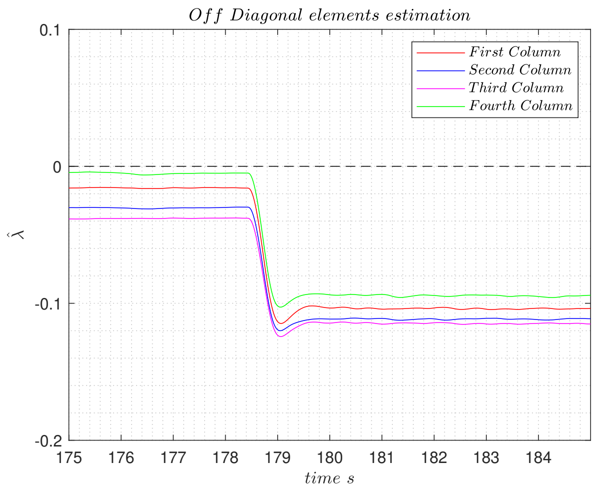

(b) Estimates of the off-diagonal terms of $\hat{\Lambda}(t)$.

Figure 4.5: Estimated effectiveness $\hat{\Lambda}(\mathrm{t})$ for the experiment with degradation of all rotors without external disturbance.

process and converge toward new steady-state values. The estimation accuracy of the diagonal elements of $\hat{\Lambda}(t)$ can be considered overall satisfactory, although the true efficiency reduction is not perfectly reconstructed and the the off-diagonal elements assume relatively larger values after the fault compared to their true values.

Considering that this experiment is conducted on a physical platform under real operating conditions, the obtained estimates of Λ can be regarded as sufficiently accurate, especially when accounting for the unavoidable presence of measurement noise, unmodeled dynamics, and external disturbances.

4.1.2. Second Case: Degradation of the third rotor

In this case, a sudden efficiency reduction of 40% is applied to the third rotor (*i.e.*, $\lambda_3 = 0.6$) while the ANT-X drone is in hovering conditions. The experiment is performed both with the Augmented P-MRAC controller enabled and with the adaptive augmentation disabled.

First, a comparison between the two configurations is carried out in terms of velocity and position responses. From the position response in Figure 4.6 and the velocity response in Figure 4.7, it can be clearly seen that the augmented controller outperforms the baseline controller. In the augmented case, the fault occurs at approximately $t = 238\,\mathrm{s}$, the horizontal displacements are larger (about $-30\,\mathrm{cm}$ along North and $30\,\mathrm{cm}$ along East), while the altitude loss is comparable to the simulated one (approximately 10cm). In the baseline case, the fault occurs at approximately $t = 268\,\mathrm{s}$, the drone exhibits a displacement of about $1.4\,\mathrm{m}$ along the North direction and $-1.1\,\mathrm{m}$ along the East direction, together with an altitude loss of approximately $20\,\mathrm{cm}$. As it is clearly visible, the Augmented P-MRAC controller allows the ANT-X drone to remain closer to ideal hovering conditions, whereas the baseline controller exhibits a slower response with larger deviations.

Therefore, the transient required to restore hovering conditions after the fault is noticeably shorter in the adaptive case. Specifically, the recovery time with the Augmented P-MRAC controller is approximately twice as fast as that observed with the baseline controller. This clearly highlights the benefit of the adaptive augmentation in compensating for actuator efficiency losses.

The time evolution of the adaptive control inputs are analyzed in Figure 4.8. After the occurrence of the fault, the third component of the adaptive force vector f_{adpt} exhibit an oscillatory behavior. Following a transient phase, it converges toward new steady-state value required to compensate for the efficiency reduction affecting the third rotor.

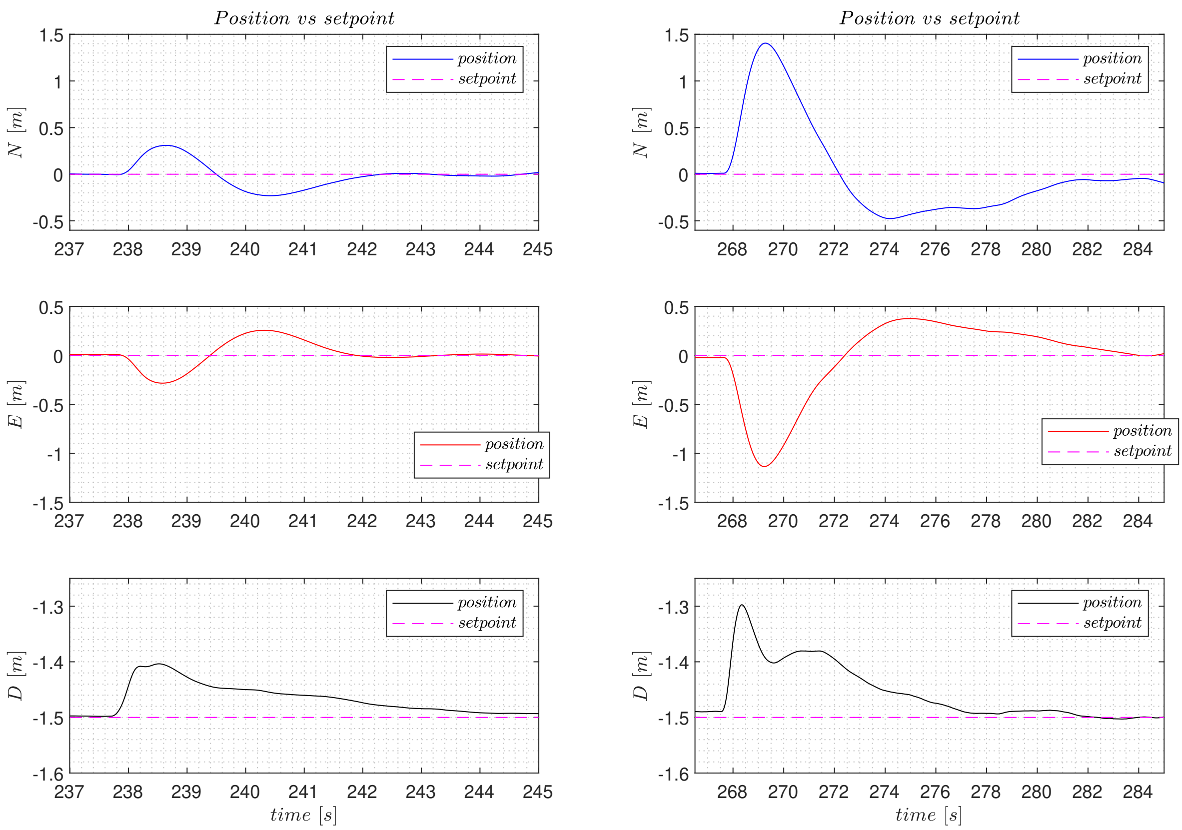

(a) Position Augmented.

(b) Position Baseline.

Figure 4.6: North, East, Down position for the experiment with degradation of the third rotor without external disturbance.

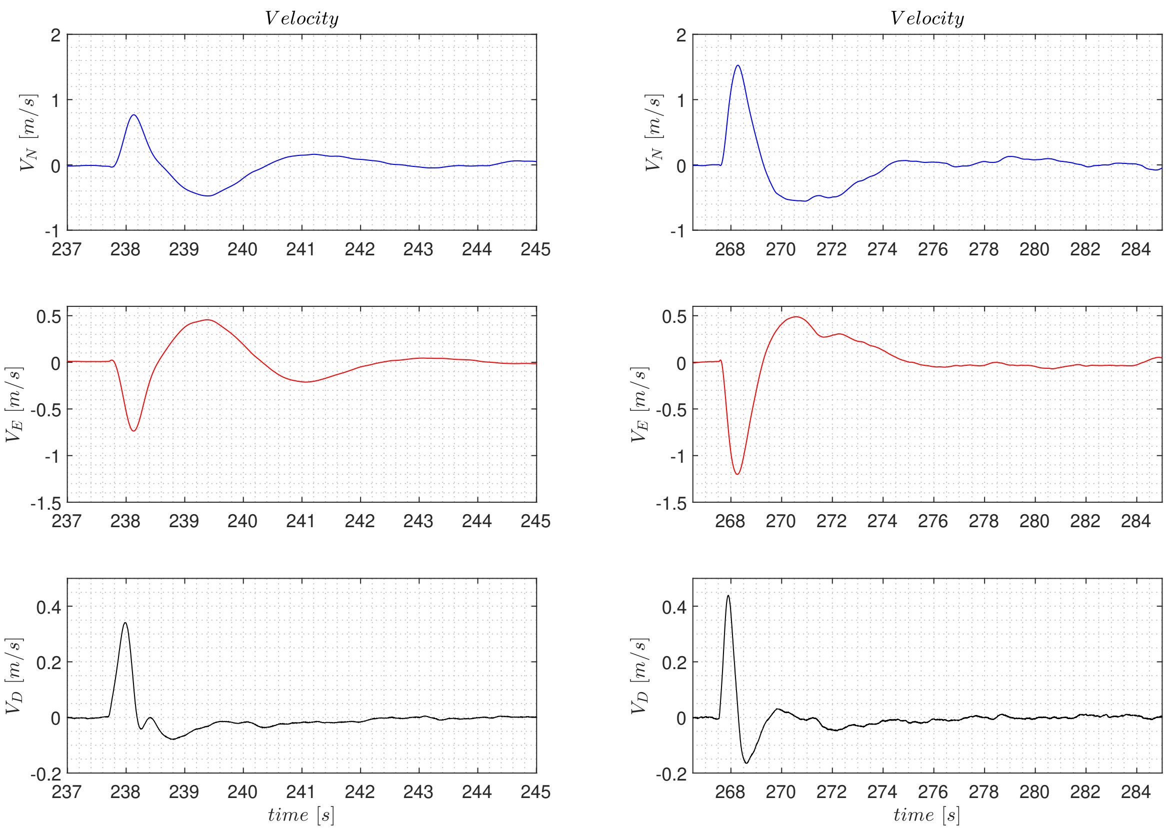

(a) Velocity Augmented.

(b) Velocity Baseline.

Figure 4.7: North, East, Down velocity for the experiment with degradation of the third rotor without external disturbance.

Regarding the adaptive moments, their magnitude remains relatively small overall. A brief transient increase is observed immediately after the fault occurrence, corresponding to the compensation of the moment imbalance generated by the third rotor degradation.

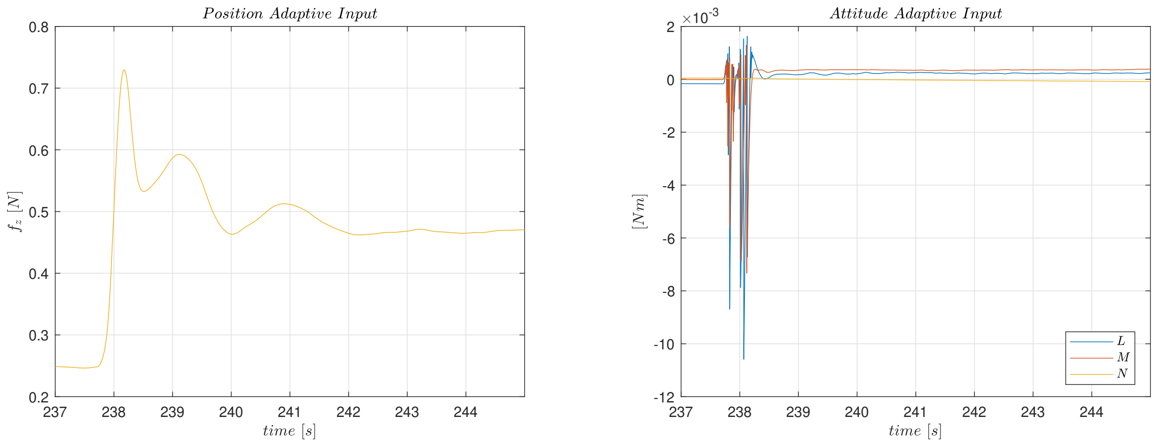

(a) Adaptive forces (b) Adaptive Moments

Figure 4.8: Adaptive inputs for the experiment with degradation of the third rotor without external disturbance.

Finally, it is interesting to analyze the time evolution of the parameter $\hat{\Lambda}$ in Figure 4.9 where the dotted lines represent the true parameter values after the fault occurrence, whereas the continuous lines correspond to their estimated values.

During the initial phase, when there are no actuator faults, $\hat{\Lambda}(t)$ exhibits only minor deviations from its nominal value (equal to 1 for the diagonal elements and 0 for the off-diagonal ones). After the fault occurrence, all estimates undergo a rapid adaptation process and converge toward new steady-state values. The estimation accuracy of the diagonal elements of $\hat{\Lambda}(t)$ can be considered quite accurate, in fact the true efficiency reduction is almost perfectly reconstructed. Also, the off-diagonal elements assume relatively small values after the fault compared to their true values. Considering that this experiment is conducted on a physical platform under real operating conditions, the obtained estimates of Λ can be regarded as sufficiently accurate, especially when accounting for the unavoidable presence of measurement noise, unmodeled dynamics, and external disturbances.

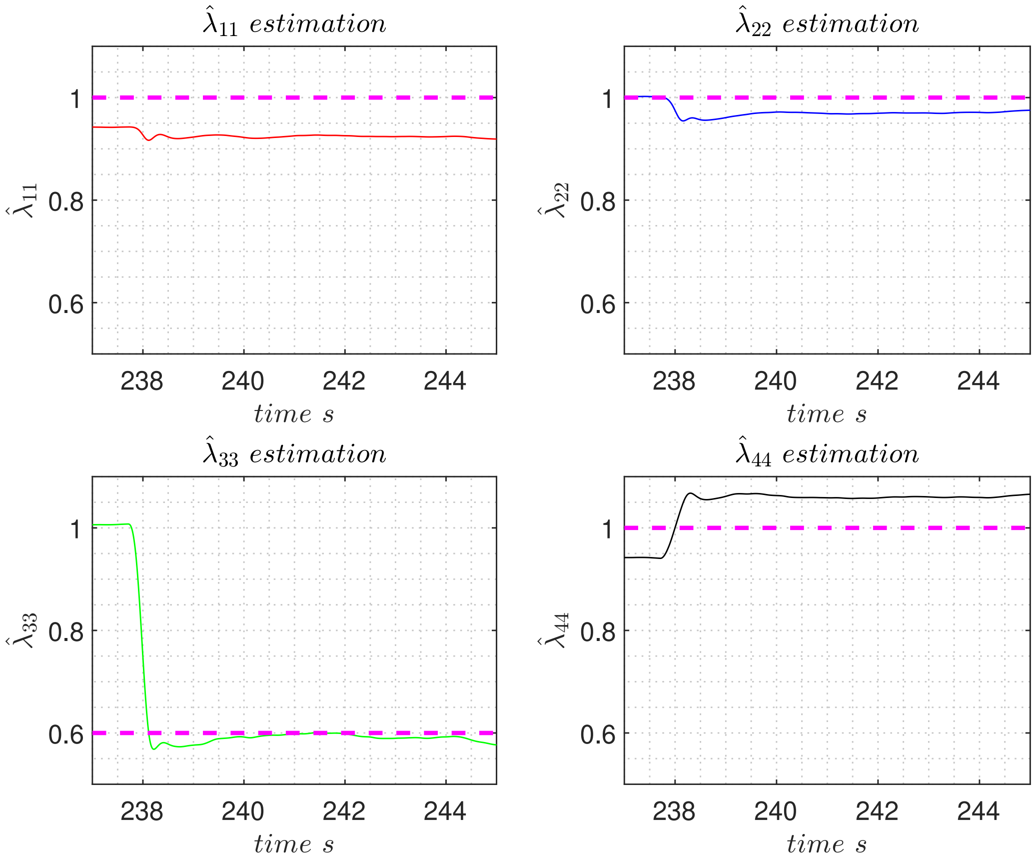

(a) Estimates of the diagonal terms of $\hat{\Lambda}(t)$.

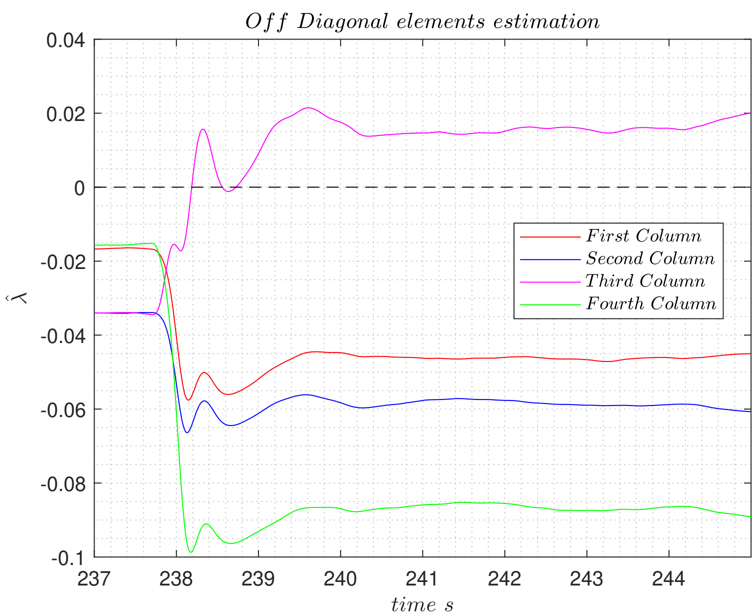

(b) Estimates of the off-diagonal terms of $\hat{\Lambda}(t)$.

Figure 4.9: Estimated effectiveness $\hat{\Lambda}$(t) for the experiment with degradation of the third rotor without external disturbance.

4.2. Hoovering condition with external wind disturbance and degradation of the third rotor

In the second test, an efficiency reduction of 20% is applied only to the third rotor (*i.e.*, $\lambda_3 = 0.8$), together with the presence of an external disturbance.

The external disturbance consists of a wind generated by a wind generator (WindShaper by WindShape) positioned at a distance between 3 m and 3.2 m from the hovering position of the drone. The wind is aligned as closely as possible with the body-frame y-axis of the drone and impacts the platform with an unknown velocity ranging between 3.6 and 4.8 m/s.
Since the exact magnitude of the wind disturbance is unknown, a quantitative comparison between the simulated and real scenarios is not feasible in this case. Therefore, only a comparison under identical experimental conditions between the adaptive controller and the baseline controller is performed.

First, the attitude angles, rates, velocity, and positions obtained with the adaptive and baseline controllers are compared.

From the attitude angle and angular rate responses in Figure 4.10 and in Figure 4.11, it can be observed that both controllers exhibit a similar oscillatory behavior, which is induced by the external wind disturbance. This oscillatory behavior is not present at the beginning of the experiment and appears only after the wind is applied, thus confirming that it is directly related to the external disturbance. It can be seen that to keep the hovering position, the drone reaches a roll angle of about -10 deg because of the presence of the constant lateral force disturbance produced by the windshaper.

The main difference between the adaptive and baseline controllers in terms of attitude angles and rates is that, after the fault, the oscillation amplitude is slightly larger in the baseline case, rather than the adaptive case, due to the absence of the additional adaptive control action.

More pronounced differences can be observed in the position and velocity responses in Figure 4.12 and in Figure 4.13. Although the overall trends are similar in the two cases, the magnitudes of the peaks are significantly different. By analyzing the position time histories, an initial peak caused by the external disturbance can be observed along the East direction and in altitude. In particular, the adaptive controller exhibits an altitude loss of approximately 4 cm and an East displacement of about 30 cm while, in contrast, the baseline controller exhibits an altitude loss of approximately 8 cm and an East displacement

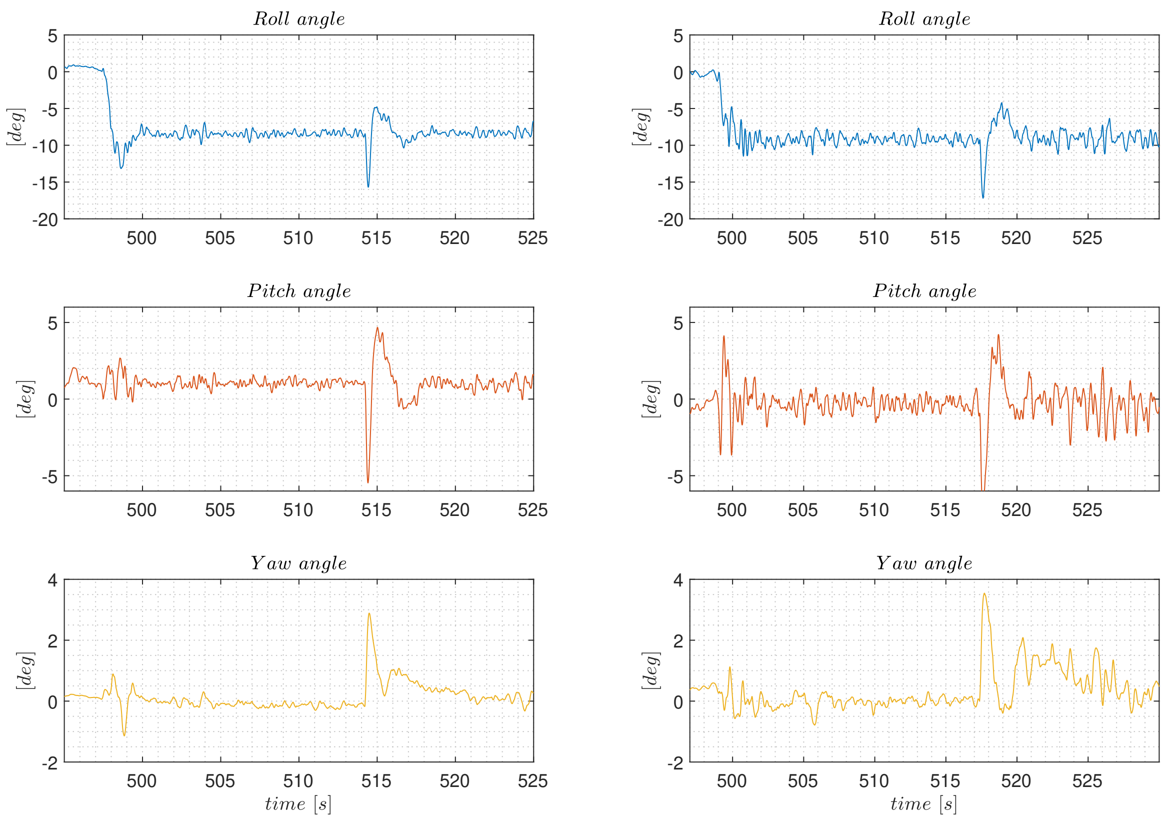

(a) Attitude Augmented.

(b) Attitude Baseline.

Figure 4.10: Roll, pitch and yaw angles for the experiment with external wind disturbance and degradation of the third rotor.

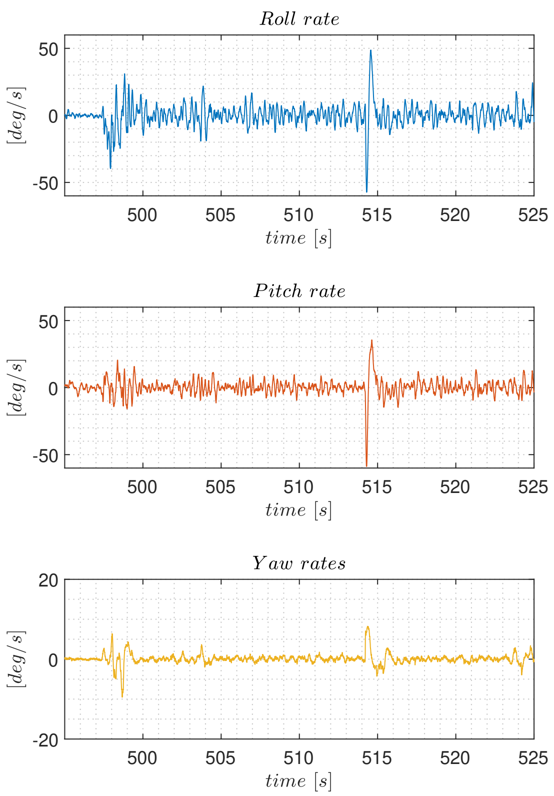

(a) Rates Augmented

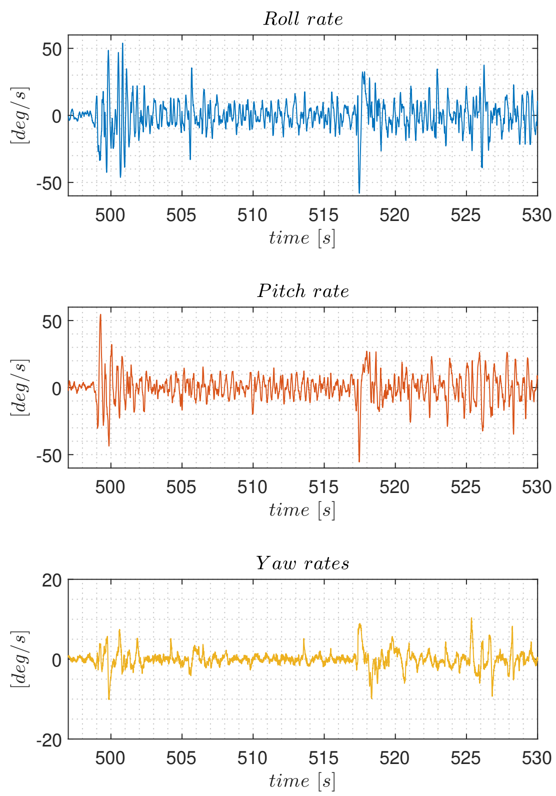

(b) Rates Baseline

Figure 4.11: Roll, pitch and yaw rates for the experiment with external wind disturbance and degradation of the third rotor.

of about 60 cm.

Subsequently, further peaks appear in all position components due to the rotor fault. By comparing the two versions, the adaptive controller exhibits an altitude loss of approximately 5 cm, an East displacement of about 15 cm, and a North displacement of about 15 cm. The baseline controller, instead, exhibits a larger altitude loss of about 10 cm, an East displacement of approximately 30 cm, and a North displacement of approximately 40 cm.

Similar considerations also apply to the velocity responses.

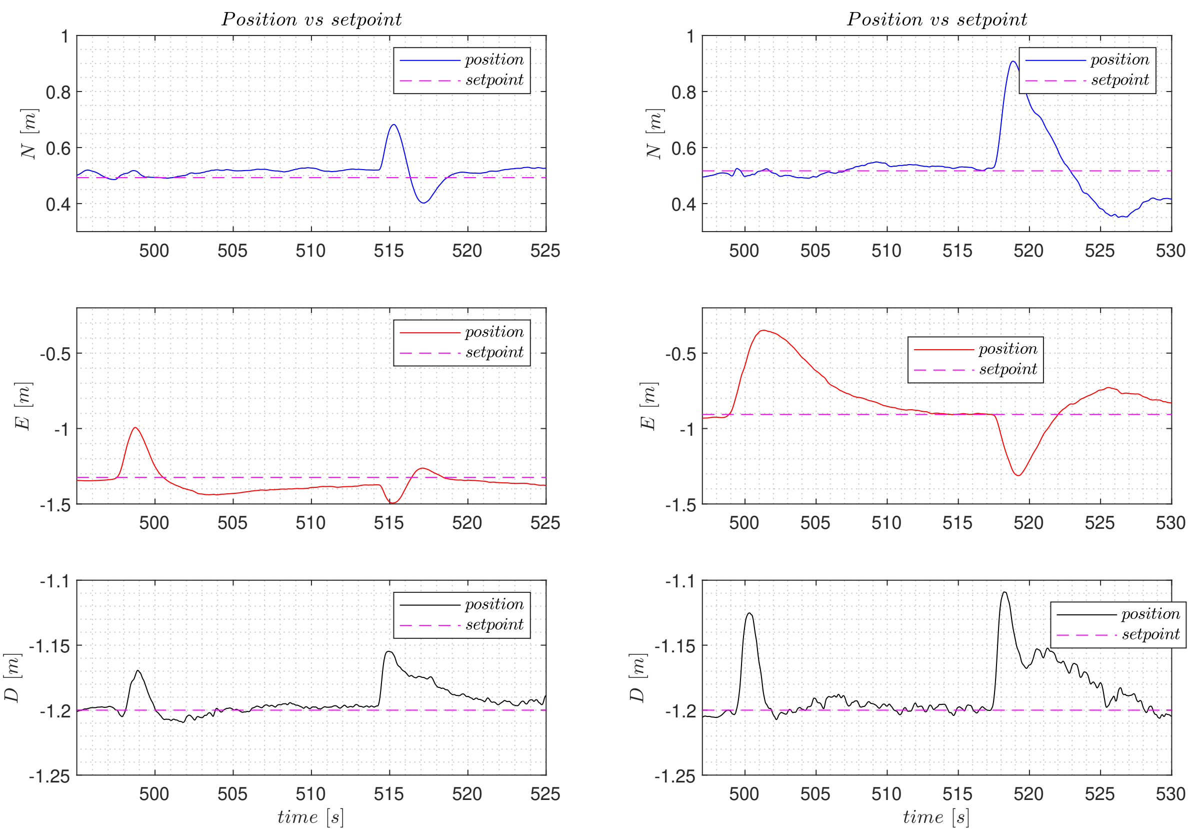

(a) Position Augmented

(b) Position Baseline

Figure 4.12: North, East, Down position for the experiment with external wind disturbance and degradation of the third rotor.

Overall, the adaptive controller demonstrates a clear performance improvement over the baseline controller, as evidenced by the significantly smaller spatial displacements observed under both external disturbances and actuator fault conditions. Moreover, the transient required to re-establish the hovering condition is approximately three times

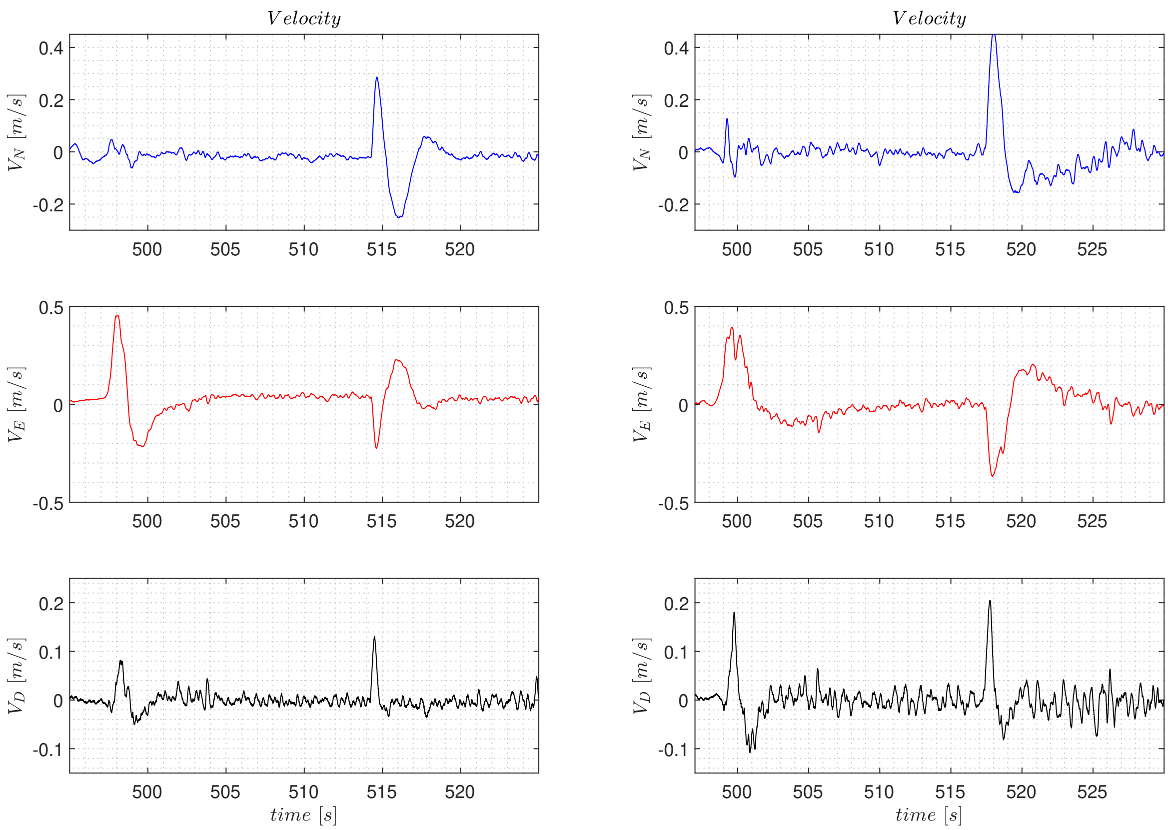

(a) Velocity Augmented

(b) Velocity Baseline

Figure 4.13: North, East, Down velocity for the experiment with external wind disturbance and degradation of the third rotor.

shorter when using the adaptive controller compared to the baseline controller.

The time evolution of the parameter $\hat{\theta}_d$ is analyzed in Figure 4.14. The parameter vector $\hat{\theta}_{d,\text{att}}$ does not exhibit significant changes in its mean values immediately after the application of the wind disturbance (at approximately $t = 498\,\text{s}$). This behavior is consistent with the fact that the wind is mainly aligned with the body-frame y-axis and therefore induces only limited moment imbalances. Approximately at $t = 514\,\text{s}$, a rapid variation in the magnitude of $\hat{\theta}_{d,\text{att}}$ is observed. This corresponds to the occurrence of the rotor fault, which introduces a moment imbalance that must be compensated by the adaptive controller.

Regarding $\hat{\theta}_{d,\text{pos}}$, no significant variation is observed in $\hat{\theta}_{d,1}$, a limited variation is present in $\hat{\theta}_{d,2}$, and a significant variation appears in $\hat{\theta}_{d,3}$ following the wind disturbance, consistently with the direction of the applied wind. After the rotor fault and the transient, an increase is observed primarily in the parameter associated with the z-velocity, as expected.

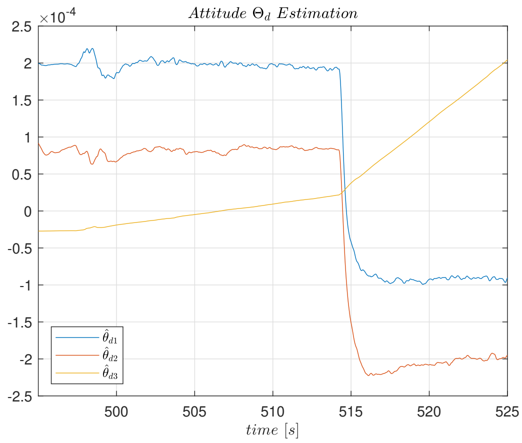

(a) $\hat{\theta}_{d_{att}}(t)$

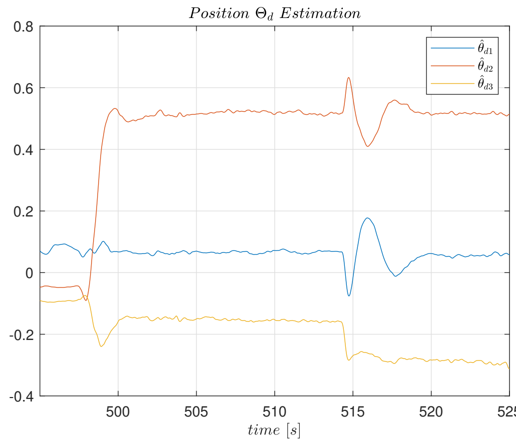

(b) $\hat{\theta}_{d_{pos}}(t)$

Figure 4.14: Estimated disturbances $\hat{\theta}_d(t)$ for the experiment with external wind disturbance and degradation of the third rotor.

Finally, the time evolution of the parameter $\hat{\Lambda}$ shown in Figure 4.15 is examined. In the figure, the dotted lines denote the true parameter values following the fault occurrence, while the solid lines represent the corresponding estimated values.

During the initial phase, when only disturbances are present and no actuator faults have occurred, the effectiveness estimate $\hat{\Lambda}(t)$ exhibits only minor deviations from its nominal value (equal to 1 for the diagonal elements and 0 for the off-diagonal elements). It can therefore be concluded that the estimate is largely unaffected by the presence of disturbances.

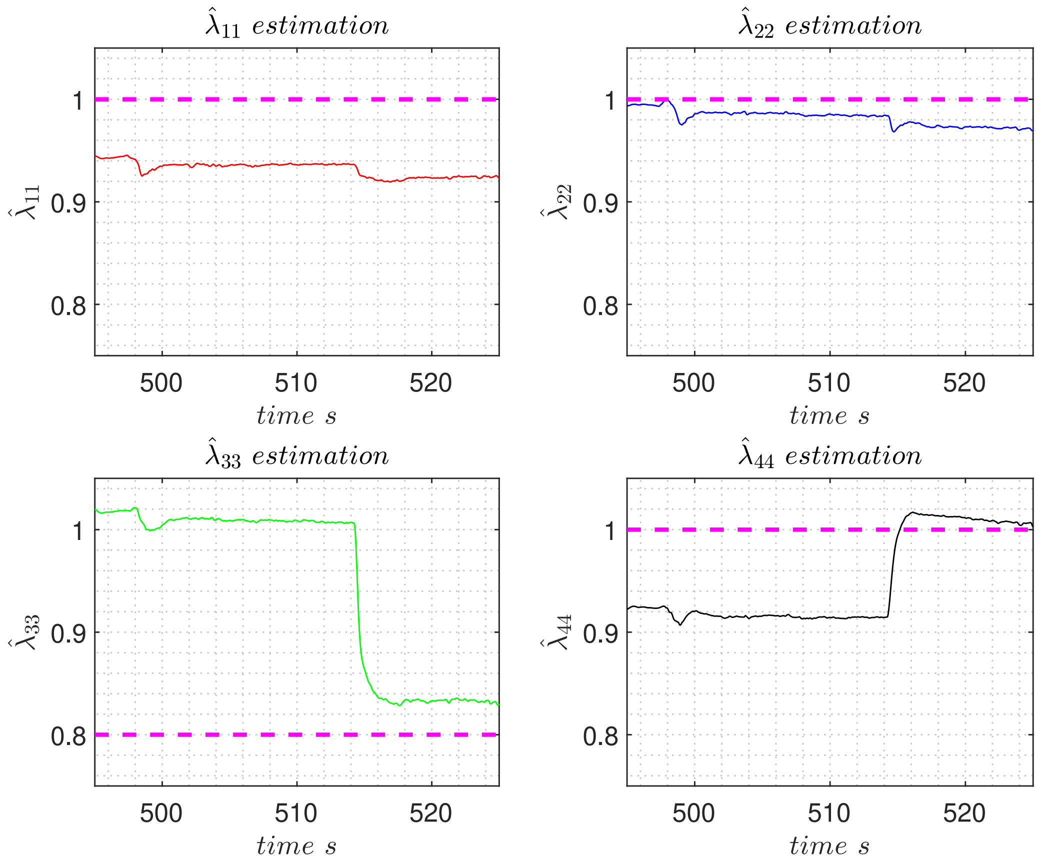

(a) Estimates of the diagonal terms of $\hat{\Lambda}(t)$

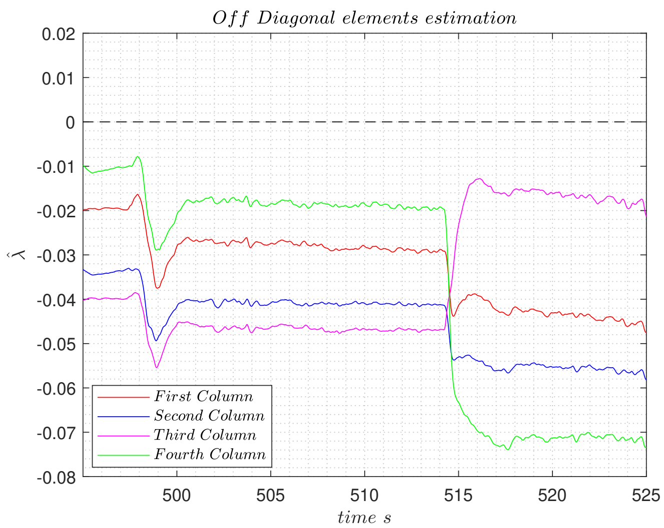

(b) Estimates of the off-diagonal terms of $\hat{\Lambda}(t)$

Figure 4.15: Estimated effectiveness $\hat{\Lambda}$(t) for the experiment with external wind disturbance and degradation of the third rotor.

Following the occurrence of the fault, all estimated parameters undergo a rapid adaptation process and converge toward new steady-state values. The estimation accuracy of the diagonal elements of $\hat{\Lambda}(t)$ can be considered high, as the true efficiency reduction is reconstructed almost exactly. The off-diagonal elements also converge to relatively small values after the fault, in line with their true magnitudes.

Considering that this experiment is conducted on a physical platform under real operating conditions, the obtained estimates of Λ can be regarded as sufficiently accurate, especially when accounting for the unavoidable presence of measurement noise, unmodeled dynamics, and external disturbances.

4.3. Hoovering condition with external wind disturbance and degradation of all rotors

In the third test, an efficiency reduction of 20% is applied to all rotors (*i.e.*, $\lambda_i = 0.8$), together with the presence of an external disturbance.

As in the previous test, the disturbance is generated by a wind generator (WindShaper by WindShape) placed at a distance between 3 and $3.2m$ from the hovering location of the drone. The wind is aligned as closely as possible along the body-frame y-axis and impacts the drone with an unknown velocity ranging between 4.8 and 6.4 m/s. As in the second test, since the exact wind magnitude is unknown, a quantitative comparison between simulation and real experiments is not possible. Therefore, only a qualitative comparison between the adaptive controller and the baseline controller under identical experimental conditions is carried out.

The performance impovement given by the adaptive augmentation can be observed in the position and velocity responses in Figure 4.12 and in Figure 4.13. Although the qualitative trends are similar, the magnitudes of the deviations are substantially different.

By analyzing the position time histories, an initial peak induced by the wind disturbance can be observed in all the directions. In particular, the adaptive controller exhibits an altitude loss of approximately 5 cm and an East displacement of about 43 cm, whereas the baseline controller exhibits an altitude loss of approximately 7 cm and an East displacement of about 72 cm. Subsequently, another peak in altitude is observed due to the actuator fault. The adaptive controller exhibits an altitude loss of approximately 11 cm, whereas the baseline controller exhibits a much larger altitude loss of approximately 30 cm.

Similar trends are observed in the velocity responses.

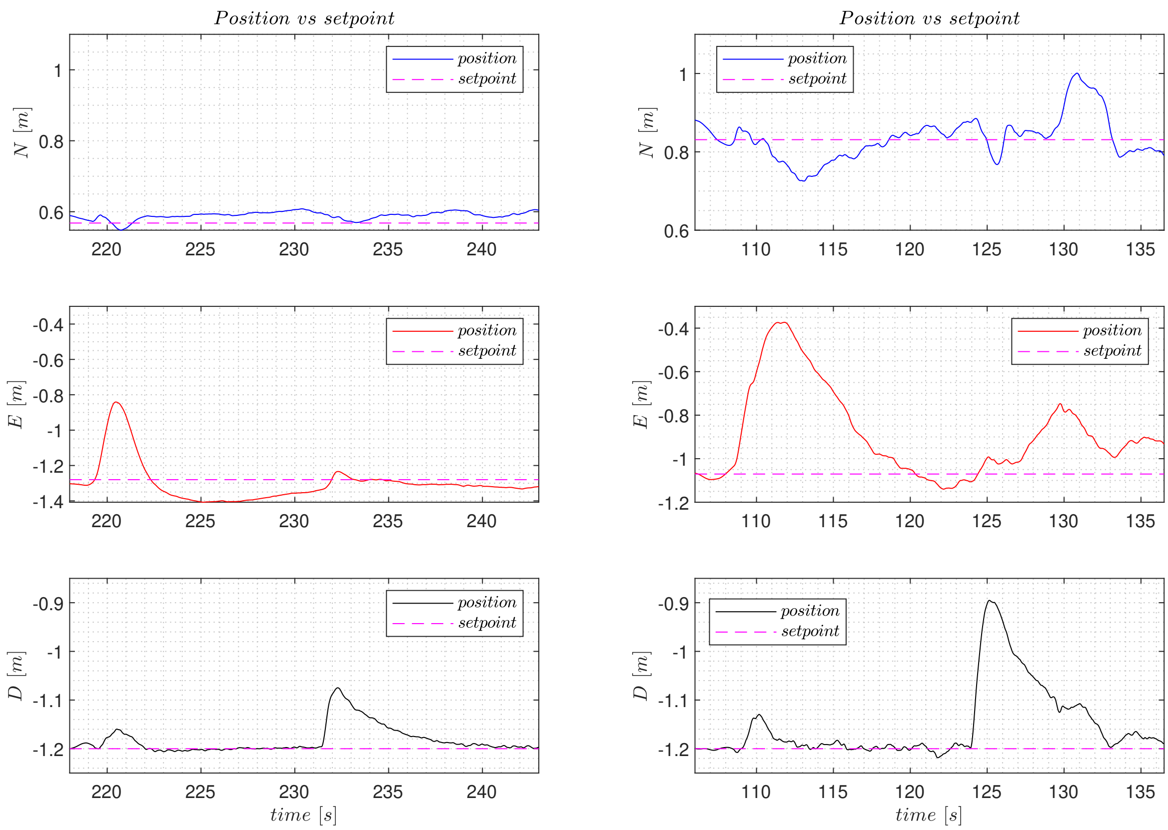

(a) Position Augmented (b) Position Baseline

Figure 4.16: North, East, Down Position for the experiment with external wind disturbance and degradation of all rotors.

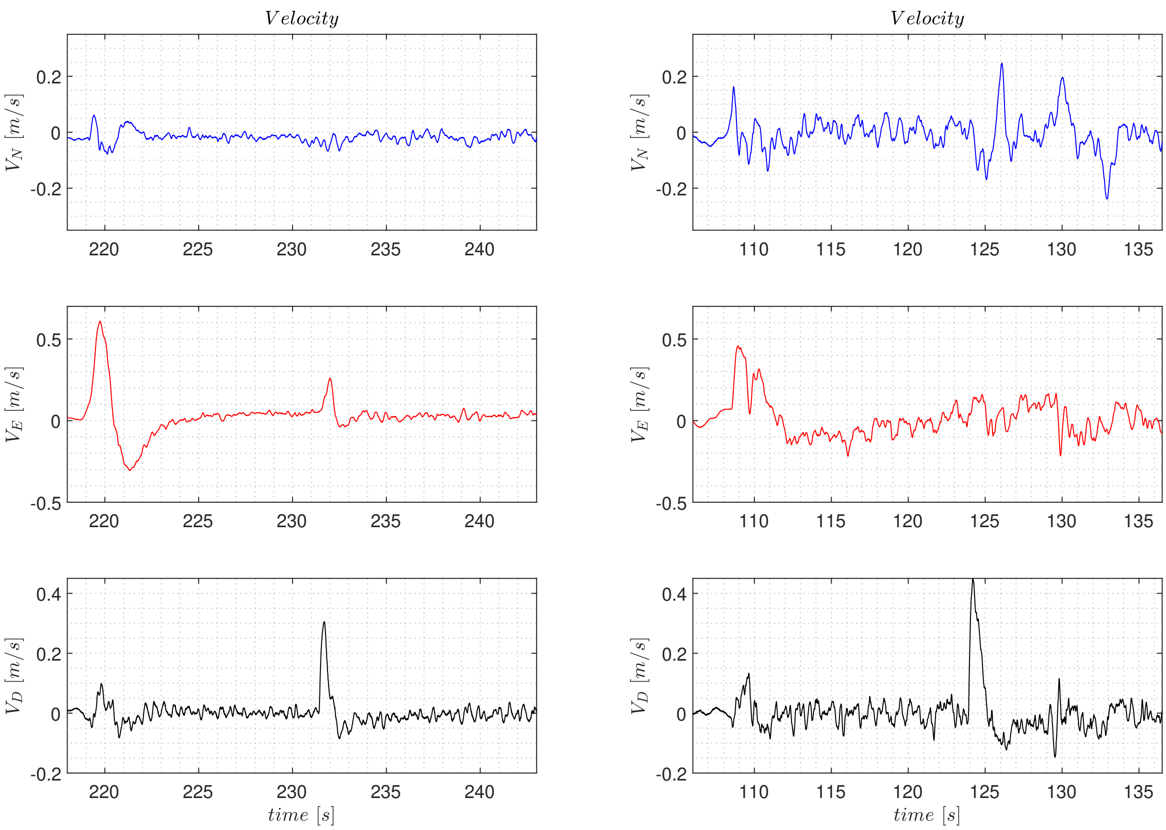

(a) Velocity Augmented

(b) Velocity Baseline

Figure 4.17: North, East, Down Position for the experiment with external wind disturbance and degradation of all rotors.

Overall, the adaptive controller clearly outperforms the baseline controller, providing significantly smaller spatial displacements and a more contained oscillatory behavior along all directions under the combined effect of wind and actuator faults. Moreover, the transient required to restore the hovering condition is approximately three times faster with the adaptive controller than with the baseline controller.

The time evolution of the parameter $\hat{\theta}_d$ is analyzed in Figure 4.18. The behavior of $\hat{\theta}_d$

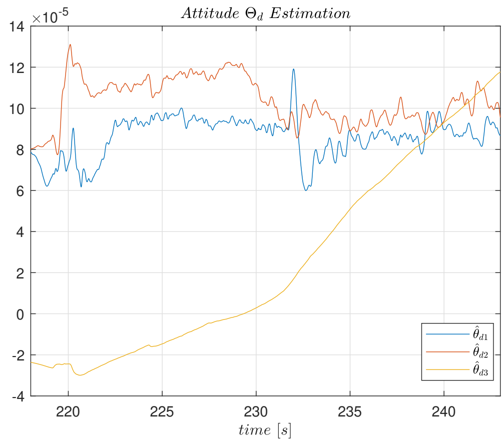

(a) $\hat{\theta}_{d_{att}}(t)$

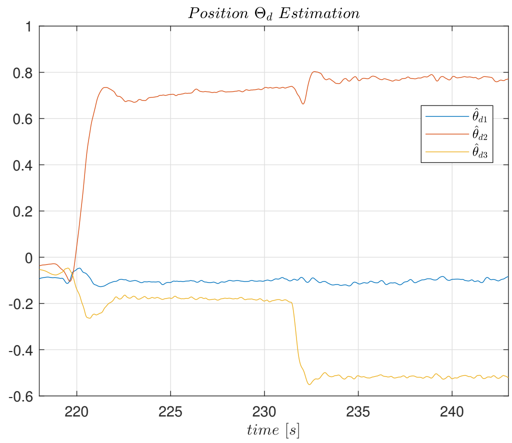

(b) $\hat{\theta}_{d_{pos}}(t)$

Figure 4.18: Estimated disturbance $\hat{\theta}_d(t)$ for the experiment with external wind disturbance and degradation of all rotors.

is consistent with the one analyzed in the previous test. However, because the efficiency reduction affects all rotors symmetrically, no appreciable increase in the magnitude of $\hat{\theta}_{d,\text{att}}$ is detected.

Finally, it is interesting to analyze the time evolution of the parameter $\hat{\Lambda}$ by looking at Figure 4.19. As in the previous case, the dotted lines represent the true parameter values after the fault occurrence, whereas the continuous lines correspond to their estimated values.

During the initial phase, when only external disturbances are present and no actuator faults have occurred, the effectiveness estimate $\hat{\Lambda}(t)$ exhibits only minor deviations from its nominal value (equal to 1 for the diagonal elements and 0 for the off-diagonal elements). It can therefore be concluded that this estimate is largely unaffected by the disturbances.

Following the occurrence of the fault, all estimates undergo a rapid adaptation process and converge toward new steady-state values. The estimation accuracy of the diagonal elements of $\hat{\Lambda}(t)$ can be considered satisfactory, as the efficiency reduction is reconstructed

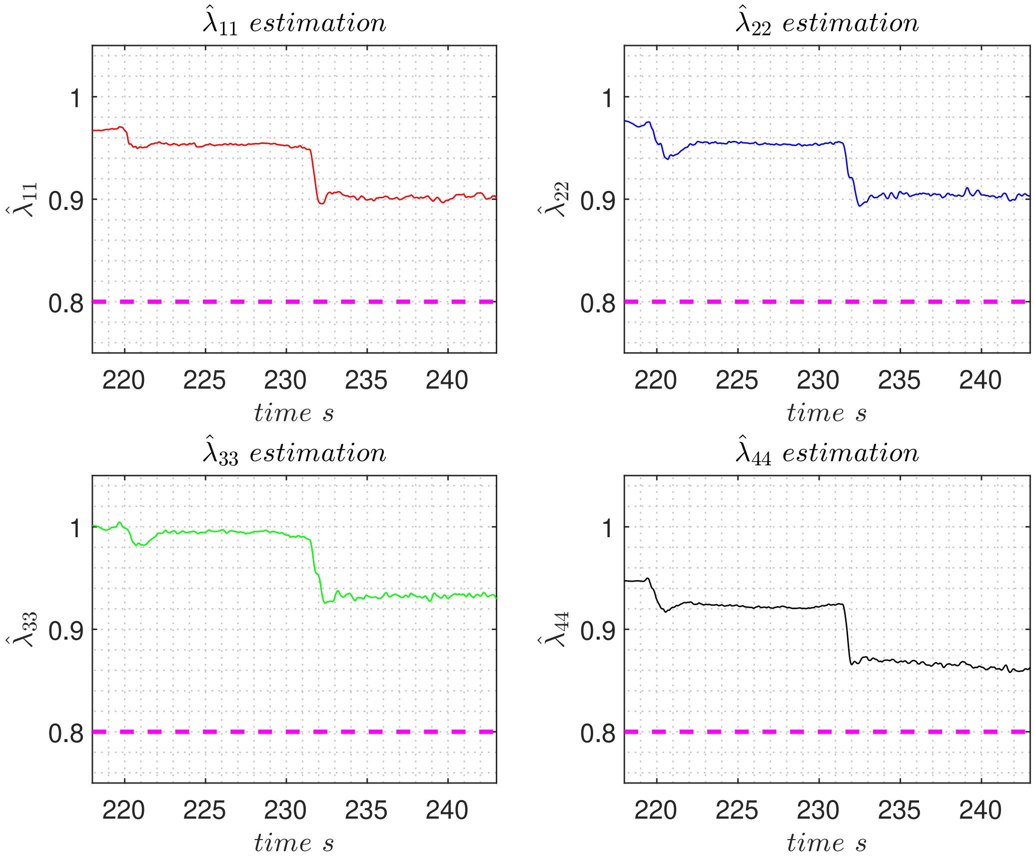

(a) Estimates of the diagonal terms of $\hat{\Lambda}(t)$.

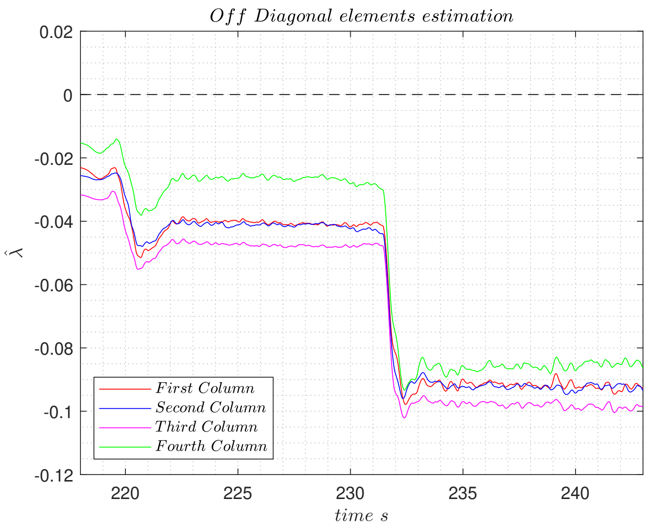

(b) Estimates of the off-diagonal terms of $\hat{\Lambda}(t)$.

Figure 4.19: Estimated effectiveness $\hat{\Lambda}$(t) for the experiment with external wind disturbance and degradation of all rotors.

with good accuracy. The off-diagonal elements also converge to relatively small values after the fault, consistent with their true magnitudes.

As can be observed, the overall estimation accuracy is poorer than in the case where the fault affects only the third rotor. This difference is attributable to the nature of the fault. In particular, a uniform efficiency reduction across all rotors can be effectively compensated for, and equivalently modeled as, a constant disturbance acting along the vertical axis.

This interpretation is further supported by the estimated external disturbance terms. By comparing the vertical disturbance estimates in Figure 4.18b and Figure 4.14b, it can be observed that the vertical component is larger in the former case. This indicates that the efficiency degradation is primarily compensated through the estimation of an equivalent external force acting in the vertical direction.

Considering that this experiment is conducted on a physical platform under real operating conditions, the obtained estimates of Λ can be regarded as sufficiently accurate, especially when accounting for the unavoidable presence of measurement noise, unmodeled dynamics, and the external disturbances.

5 | Conclusions and future developments

The analyses carried out throughout this thesis clearly demonstrate the effectiveness and advantages of applying an Augmented P-MRAC adaptive controller to a vector-thrust quadrotor UAV.

In the first chapter, the theoretical framework of the Augmented P-MRAC controller was developed for a generic uncertain dynamical system. Particular emphasis was placed on the exploitation of overactuation through Singular Value Decomposition (SVD) and on the structural properties of the control effectiveness matrix Λ, enabling a reduction in the number of adaptive parameters while preserving stability guarantees.

In the second chapter, the adaptive framework was specialized to the case of a vector-thrust quadrotor UAV. The structural characteristics of the platform were leveraged to reduce computational complexity and to ensure real-time implementability. Two alternative controller architectures were formulated, highlighting the trade-off between modularity, parameter reduction, and direct actuator efficiency estimation.

In the third chapter, numerical simulations were performed in a Simulink environment under different actuator fault scenarios and external disturbances. The results consistently showed a significant improvement in tracking performance and robustness when the adaptive augmentation was enabled.

Finally, real-world experimental validation was conducted by implementing the separated Augmented P-MRAC architecture on a physical vector-thrust quadrotor UAV (ANT-X platform). The experimental results, supported by comparisons with both baseline and simulation outcomes, confirmed the practical effectiveness of the proposed approach. In particular, the adaptive controller demonstrated enhanced robustness to actuator efficiency losses and wind disturbances, while maintaining stable flight and satisfactory tracking performance under real operating conditions.

Possible future developments include the extension of the proposed Augmented P-MRAC framework to fully overactuated systems, rather than limiting the approach to overactuated subsystems. Such an extension would allow a more comprehensive exploitation of actuation redundancy, further enhancing adaptive control allocation capabilities in the presence of partial or total actuator faults and under more severe disturbance conditions. Additionally, further research could investigate improved parameter adaptation mechanisms to enhance identifiability and robustness in highly dynamic flight scenarios.s.

Bibliography

[1] I. Amazon.com, "Amazon prime air," 2013.

[2] I. Amazon.com, "Amazon prime air drone mk30," 2022.

[3] Hexoplus, "Hexoplus drone," 2014.

[4] H. J. Umair B. Chaudhry, *Autonomous Revolution: Strategies, Threats and Challenges*, vol. 1 of *1*. |: Springer, Cham, 1 ed., 7 2025.

[5] UM, "Um's schools of medicine and engineering first to use unmanned aircraft to deliver kidney for transplant at ummc," 2019.

[6] CityAirbus, "Cityairbus nextgen," 2024.

[7] W. A. by Boeing, "Wisk aero," 2022.

[8] J. S. Eterno, J. L. Weiss, D. P. Looze, and A. Willsky in *1985 24th IEEE Conference on Decision and Control*, 1985 24th IEEE Conference on Decision and Control, 1985.

[9] E. Lavretsky and K. A. Wise, *Robust and Adaptive Control with Aerospace Applications*. Springer-Verlag, 2013.

[10] A. Aran, H. Ghaffarzadeh, D. Miller, and N. Talebian, "Robust controller analysis and synthesis with consideration of various uncertainties for building structures," *Engineering Structures*, 2024.

[11] Y. Zhang and J. Jiang, "Bibliographical review on reconfigurable fault-tolerant control systems," *Annual Reviews in Control*, vol. 32, pp. 229–252, 2008.

[12] G. Dumont and M. Huzmezan, "Concepts, methods and techniques in adaptive control," in *Proceedings of the 2002 American Control Conference (IEEE Cat. No.CH37301)*, 2002.

[13] A. Shekhar and A. Sharma, "Review of model reference adaptive control," in *2018 International Conference on Information , Communication, Engineering and Technology (ICICET)*, 2018.

[14] G. P. F. Salazar, *Adaptive Fault Tolerant Control for VTOL Aircraft with Actuator Redundancy.* PhD thesis, Technical University of Munich, Technical University of Munich, Arcisstrasse 2180333 Munichr, 2022.

[15] C.-C. HANG and P. C. PARKS, "Comparative studies of model reference adaptive control systems," 1973.

[16] D. Invernizzi and A. Serrani, "Predictor-based adaptive plant augmentation design with application to hierarchical control," *IEEE CONTROL SYSTEMS LETTERS*, vol. 8, pp. 502–507, 2024.

[17] E. Lavretsky, R. Gadient, and I. M. Gregory, "Predictor-based model reference adaptive control," tech. rep., The Boeing Company and NASA Langley Research Center, Huntington Beach, CA 92647, USA and Hampton, VA 23681-2199, USA.

[18] K. A.Bordignon and W. C. Durham, "Null space augmented solutions to constrained control allocation problems," *American Institute of Aeronautics and Astronautics*, pp. 328–333.

[19] M. Bodson, "Evaluation of optimization methods for control allocation," *Journal of Guidance Control and Dynamics - J GUID CONTROL DYNAM*, 2002.

[20] A. Leonessa, W. M. Haddad, T. Hayakawa, and Y. Morel, "Adaptive control for nonlinear uncertain systems with actuator amplitude and rate saturation constraints," *International Journal of Adaptive Control and Signal Processing*, 2009.

[21] G. P. Falconì, C. D. Heise, and F. Holzapfel, "Novel control law for predictor-based mrac for overactuated systems," 14th International Conference on Control, Automation, Robotics & Vision Phuket, Thailand, 13-15th November, 2016.

[22] G. P. Falconì, C. D. Heise, and F. Holzapfel, "Novel stability analysis of direct mrac with redundant inputs," 24th Mediterranean Conference on Control and Automation (MED), June 21-24, 2016, Athens, Greece, 2016.

[23] M. Manzoni, R. Rubinacci, G. Gozzini, and D. Invernizzi, "Control-oriented modeling and hierarchical control of multirotor UAVs for research and teaching purposes," 2024. 2nd IFAC Workshop on Aerospace Control Education - WACE 2024.

[24] D. Invernizzi, *Adaptive And Autonomous Aerospace Systems Course.* Politecnico Di Milano, 2023.

[25] S. Meraglia, G. Gozzini, S. Liu, and D. Invernizzi, "Adaptive control for high-

performance trajectory tracking in multirotor uavs," in *2023 9th International Conference on Control, Decision and Information Technologies (CoDIT)*, 2023.

[26] ANT-X, "Ant-x drone lab," 2025.

A | Theorems

In this appendix, the mathematical tools that are used in the Thesis, but not explained, are presented:

Theorem A.1. ***Trace and Scalar product:*** *for any 2 vectors $a, b \in \mathbb{R}^n$, it holds that:*

$$a^\top b = \mathrm{trace}(ba^\top) \tag{A.1}$$

Proof: due to the fact that a, b are 2 vectors, $ba^\top$ has rank 1. If we then recall the trace function:

$$\mathrm{trace}(ba^\top) = \sum_{i=1}^{n} (ba^\top)_{ii} = \sum_{i=1}^{n} b_i a_i \tag{A.2}$$

but:

$$a^\top b = \sum_{i=1}^{n} a_i b_i \tag{A.3}$$

so:

$$\mathrm{trace}(ba^\top) = \sum_{i=1}^{n} b_i a_i = \sum_{i=1}^{n} a_i b_i = a^\top b! \tag{A.4}$$

Theorem A.2. ***LU inversion:*** *Given $A \in \mathbb{R}^{n \times n}$ an invertible matrix, its inverse can be computed by using LU decomposition.*
A method to compute the inverse of a $n \times n$ matrix A, is to solve the matrix equation:

$$AX = I_{n \times n} \tag{A.5}$$

The previous equation can be rewritten in columns as a system of equations:

$$Ax_j = e_j \qquad j = 1, ..., n \tag{A.6}$$

in which e_j is the j-th column of I and x_j is the j-th column of X.

If we apply a LU decomposition on A, we obtain:

$$A = LU \tag{A.7}$$

*in which $L \in \mathbb{R}^{n\times n}$ is a lower triangular matrix and $U \in \mathbb{R}^{n\times n}$ is an upper triangular matrix (**OBS**: Since only the right-hand side is different in each of the previous system of equations, the LU decomposition of A is needed only once).*
Given the LU decomposition, $A^{-1} = X$ is computed by solving, for $j = 1, ..., n$, the systems:

$$\begin{aligned} Ly_j &= e_j \\ Ux_j &= y_j \end{aligned} \tag{A.8}$$

with forward substitution method and backward substitution method respectively, knowing that the generic x_j is the j-th column of the inverse A^{-1}.

Theorem A.3. ***Sherman-Morrison theorem:*** *Given $A \in \mathbb{R}^{n\times n}$ an invertible matrix, given $D \in \mathbb{R}^{n\times n}$ an invertible matrix and $r, v \in \mathbb{R}^n$ two generic vectors, such that $A = D + rv^\top$.*
If $1 + v^\top D^{-1} r \neq 0$, it can be observed that:

$$A^{-1} = (D + rv^\top)^{-1} = D^{-1} - \frac{D^{-1}rv^\top D^{-1}}{1 + v^\top D^{-1} r} \tag{A.9}$$

Proof: Given $(D + rv^\top)$, we need to find a matrix B, such that:

$$(D + rv^\top) \cdot B = I_{n\times n} \tag{A.10}$$

Consider:

$$B = D^{-1} - \frac{D^{-1}rv^\top D^{-1}}{1 + v^\top D^{-1} r} \tag{A.11}$$

if we multiply B on the left by $(D + rv^\top)$, we obtain:

$$(D + rv^\top) \cdot B = DB + rv^\top B = DD^{-1} - \frac{DD^{-1}rv^\top D^{-1}}{1 + v^\top D^{-1} r} + rv^\top D^{-1} - \frac{rv^\top D^{-1} rv^\top D^{-1}}{1 + v^\top D^{-1} r} \tag{A.12}$$

If we observe that $v^\top D^{-1} r$ is a scalar, we obtain:

$$(D + rv^\top) \cdot B = I - \frac{rv^\top D^{-1}}{1 + v^\top D^{-1} r} + rv^\top D^{-1} - \frac{(v^\top D^{-1} r) rv^\top D^{-1}}{1 + v^\top D^{-1} r} \tag{A.13}$$

If we collect the term $(rv^\top D^{-1})$, we obtain:

$$(D + rv^\top) \cdot B = I + (rv^\top D^{-1}) \cdot \left(1 - \frac{1 + v^\top D^{-1} r}{1 + v^\top D^{-1} r}\right) \tag{A.14}$$

due to the fact that the right term between brackets is equal to zero:

$$(D + rv^\top) \cdot B = I! \tag{A.15}$$

Theorem A.4. ***Inverse of a diagonal matrix:*** *Given $A \in \mathbb{R}^{n \times n}$ a diagonal matrix, that has this form:*

$$A = \begin{bmatrix} a_1 & 0 & \cdots & 0 \\ 0 & a_2 & \cdots & 0 \\ \vdots & \vdots & \ddots & \vdots \\ 0 & 0 & \cdots & a_n \end{bmatrix} \tag{A.16}$$

Its inverse has always this form:

$$A^{-1} = \begin{bmatrix} \frac{1}{a_1} & 0 & \cdots & 0 \\ 0 & \frac{1}{a_2} & \cdots & 0 \\ \vdots & \vdots & \ddots & \vdots \\ 0 & 0 & \cdots & \frac{1}{a_n} \end{bmatrix} \tag{A.17}$$

Proof: given a generic matrix $D \in \mathbb{R}^{n \times n}$ and assuming that its inverse $D^{-1} \in \mathbb{R}^{n \times n}$ exist, D^{-1} is such that:

$$D \cdot D^{-1} = D^{-1} \cdot D = I_{n \times n} \tag{A.18}$$

If we apply this equations to the previous matrices:

$$A \cdot A^{-1} = A^{-1} \cdot A = \begin{bmatrix} \frac{1}{a_1} & 0 & \cdots & 0 \\ 0 & \frac{1}{a_2} & \cdots & 0 \\ \vdots & \vdots & \ddots & \vdots \\ 0 & 0 & \cdots & \frac{1}{a_n} \end{bmatrix} \cdot \begin{bmatrix} a_1 & 0 & \cdots & 0 \\ 0 & a_2 & \cdots & 0 \\ \vdots & \vdots & \ddots & \vdots \\ 0 & 0 & \cdots & a_n \end{bmatrix} = \begin{bmatrix} \frac{a_1}{a_1} & 0 & \cdots & 0 \\ 0 & \frac{a_2}{a_2} & \cdots & 0 \\ \vdots & \vdots & \ddots & \vdots \\ 0 & 0 & \cdots & \frac{a_n}{a_n} \end{bmatrix} = \begin{bmatrix} 1 & 0 & \cdots & 0 \\ 0 & 1 & \cdots & 0 \\ \vdots & \vdots & \ddots & \vdots \\ 0 & 0 & \cdots & 1 \end{bmatrix} = I_{n \times n}! \tag{A.19}$$

Theorem A.5. ***Raw components norm equality.*** *Consider a vector-thrust quadrotor*

UAV, and, in particular, its attitude dynamics input map:

$$W_M = \begin{bmatrix} -bs(\gamma_1) & -bs(\gamma_2) & -bs(\gamma_3) & -bs(\gamma_4) \\ bc(\gamma_1) & bc(\gamma_2) & bc(\gamma_3) & bc(\gamma_4) \\ -\xi_1\sigma & -\xi_2\sigma & -\xi_3\sigma & -\xi_4\sigma \end{bmatrix}. \tag{A.20}$$

If the quadrotor is in an X configuration with arms oriented at 45°, then, after applying a Singular Value Decomposition (SVD) to W_M, the reduced right-singular matrix V_{Mr} satisfies

$$\left|V_{Mr}(i,1)\right| = \left|V_{Mr}(i,2)\right| = \left|V_{Mr}(i,3)\right|, \quad \forall i = 1,\dots,4. \tag{A.21}$$

Proof: For a quadrotor with X configuration and arms oriented at 45°, the rotor angles and spin directions are given by

$$\begin{aligned} &\gamma_1 = \frac{\pi}{4}, \quad \gamma_2 = \frac{5\pi}{4}, \quad \gamma_3 = \frac{7\pi}{4}, \quad \gamma_4 = \frac{3\pi}{4}, \\ &\xi_i = (-1,-1,+1,+1). \end{aligned} \tag{A.22}$$

Substituting these values into W_M yields

$$W_M = \begin{bmatrix} -\frac{\sqrt{2}}{2}b & \frac{\sqrt{2}}{2}b & \frac{\sqrt{2}}{2}b & -\frac{\sqrt{2}}{2}b \\ \frac{\sqrt{2}}{2}b & -\frac{\sqrt{2}}{2}b & \frac{\sqrt{2}}{2}b & -\frac{\sqrt{2}}{2}b \\ \sigma & \sigma & -\sigma & -\sigma \end{bmatrix}. \tag{A.23}$$

Applying the Singular Value Decomposition $W_M = U_M \Sigma_M V_M^\top$ gives

$$\begin{aligned} U_M &= \begin{bmatrix} 1 & 0 & 0 \\ 0 & 1 & 0 \\ 0 & 0 & 1 \end{bmatrix}, \\ \Sigma_M &= \begin{bmatrix} \sqrt{2}\,|b| & 0 & 0 & 0 \\ 0 & \sqrt{2}\,|b| & 0 & 0 \\ 0 & 0 & 2|\sigma| & 0 \end{bmatrix}, \\ V_M &= \begin{bmatrix} -\frac{\mathrm{sgn}(b)}{2} & -\frac{\mathrm{sgn}(b)}{2} & \frac{\mathrm{sgn}(\sigma)}{2} & \frac{1}{2} \\ \frac{\mathrm{sgn}(b)}{2} & \frac{\mathrm{sgn}(b)}{2} & \frac{\mathrm{sgn}(\sigma)}{2} & \frac{1}{2} \\ -\frac{\mathrm{sgn}(b)}{2} & \frac{\mathrm{sgn}(b)}{2} & -\frac{\mathrm{sgn}(\sigma)}{2} & \frac{1}{2} \\ \frac{\mathrm{sgn}(b)}{2} & -\frac{\mathrm{sgn}(b)}{2} & -\frac{\mathrm{sgn}(\sigma)}{2} & \frac{1}{2} \end{bmatrix}. \end{aligned} \tag{A.24}$$

Assuming $b > 0$ and $\sigma > 0$, V_M simplifies to

$$V_M = \begin{bmatrix} -\frac{1}{2} & -\frac{1}{2} & \frac{1}{2} & \frac{1}{2} \\ \frac{1}{2} & \frac{1}{2} & \frac{1}{2} & \frac{1}{2} \\ -\frac{1}{2} & \frac{1}{2} & -\frac{1}{2} & \frac{1}{2} \\ \frac{1}{2} & -\frac{1}{2} & -\frac{1}{2} & \frac{1}{2} \end{bmatrix}. \tag{A.25}$$

Recalling the definition of the reduced right-singular matrix V_{Mr} (cf. Section 1.2.2), one obtains

$$V_{Mr} = \begin{bmatrix} -\frac{1}{2} & -\frac{1}{2} & \frac{1}{2} \\ \frac{1}{2} & \frac{1}{2} & \frac{1}{2} \\ -\frac{1}{2} & \frac{1}{2} & -\frac{1}{2} \\ \frac{1}{2} & -\frac{1}{2} & -\frac{1}{2} \end{bmatrix}. \tag{A.26}$$

Hence, each row of V_{Mr} has components with equal absolute value, and condition (A.21) *is satisfied.*

Theorem A.6. *Given the reduced right-singular matrix V_{Mr} obtained for the X-configuration quadrotor, the matrix B_Λ is invertible.*
Proof: Consider the reduced right-singular matrix V_{Mr} computed in the previous section:

$$V_{Mr} = \begin{bmatrix} -\frac{1}{2} & -\frac{1}{2} & \frac{1}{2} \\ \frac{1}{2} & \frac{1}{2} & \frac{1}{2} \\ -\frac{1}{2} & \frac{1}{2} & -\frac{1}{2} \\ \frac{1}{2} & -\frac{1}{2} & -\frac{1}{2} \end{bmatrix}. \tag{A.27}$$

The matrix B_Λ, defined as

$$B_\Lambda = \begin{bmatrix} V_{Mr_{11}}^2 & V_{Mr_{21}}^2 & V_{Mr_{31}}^2 & V_{Mr_{41}}^2 \\ V_{Mr_{11}}V_{Mr_{12}} & V_{Mr_{21}}V_{Mr_{22}} & V_{Mr_{31}}V_{Mr_{32}} & V_{Mr_{41}}V_{Mr_{42}} \\ V_{Mr_{11}}V_{Mr_{13}} & V_{Mr_{21}}V_{Mr_{23}} & V_{Mr_{31}}V_{Mr_{33}} & V_{Mr_{41}}V_{Mr_{43}} \\ V_{Mr_{12}}V_{Mr_{13}} & V_{Mr_{22}}V_{Mr_{23}} & V_{Mr_{32}}V_{Mr_{33}} & V_{Mr_{42}}V_{Mr_{43}} \end{bmatrix}, \tag{A.28}$$

assumes the following explicit form:

$$B_\Lambda = \frac{1}{4}\begin{pmatrix} 1 & 1 & 1 & 1 \\ 1 & 1 & -1 & -1 \\ -1 & 1 & 1 & -1 \\ -1 & 1 & -1 & 1 \end{pmatrix}. \tag{A.29}$$

The determinant of B_Λ is

$$\det(B_\Lambda) = \frac{1}{16} \neq 0, \tag{A.30}$$

which proves that B_Λ is invertible.

List of Figures

1 MRAC structure. . . . 3
2 Augmented P-MRAC. . . . 4

1.1 Augmented P-MRAC structure. . . . 14

2.1 Vector-thrust UAVs scheme. . . . 19

3.1 Augmented P-MRAC on the vector-thrust quadrotor UAV. . . . 37
3.2 Controller block of the vector-thrust quadrotor UAV. . . . 38
3.3 Exemple of external distrubance. . . . 39
3.4 Angular rates for the position setpoint simulation in the decoupled case. . 40
3.5 Velocity for the position setpoint simulation in the decoupled case. . . . 41
3.6 Position for the position setpoint simulation in the decoupled case. . . . 42
3.7 States estimation errors for the position setpoint simulation in the decoupled case. . . . 43
3.8 Propellers' thrust for the position setpoint simulation in the decoupled case. 43
3.9 Parameter estimates $\hat{\theta}_{d,att}$ and $\hat{\theta}_{d,pos}$ for the position setpoint simulation in the decoupled case. . . . 45
3.10 Diagonal terms of $\hat{\Lambda}(t)$ for the position setpoint simulation in the decoupled case. . . . 46
3.11 Estimates $\hat{\Lambda}$ of the off-diagonal terms of the effectivenss matrix for the position setpoint simulation in the decoupled case. . . . 46
3.12 Angular rates for the position setpoint simulation in the coupled case. . . 47
3.13 Velocity for the position setpoint simulation in the coupled case. . . . 48
3.14 Position for the position setpoint simulation in the coupled case. . . . 49
3.15 Estimated states for the position setpoint simulation in the coupled case. . 49
3.16 Estimate of the position and attitude disturbance $\hat{\theta}_d$ for the position setpoint simulation in the coupled case. . . . 50
3.17 Estimate of the effectiveness $\hat{\Lambda}(t)$ for the position setpoint simulation in the coupled case. . . . 51
3.18 Angular rates for the circular setpoint simulation in the decoupled case. . 53

3.19 Velocity for the circular setpoint simulation in the decoupled case. 54
3.20 Position for the circular setpoint simulation in the decoupled case. 54
3.21 State estimation error for the circular setpoint simulation in the decoupled case. 55
3.22 Propellers' thrust for the circular setpoint simulation in the decoupled case. 56
3.23 Estimates $\hat{\Lambda}$ of the diagonal and off-diagonal terms of the effectivenss matrix for the circular setpoint simulation in the decoupled case. 57
3.24 Angular rates for the circular setpoint simulation in the coupled case. . . 58
3.25 Velocity for the circular setpoint simulation in the coupled case. 58
3.26 Position for the circular setpoint simulation in the coupled case. 59
3.27 State estimation error for the circular setpoint simulation in the coupled case. 60
3.28 Estimate of the effectiveness $\hat{\Lambda}$ for the circular setpoint simulation in the coupled case. 61

4.1 ANT-X drone. 63
4.2 North, East, Down position for the experiment with degradation of all rotors without external disturbance. 65
4.3 Velocity for the experiment with degradation of all rotors without external disturbance. 66
4.4 Adaptive inputs for the experiment with degradation of all rotors without external disturbance. 67
4.5 Estimated effectiveness $\hat{\Lambda}(t)$ for the experiment with degradation of all rotors without external disturbance. 68
4.6 North, East, Down position for the experiment with degradation of the third rotor without external disturbance. 70
4.7 North, East, Down velocity for the experiment with degradation of the third rotor without external disturbance. 71
4.8 Adaptive inputs for the experiment with degradation of the third rotor without external disturbance. 72
4.9 Estimated effectiveness $\hat{\Lambda}(t)$ for the experiment with degradation of the third rotor without external disturbance. 73
4.10 Roll, pitch and yaw angles for the experiment with external wind disturbance and degradation of the third rotor. 75
4.11 Roll, pitch and yaw rates for the experiment with external wind disturbance and degradation of the third rotor. 76

4.12 North, East, Down position for the experiment with external wind disturbance and degradation of the third rotor. 77
4.13 North, East, Down velocity for the experiment with external wind disturbance and degradation of the third rotor. 78
4.14 Estimated disturbances $\hat{\theta}_d(t)$ for the experiment with external wind disturbance and degradation of the third rotor. 79
4.15 Estimated effectiveness $\hat{\Lambda}(\mathrm{t})$ for the experiment with external wind disturbance and degradation of the third rotor. 80
4.16 North, East, Down Position for the experiment with external wind disturbance and degradation of all rotors. 82
4.17 North, East, Down Position for the experiment with external wind disturbance and degradation of all rotors. 83
4.18 Estimated disturbance $\hat{\theta}_d(t)$ for the experiment with external wind disturbance and degradation of all rotors. 84
4.19 Estimated effectiveness $\hat{\Lambda}(\mathrm{t})$ for the experiment with external wind disturbance and degradation of all rotors. 85

List of Tables

3.1 Plant Parameters. 35

List of Symbols

Variable	Description	SI unit
x_p	plant State	/
A_p	dynamics Matrix	/
B_p	Input Matrix	/
Λ	Control Effectiveness Matrix	/
λ	vector of diagonal elements of Λ	/
u	System Input	/
φ	Regressor Vector	/
θ_i	Uncertain Parameter	/
d	Disturbances	/
τ_u	Input dynamics time constant	/ s
B_ν	Rigid Body Input Matrix	/
ν	Virtual Controls	/
B_a or W_i	Actuator Mapping Maps	/
e_i	Generic Error	/
L	Luenberger Gain	/
U_i	Left Eigenvectors Matrix	/
Σ_i	Singular Values Matrix	/
V_i	Right Eigenvectors Matrix	/
D_i	Non-Null Submatrix of Σ_i	/
U_{ir}	Matrix of the directions in the state space that can be influenced by the control input	/
U_{in}	Matrix of the directions in the state space that cannot be influenced by the control input	/
V_{ir}	Matrix of the directions in the input space that have an effect on the state space	/

V_{in}	Matrix of the combinations that have no influence in the plant dynamics	/
Λ_{ar}	Λ single projection	/
Λ_{aa}	Λ double projection	/
I	Diagonal Unitary Matrix	/
$\tilde{\theta}$	Parameters Error	/
$\tilde{\Lambda}$	Control Effectiveness Matrix Error	/
V	Lyapunov Candidate Function	/
Γ_i	Gain Matrix	/
$f(\cdot)$	convex C^1 function	/
$\nabla f(\cdot)$	gradient of $f(\cdot)$	/
ϵ	scaling factor	/
θ_M	Proj. maximum value	/
F_I	NED Frame	/
F_B	Body Frame	m
ψ	Yaw angle	deg or rad
θ	Pitch Angle	deg or rad
ϕ	Roll angle	deg or rad
J	Inertia Matrx	$Kg \cdot m^2$
ω_b	Angular Velocity	rad/s
m	mass	kg
v_i	velocity	m/s
g	Gravity Acceleration	m/s^2
τ_c	Commanded Torque	Nm
T_c	Commanded Total Thrust	N
$D_{\tau\omega}$	Angular Velocity Damping Matrix	$N \cdot s/rad$
R	Rotational Matrix	/
e_3	Unit Vector	/
D_{fv}	Linear Velocity Damping Matrix	$N \cdot s/m$
$a^{\times}$	Cross Product $(a \times ...)$	/
T_i	Thrust Generated by i-th Propeller	N
p_i	Position Vector	m
l_c	Roll Moment	Nm
m_c	Pitch Moment	Nm

n_c	Yaw Moment	Nm
γ_i	Tilt Angle	deg or rad
ξ_i	Rotation Direction of the i-th propeller	/
σ	Torque Aerodynamics Coefficient	m
b	Arm Length	m
$\mathrm{s}(\cdot)$	Sine	/
$\mathrm{c}(\cdot)$	Cosine	/
f_c	Virtual Control Force	N
K_v	Velocity Proportional Gain Matrix	$N \cdot s/m$
K_{iv}	Velocity Integrative Gain Matrix	N/m
K_p	Position Proportional Gain Matrix	$1/s$
$k_{\phi\theta}$	Pitch,Roll Scalar Gain	rad/s
K_ψ	Yaw Scalar Gain	rad/s
K_ω	Angular Velocity Proportional Gain Matrix	$Nm \cdot s/rad$
$K_{i\omega}$	Angular Velocity Integrative Gain Matrix	Nm/rad
λ_τ	Torque Efficiency	/
λ_{Tc}	Total Thrust Efficiency	/
B_λ	Projections Transformation Matrix	/

Acknowledgements

Non sono una persona troppo emotiva, ma cercherò di dare il meglio di me per questi ringraziamenti.
Desidero, innanzitutto, ringraziare il Professor Davide Invernizzi, relatore di questa tesi, e Giovanni Gozzini, correlatore di questa tesi, per la disponibilità, la competenza e il costante supporto offerto durante tutto il percorso didattico, di ricerca e di stesura di questo elaborato.
Un sentito ringraziamento va anche a tutte le persone dell'ASCL per i preziosi suggerimenti, per l'attenzione dimostrata e per tutto l'aiuto dato.
Desidero, inoltre, ringraziare tutto il corpo docente del corso di Ingegneria Aerospaziale, per la professionalità, la disponibilità e la qualità della formazione ricevuta in questi anni, che hanno contribuito in modo determinante alla mia crescita accademica e personale.
Ringrazio tutta la mia famiglia, i miei genitori Cristina e Luciano, mia nonna Claudia, mia zia Michela, mio zio Massimo e le mie cugine Martina e Giulia, per il supporto incondizionato, la pazienza (soprattutto la pazienza) e l'incoraggiamento che non sono mai mancati durante tutti questi anni di studio.
Un grazie speciale va ai miei amici:

- Jaco, Sisso, Fede, Chendi, Gp e Marco: i miei amici storici, che conosco quasi tutti dalle medie, con cui ho passato tanti, tantissimi momenti indimenticabili e con cui ho un rapporto molto, molto profondo.
- Muro, Grazza, Lenzo, Rogo, Acca, Teo Guidi, Jhonny e Camilla: i miei ex compagni delle superiori (e fidanzata) a cui voglio un mondo di bene e su cui posso sempre contare.
- Fabi, Fra, Emma, Barbara, Aurora, Simo, Jacopo, Mattia e tutto il gruppo degli SQUATtrinati: per tutta la gentilezza, l'amicizia e l'affetto che hanno riposto nei miei confronti (ovviamente tutto ricambiato).
- Stefano, Silvia, Adriana e Roberto: le persone che conosco da più tempo nella mia vita e che considero come una seconda famiglia.

Infine, ringrazio tutte le persone che, anche con un solo sorriso, hanno contribuito a rendere questo percorso indimenticabile.